The Thesis Committee for Jennifer Leigh Kurkowski certifies that this is the approved version of the following thesis:

Seismic Vulnerability of Masonry Facades in Texas and Oklahoma Regions

APPROVED BY
SUPERVISING COMMITTEE:

Patricia M. Clayton, Supervisor

Juan Murcia-Delso

Seismic Vulnerability of Masonry Facades in Texas and Oklahoma Regions

by

Jennifer Leigh Kurkowski

Thesis

Presented to the Faculty of the Graduate School of

The University of Texas at Austin

in Partial Fulfillment of the

Requirements for the Degree of

Master of Science in Engineering

The University of Texas at Austin

August 2018

Acknowledgements

I would like to thank my advisor, Dr. Patricia Clayton, for all of her support, enthusiasm, and guidance over the course of this research project. Her willingness to help and make sure not only I, but all of her students, learn and succeed helped to make the master's degree program, and research, rewarding and provide invaluable insight. I could not have made it through without her help and support.

I would also like to thank the TexNet Seismic Monitoring Project, as well as the Industrial Associated of the Center for Integrated Seismic Research (CISR), at the Bureau of Economic Geology of the University of Texas, for providing the necessary funding that allowed me to conduct this research, as well as receive my master's degree.

My ability to succeed throughout the degree program and this research study was also only possible through the support I received outside of the university. I would like to especially thank my family, who never failed to provide encouragement and moral support. I would most especially give thanks to God for not only guiding me into a field I'm passionate about, but also constantly reminding me of who I am, what is possible, and what is actually important when I get distracted and forget.

Abstract

Seismic Vulnerability of Masonry Facades in Texas and Oklahoma

Jennifer Leigh Kurkowski, MSE
The University of Texas at Austin, 2018

Supervisor: Patricia Clayton

In the Oklahoma and Texas area, an increase in human-induced seismic activity has resulted in millions of dollars of damage in the region, primarily to residential homes. The most common damage is to chimneys and masonry veneers. This study focuses on better understanding and evaluating the fragility of brick veneers to the human-induced earthquakes that have been experienced in this region. A computational wall model was developed based on previous experimental and computational research on non-seismically detailed brick veneers from the literature. A suite of ground motion recorded in Texas, Oklahoma, and Kansas since 2010 was provided by geotechnical engineering researchers at the University of Texas at Austin and was used in this study to represent the seismic hazards expected in the region. Fragility curves were developed using the experimentally validated computational models, in which ground motion uncertainty was accounted for in the suite of ground motions used in the fragility analysis. To evaluate the effects of different seismic hazards on brick veneer fragility, ground motion ensembles representing both the New Madrid and the Texas-region seismic events were considered. Fragility curves were also generated using brick veneer models with variations in brick tie types and configurations to evaluate the effects of veneer anchorage detailing and retrofit strategies on seismic performance.

The study has shown that when trying to predict the fragility of masonry façade, it's important to utilize ground motions from the region and seismic hazard of interest, as it has an impact on the relative fragility of the wall model because of varying characteristics. Although

using a code compliant gauge for veneer ties is ideal, it was shown that the most critical part of installation is including ties in the upper portion of a wall panel. If it is desired to strengthen an existing brick veneer wall, without having to reinstall the wall, adding additional anchorage at the top of the wall will still provide increased seismic resistance, which may be a good course of action if it is suspected that there are ties that are missing, have corroded, or were not installed properly.

TABLE OF CONTENTS

LIST OF TABLES ix

LIST OF FIGURES x

CHAPTER 1: INTRODUCTION AND RESEARCH MOTIVATION…….....1

1.1 PROBLEM BACKGROUND 1

1.2 REGIONAL BUILDING INFORMATION 4

1.2.1 BRICK VENEER CONSTRUCTION 9

1.2.2 COMMON BRICK VENEER CONSTRUCTION METHODOLOGY AND ISSUES 12

1.3 PREVIOUS RESEARCH ON SEISMIC PERFORMANCE OF MASONRY VENEER……14

1.4 PURPOSE OF CURRENT RESEARCH STUDY 17

CHAPTER 2: COMPUTATIONAL MODEL CREATION AND VALIDATION……...19

2.1 ORIGINAL RENECKIS EXPERIMENTAL TESTS AND MODEL 19

2.2 OPENSEES TIE MODEL DEVELOPMENT AND VALIDATION 24

2.3 OPENSEES STRIP MODEL DEVELOPMENT AND VALIDATION 30

2.3.1 ELEMENTS IN OPENSEES MODEL 31

2.3.1.1 SHELL ELEMENTS 31

2.3.1.2 BEAM-COLUMN ELEMENTS 33

2.3.1.3 LATERAL SPRING ELEMENTS 34

2.3.1.4 ROTATIONAL SPRING ELEMENTS 35

2.3.2 SEISMIC MASS 36

2.3.3 OPENSEES STRIP MODEL VALIDATION 38

2.4 DAMAGE STATES 40

2.5 CALCULATION OF FUNDAMENTAL PERIODS 42

2.6 CONCLUSION 43

CHAPTER 3: DEVELOPMENT AND ANALYSIS OF FRAGILITY CURVES…….44

3.1 DEFINITION OF FRAGILITY CURVES 44

3.2 WALL PARAMETERS EVALUATED WITH FRAGILITY CURVES 46

3.3 GROUND MOTION SUITES USED IN FRAGILITY ANALYSIS 49

3.3.1 GROUND MOTION CHARACTERISTICS 53

3.3.2 GROUND MOTION SPECTRAL RESPONSES 56

3.3.2.1 TEXAS SUITE SPECTRAL RESPONSE 56

3.3.2.2 NEW MADRID SPECTRAL RESPONSE 61

3.4 FRAGILITY CURVE COMPARISONS 62

3.4.1 Effects of Ground Motion Characteristics and Tie Types 62
3.4.1.1 Texas Suite Fragility Curves 64
3.4.2 Effects of Tie Spacing on Fragility Curves 73
3.4.3 Effects of Retrofits on Fragility Curves 77
3.5 CONCLUSION 81
CHAPTER 4: CONCLUSION, RECOMMENDATIONS, AND FUTURE RESEARCH...82
4.1 SUMMARY OF RESEARCH PROJECT 82
4.2 CONCLUSIONS 83
4.3 RECOMMENDATIONS AND FUTURE RESEARCH 84
APPENDIX A…..... I
APPENDIX B…..... VIII
REFERENCES…..... IX

List of Tables

Table 1.1. Percentage of regional buildings with designated exterior material.
(U.S. Census Bureau, 2016)……....4

Table 2.1. Tie displacement limit values……...28

Table 2.2: Shell element material properties…….....32

Table 2.3: Wood stud material properties……..33

Table 2.4: Experimental and model wall initial natural periods…….....42

Table 2.5: Natural period of original models and models after first tie failure…….43

Table 3.1: Wall models used to create fragility curves and evaluate impact
of wall parameters……....49

Table 3.2: Ground motion characteristics for comparative sampling……....53

Table 3.3: Median PGA and lognormal standard deviation parameters
for fragility curves of models subjected to New Madrid suite.
(Wen and Wu, 2001)…….64

Table 3.4: Median PGA and lognormal standard deviations of fragility curves
from Texas random samplings…….66

Table 3.5: Median PGA and lognormal standard deviations of characteristic
Texas samples……...71

Table 3.6: Vertical locations of veneer ties in modified non-code compliant walls……..74

Table 3.7: Median PGAs of modified non-code compliant spacing wall models…….76

Table 3.8: Tie locations for retrofitted non-code compliant wall models……..78

Table 3.9: Median PGAs of retrofitted larger than code-compliant tie spacing
wall models…….....79

List of Figures

Figure 1.1. Damage to masonry buildings due to Oklahoma earthquakes:
(a) M5.0 Cushing, (b) M5.8 Pawnee, and (c) M5.7 Prague. (EERI, 2016)……..…1

Figure 1.2: USGS Potential for Damage National Map (USGS, 2018)……..…3

Figure 1.3. U.S. Census Bureau map of states by census region. (U.S. Census
Bureau, 2016)……....5

Figure 1.4. Trends of residential exterior material from 1973 to 2016 for
U.S. Census Bureau regions: (a) West, (b) South, and (c) Total U.S.
(U.S. Census Bureau, 2016)…….....……..6-7

Figure 1.5 Southern U.S. trends of residential exterior material including
specific sub region (TX & OK) data from 1999 to 2016. (Bradtmueller
et al., 2014), (U.S. Census Bureau, 2013)……..….7

Figure 1.6. Percentage distribution of building stock by age of construction
for sub regions: (a) Western Pacific and (b) West South Central
(USGS, 2013)……..……...8

Figure 1.7. Examples of Heckmann Building Products, Inc. possible veneer tie options.
(Heckmann Building Products, Inc., 2018)……...…9

Figure 1.8. Commonly used corrugated brick veneer tie in installed position.
(Heckmann Building Products, 2018)……..…..….10

Figure 1.9. Basic steps in corrugated tie installation (Masonry Magazine, 2015)…….10

Figure 1.10. Setup of shake table wood-framed specimen from previous
Klingner et al. study at UCSD. (Klingner et al., 2013)……..13

Figure 2.1. Experimental wall specimen setup (schematic from Reneckis and LaFave, 2009)……..21

Figure 2.2 Renderings of brick veneer wall: (a) Actual wall as constructed, (b) Actual wall with individual elements labeled, (c) FE veneer full wall model, and (d) FE strip wall model.....23

Figure 2.3. Tie subassembly test setup. (Reneckis, 2009)…….24

Figure 2.4. Veneer Tie Hysteretic Backbones in OpenSEES for different tie types: (a) 28ga(min), (b) 28ga(ecc), (c) 22ga(min), and (d) 22ga(ecc)……..26

Figure 2.5. Cyclic behavior of tie subassemblies and OpenSEES hysteretic material for veneer ties: (a) experimental 28ga(ecc) subassembly, (b) 28ga(ecc), (c) experimental 22ga(ecc) subassembly, and (d) 22ga(ecc)……...27

Figure 2.6. Validation of use of displacement limits for tie backbones based on comparing OpenSEES and experimental peak displacement data for specimens: (a) Wall-1 and (b) Wall-2……..30

Figure 2.7. Exploded view of strip model with individual OpenSEES elements labeled……..…31

Figure 2.8. Bilinear rotational spring behavior model. (Reneckis, 2009)……..36

Figure 2.9. Dimensions of OpenSEES Model as Loaded for Analysis: (a) side, (b) front, and (c) top……...37

Figure 2.10. Veneer and wood backup peak displacements along length of wall for experimental walls and OpenSEES model subjected to 10% in 50yr motion with PGA=0.059g scaled to corresponding experimental values: (a) Wall-1 scaled to a PGA of 0.38g and (b) Wall-2 scaled to a PGA of 0.18g……..…39

Figure 2.11. Comparison of OpenSEES model peak displacements to experimental and previous FE model results for both solid panel walls from previous experimental tests: (a) Wall-1 and (b) Wall-2……..40

Figure 2.12. Points where Damage State 1 and 2 were reached for OpenSEES and experimental results for (a) Wall-1 and (b) Wall-2……...….41

Figure 3.1. Example probability of reaching a given damage state, for discrete 0.1g increments and full curve fit……...45

Figure 3.2 Representative elevations of model prototype houses for: (a) one story and (b) two stories. (Isoda et al. 2001) (Schematic from Reneckis and LaFave, 2009)……...49

Figure 3.3: (a) Locations and Magnitudes of selected earthquake events, (b) Locations of seismic recording stations in Texas, Oklahoma, and Kansas; distinction of stations with V_{S30} estimates based on Zalachoris et al. (2017) and Parker et al. (2017) (Khosravikia et al., 2018)…….50

Figure 3.4: (a) Locations and Magnitudes of earthquake events selected for previous study, (b) Locations of seismic recording selected for previous study. (Khosravikia et al., 2018)……..51

Figure 3.5: Ground motion database utilized in this study: a) Moment Magnitude (M_W) – Hypocentral Distance (R_{hyp}) distribution, and b) number of stations per NEHRP site classification; The selected ground motions for use in this project are shown in red. (Khosravikia et al., 2018)…….52

Figure 3.6. Box and Whisker plots displaying distribution within each sample of particular ground motion characteristics: (a) Magnitude of Event,

(b) Hypocentral Depth, (c) Recorded PGA, (d) Vs_{30}[29], and
(e) Hypocentral Distance to Station……...55
Figure 3.7: Spectral Acceleration plots for ground motion sample groups:
(a) Random 1, (b) Random 2, (c) Random 3, (d) Random 4,
(e) Maximum Magnitude, (f) Maximum PGA, and (g) Minimum
Hypocentral Distance……57-58
Figure 3.8. Average Spectral Acceleration for each sample set of ground motion files……...59
Figure 3.9. Spectral Acceleration plot of New Madrid ground motion suite,
including average spectrum……61
Figure 3.10. Average Spectral Acceleration plots for Texas and New Madrid sample sets……..62
Figure 3.11. Comparison of OpenSEES model and previous study fragility curves
subjected to New Madrid suite ground motions, for both tie types
and damage states: (a) 28ga(min) (Wall #1) and (b) 22ga(ecc) (Wall #2)……...63
Figure 3.12. Fragility curves from models subjected to four random sets of
Texas ground motion files: (a) 28ga(min) Ties (Wall #1) Damage
State 1, (b) 28ga(min) Ties (Wall #1) DS 2, (c) 22ga(ecc) (Wall #2)
Damage State 1, and (d) 22ga(ecc) (Wall #2) Damage State 2……....65
Figure 3.13. Fragility curves from selection of Texas ground motion files with
largest magnitude events: (a) Damage State 1 and (b) Damage State 2……...67
Figure 3.14. Fragility curves from selection of Texas ground motion files with
largest maximum PGA recordings: (a) Damage State 1 and
(b) Damage State 2……67

Figure 3.15. Fragility curves from selection of Texas ground motion files with smallest hypocentral distance recordings: (a) Damage State 1 and (b) Damage State 2……....68

Figure 3.16. Comparison of fragility curves based on selected sample characteristics: (a) 28ga(min) Damage State 1 (Wall 1), (b) 28ga(min) Damage State 2 (Wall 1), (c) 22ga(ecc) Damage State 1 (Wall 2), and (d) 22ga(ecc) Damage State 2 (Wall 2)……....69

Figure 3.17. Comparison of Texas sample groups with corresponding New Madrid fragility curve for: (a) 28ga(min) Damage State 1 (Wall 1), (b) 28ga(min) Damage State 2 (Wall 1), (c) 22ga(ecc) Damage State 1 (Wall 2), and (d) 22ga(ecc) Damage State 2 (Wall 2)……...73

Figure 3.18. Schematics tie layout for larger than code compliant spacing: (a) Wall #3, and (b) Wall #4…….74

Figure 3.19. Comparison of original 28ga(min) wall model (Wall #1) to two models with larger than code-compliant tie layout wall models: (a) DS 1 for Wall #3 & #4, and (b) DS 2 for Wall #3 & #4……..77

Figure 3.20. Schematic of retrofits of larger than code-compliant wall models: (a) Wall #5, and (b) Wall #6…….78

Figure 3.21. Fragility curves for both larger than code compliant walls (#3 and #4) and retrofitted walls (#5 and #6) under Random Set 2:(a) Damage State 1, (b) Damage State 2……80

Chapter 1: Introduction and Motivation

1.1 Problem Background

In 2016 alone, over 500 M3+ earthquakes occurred in the Central and Eastern parts of the United States, while in 1973-2008 there were only an average of 21 earthquakes per year within the same region (USGS, 2016a). Most of these recent events are not naturally occurring, but rather, are believed to be human-induced, related to oil and gas industry activities, based on studies, such as Ellsworth et al. (2012), demonstrating that the increase in seismicity is inconsistent with natural processes in such a geologically stable region. Therefore, few of the 7 million people impacted have ever dealt with the threat of earthquakes previously. Infrastructure in these areas, typically designed without seismic consideration, are vulnerable to damage, especially façade damage, which can occur even under small ground accelerations. Examples of the type of damage observed after seismic events in Oklahoma are shown in Figure 1.1.

(a)

(b)

(c)

Figure 1.1. Damage to masonry buildings due to Oklahoma earthquakes: (a) M5.0 Cushing, (b) M5.8 Pawnee, and (c) M5.7 Prague. (EERI, 2016)

Much of the observed damage following the 2011 M5.7 Prague, OK, the 2016 M5.8 Pawnee, OK, and the 2016 M5.0 Cushing, OK earthquakes includes masonry veneer and chimney failures in residential homes, which has generated millions of dollars of insurance claims. Insurance companies paid $5.1 million on earthquake claims in Oklahoma from 2010 through 2016, but that was only with an approval rating of approximately 3 in 20 claims, according to Tulsa World News. Following the M5.8 Pawnee event, 423 insurance claims were filed for just that particular earthquake. (Jones, 2017)

While the typical damage is nonstructural, such as in Figure 1.1, having widespread occurrences significantly impact those residing in the region experiencing the increase in seismic activity. Failing brick facades causes not only a physical hazard to residents, but the need for repairs becomes costly for both individuals and governmental infrastructure organizations. According to the one-year USGS (2016a) earthquake hazard predictions accounting for induced seismic activity, the likelihood of experiencing minor damage from an earthquake in parts of the Central U.S., such as Oklahoma, is now comparable with that in California, as shown in Figure 1.2.

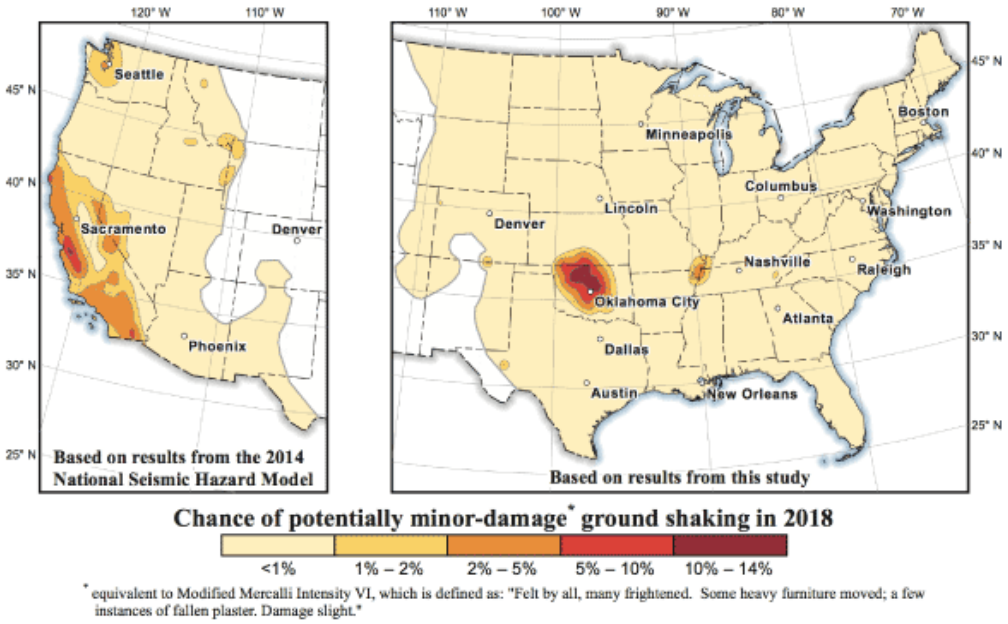

Figure 1.2. USGS potential for damage national map. (USGS, 2018)

Oklahoma experienced three of its strongest ever earthquake just in 2016, all of which were M5.0 or greater. According to available USGS Shake Map Metadata, the 2016 M5.1 Fairview event had a maximum PGA value of 0.264g (USGS, 2016c), the 2016 M5.0 Cushing, OK event had a maximum PGA of 0.593g (USGS, 2016b), and the 2016 M5.8 Pawnee, OK event had a maximum PGA of 0.463g (USGS, 2016d). The magnitude of these recent earthquakes indicates that the seismic events in the region have a potential for increased intensity, along with the increase in overall frequency of events. A study conducted by McGarr (2014) demonstrated that the magnitudes of earthquakes influenced by wastewater fluid injection appear to be limited by the total volume of fluid injected in that specific area. However, the correlation between magnitude and volume of fluid injected needs continued development, and the possibility of larger magnitudes compared to fluid injection cannot be fully discounted.

These areas are most at risk to experience damage, particularly nonstructural damage, in existing buildings as seismic activity has not been a factor in typical regional construction. In

addition, national building code committees are unsure of how to treat this new form of hazard in design of new construction, largely due to lack of information and uncertainty associated with predicting hazards tied to future human activity. Therefore, new construction may also be similarly vulnerable to seismic damage if these induced seismic hazards are not specifically accounted for in design.

1.2 Regional Building Information

Typical construction of buildings, including residential, varies across regions of the United States. In order to determine the dominant methods used in the states of interest, particularly Texas and Oklahoma, United States Census Bureau data was compiled on the characteristics of homes by region in which they were built. Of specific interest in this story, is the material used for the exterior cladding of the home. The percent of buildings constructed within a region of each exterior material type is shown in Table 1.1. The data in Table 1.1 is for both 1973 and 2016 to show the change in percentage in a region over time. Figure 1.3 is included that shows how the states are divided into the regional categories by the U.S. Census Bureau.

Table 1.1: Percentage of regional buildings with designated exterior material. (U.S. Census Bureau, 2016)

Census	Brick		Wood		Stucco		Other	
Region	1973	2016	1973	2016	1973	2016	1973	2016
South	64	35[(a)]	16	2	5	22	16	41
West	6	1	34	5	45	52	15	42
Total U.S.	35	22	30	5	12	24	22	49

[(a)]Percentage of brick in sub region of Oklahoma and Texas is higher than the rest of the South region, see Figure 1.5.

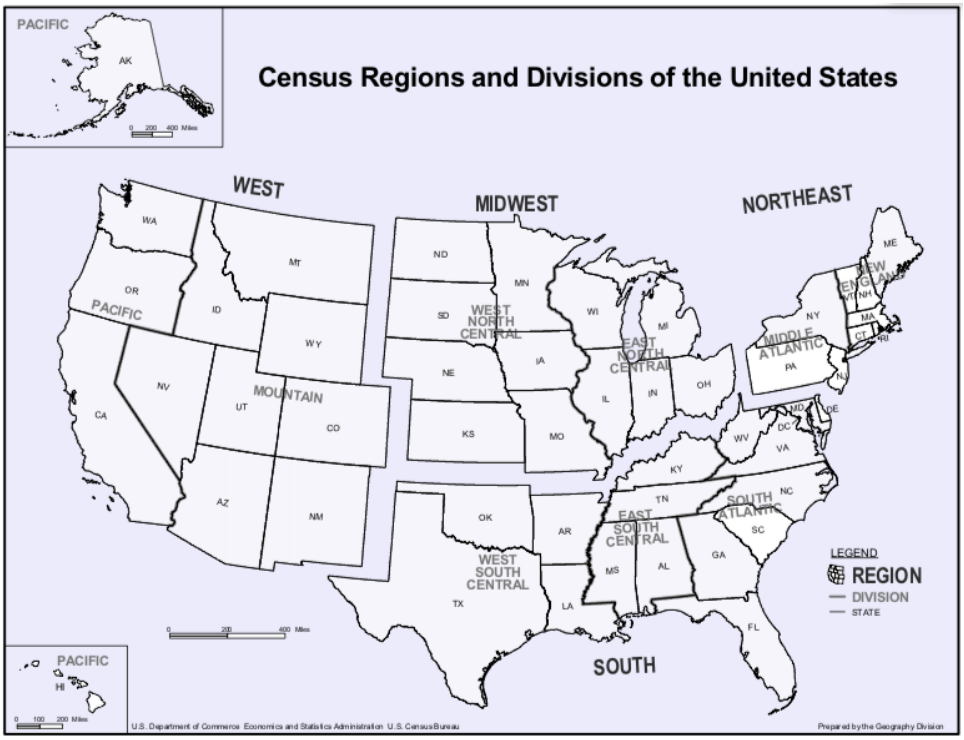

Figure 1.3. U.S. Census Bureau map of states by census region. (U.S. Census Bureau, 2016)

As displayed in Table 1.1, the most common exterior cladding for residential homes in the Western U.S. in the 1970s were wood and stucco, but more current buildings are either stucco or in the other category, which includes a variety of vinyl and fiber based materials. In contrast, homes in the Southern U.S. had a majority of brick cladding in the 1970s, and current homes are shown to mostly still clad in brick or other materials. The difference in residential building construction practices between the West and South is part of the motivation for the current study. While historically seismically active regions such as the West Coast typically avoid brick cladding, as it is known to perform poorly during earthquakes, areas with more recent increases in seismicity, such as Texas and Oklahoma, have a large population of brick clad homes that may be susceptible to seismic damage.

The trend in exterior housing material for the U.S. as a whole, as well as the South and West, is displayed in the plots in Figure 1.4. Figure 1.4(a) shows that in Western states, such as

California, there has consistently been minimal use of brick on exterior construction, less than 10%, over the 43-year time period provided. In contrast, Figure 1.4(b) demonstrates that since the early 1970s, states in the Southern census region have a consistently higher than national average percentage of brick utilized, compared to the total U.S. plot in Figure 1.4(c).

In addition, Figure 1.5 shows that specifically within the West South Central sub region, which includes Oklahoma and Texas, over 60% of buildings had brick as the exterior material in the years 1999-2012. (Bradtmueller et al., 2014) The average percentage in the larger Southern region was only around 40%, as visible in Figure 1.5. Therefore, even though the South already had larger than national average percentages of brick, within the smaller sub region, including Texas and Oklahoma, it was even higher.

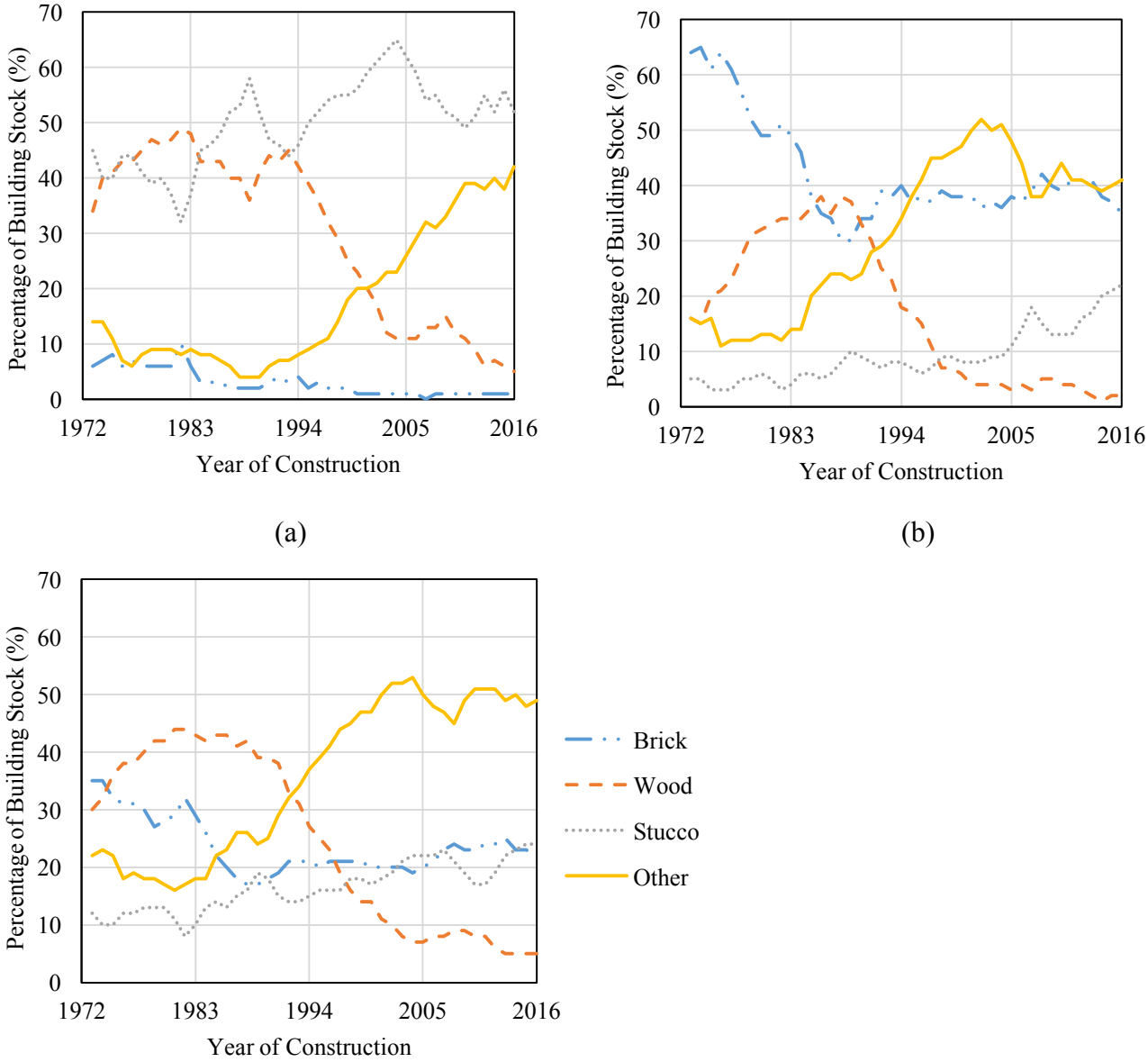

Figure 1.4. Trends of residential exterior material from 1973 to 2016 for U.S. Census Bureau regions: (a) West, (b) South, and (c) Total U.S. (U.S. Census Bureau, 2016)

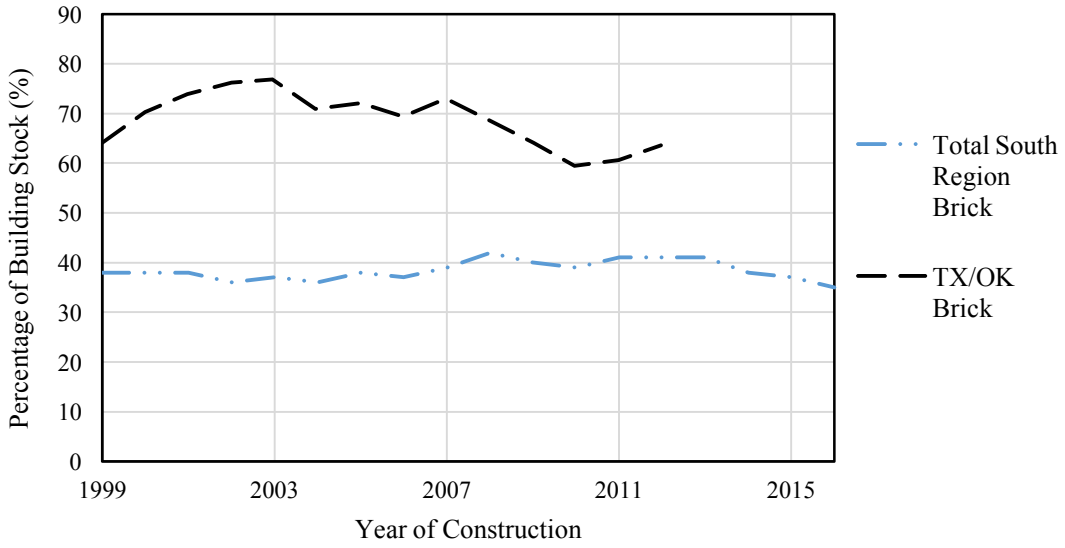

Figure 1.5 Southern U.S. trends of residential exterior material including specific sub region (TX & OK) data from 1999 to 2016. (Bradtmueller et al., 2014), (U.S. Census Bureau, 2013)

The U.S. Census Bureau in 2013 provided data on the age of building stock by region. The percentage distribution by decade is shown in Figure 1.6 for the two areas of interest, West South Central (i.e. TX, OK, AR, LA) and Western Pacific states (i.e. CA, OR, WA). The charts in both Figure 1.6(a) and (b) show that the majority of buildings in both regions were constructed in the year range of 1960-1999. Comparing the age of construction back to the plots in Figure 1.4 shows that within the timeframe the majority of homes were built, brick was the dominant material in the South, while stucco or wood were most prevalent in the West. The median age of the building stock is 1979, 1975, and 1975, for the West South Central and Western Pacific regions, and Total U.S., respectively.

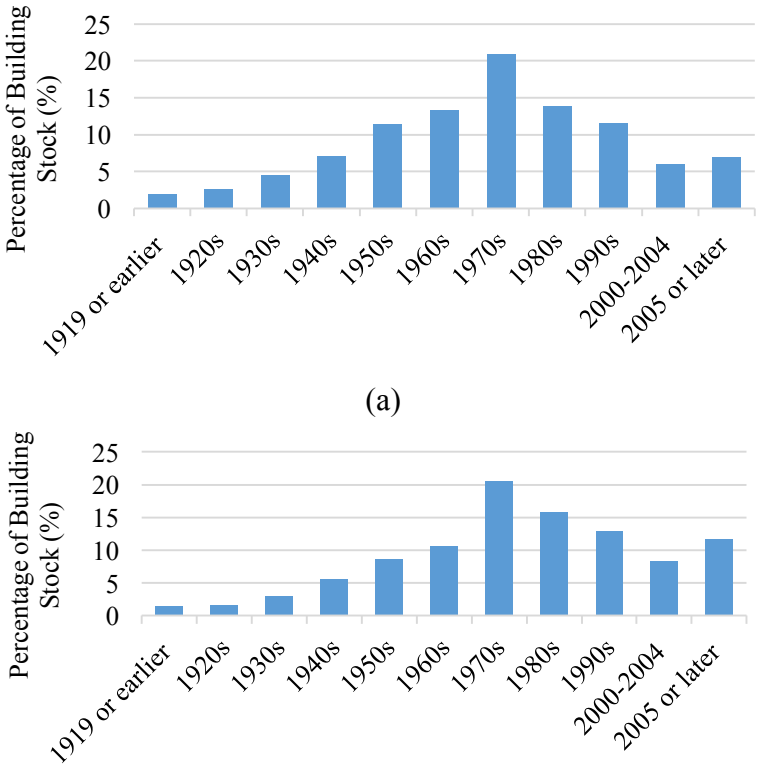

Figure 1.6. Percentage distribution of building stock by age of construction for sub regions: (a) Western Pacific and (b) West South Central (USGS, 2013)

In areas with historic seismic activity, such as the West Coast of the U.S., brick veneers, which are known to have poor seismic performance, are uncommon; whereas brick veneers are commonly employed in areas of the Central and Eastern U.S. The historical prevalence of buildings with brick masonry exteriors in areas of Texas and Oklahoma, where the increase in seismic activity has also been experienced, motivates the need to investigate the potential for seismic damage to wood-framed structures with brick veneer facades.

1.2.1 Brick Veneer Construction

In typical brick veneer construction, the brick façade is not load bearing, but rather is connected back to the load bearing wall with veneer ties. The actual load bearing wall is often constructed of wood studs and oriented strand board (OSB), or concrete masonry unit (CMU) blocks. There is a variety of available veneer tie products that can be installed to attach the brick

veneer to the backing, some of which are shown in Figure 1.7. However, one of the most common ties used in residential construction is the corrugated tie, due to it being inexpensive and easy to install. Figure 1.8 displays the corrugated metal tie as installed, while Figure 1.9 demonstrates the basic steps in the construction of the ties. It should be noted that the construction of the brick veneer wall requires a 1 inch gap between the back face of the brick and the front face of the wood sheathing. The required gap, which can be seen in all of the tie examples from Figures 1.7 through 1.9, allows for moisture to escape from behind the veneer wall and prevent a build up of water.

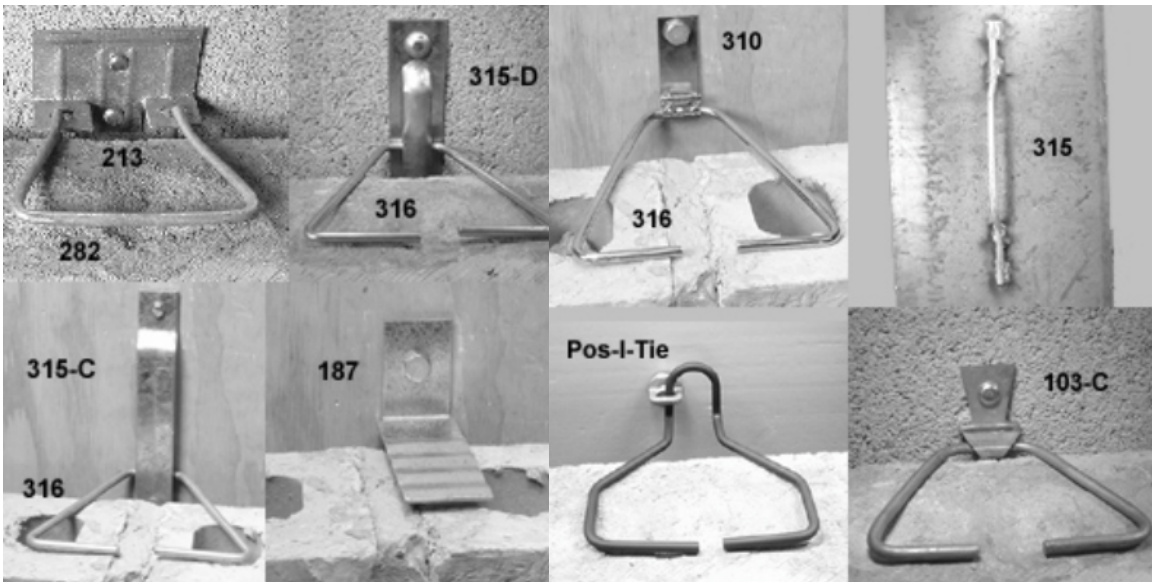

Figure 1.7. Examples of Heckmann Building Products, Inc. possible veneer tie options. (Heckmann Building Products, Inc., 2018)

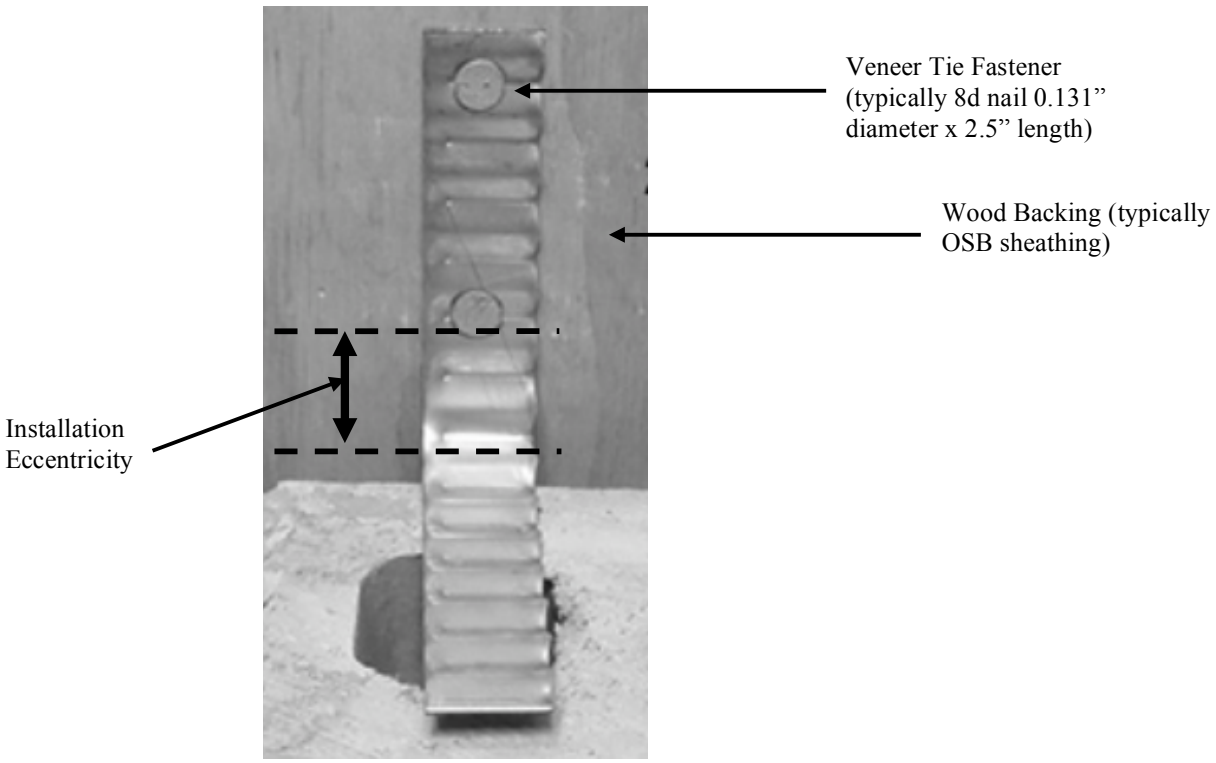

Figure 1.8. Commonly used corrugated brick veneer tie in installed position. (Heckmann Building Products, 2018)

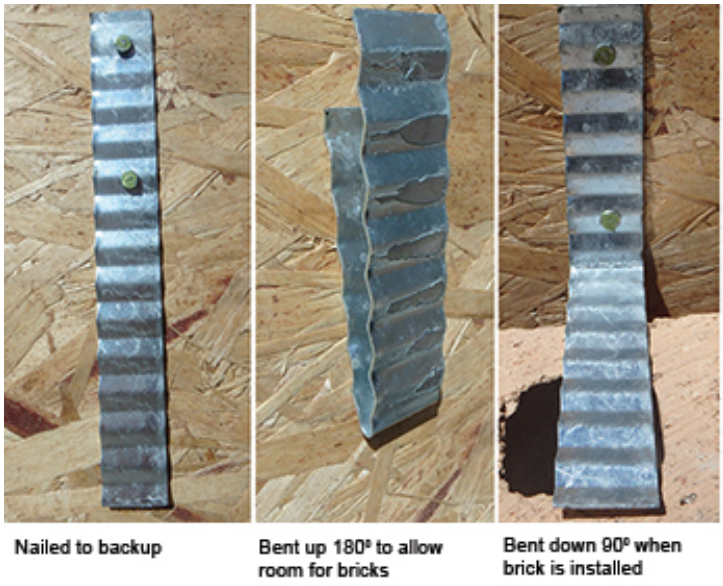

Figure 1.9. Basic steps in corrugated tie installation (Masonry Magazine, 2015).

Brick veneer construction follows the International Building Code (IBC) with provisions from the Building Code Requirements for Masonry Structures (TMS 402/ACI 530/ASCE 5). The

IBC mandates that for veneer anchors in areas of low seismicity (i.e. Seismic Design Category C or below), the maximum spacing is 32 in. horizontally and 24 in. vertically, with one anchor required per 2.67 square feet of wall area. In addition, anchors are to be fastened with a common 8d nail or equivalent, with an eccentricity of less than ½ in., but at least 5/32 in. A visual of the eccentricity of installation, which is the distance between the fastener and the 90-degree bend in the corrugated tie, is found in Figure 1.8. If corrugated anchors are installed, IBC requires a minimum thickness of 0.03 in., which is equivalent to a 22-gauge anchor.

1.2.2 Common Brick Veneer Construction Methodology And Issues

For the collection of data on common methodology and issues, the research was in the form of personal conversations with tie suppliers and forensic engineering firms. Two veneer anchorage suppliers, Hohmann & Barnard, Inc. (H&B) (C. Bupp, personal communication, July, 2017) and Heckmann Building Products (P. Curtis, personal communication, July, 2017), were interviewed on what contractors might typically do that cause ties to not perform to their specified capacity. In addition, the forensic engineering firm Building Diagnostics, Inc. (BDI) (R. Chamra, personal communication, March, 2017) gave information on what problems they saw the most when observing brick veneer after failure had occurred. BDI (2017) also discussed simple retrofit options, for example the addition of helical anchors into a preexisting brick veneer wall, which provided information on what realistic options are available in the industry and how it could be applied to this study.

In order to properly use corrugated ties, brick anchor suppliers, such as H&B (2018), expressed that a wooden backup is required, such as the OSB shown in Figures 1.8 and 1.9. Even though this is the industry and code recommendation, a common construction error is to use these particular ties with CMU block walls as the back up structure. According to the technical

sales representative at H&B (2018), most residential or older buildings, which is the majority of building stock for the regions of interest (Figure 1.6), likely were built using thinner 28-gauge due to a lack of stringent code development and enforcement in the residential building sector. In addition, one of the common problems with corrugated metal tie installation is the compromising of the cross section that occurs when it must be bent up and down to allow for brick installation, such as in Figure 1.9.

Suppliers at H&B also expressed that oftentimes in anchor installation, the tie is not sufficiently embedded into the mortar as necessary to provide the best possible tie performance (C. Bupp, 2018). When attaching the anchors to the wood backup, one common error is the use of fasteners other than those specified that provide reduced pull-out strength for the tie, such as shorter 6d or roofing nails. Both of these errors will cause premature failure of the brick veneer anchorage as the veneer tries to separate from the backup structure.

In regions with more moisture exposure, such as snowfall, it has been common to find a large percentage of the ties installed in a wall to be rusted beyond the point of usefulness, according to contacts at Heckmann Anchors (P. Curtis, 2018). Veneer tie corrosion can also occur from excess mortar that drops into the cavity and onto a tie, leading the moisture in the mortar to cause corrosion in that tie. Moisture exposure to the ties can also be attributed to a lack of air space that should be present between the veneer and wood to prevent water build up by allowing it to flow outwards towards the ground. In addition, Heckmann (2018) suppliers pointed out that even with a lack of anchors behind a brick veneer wall, it can oftentimes remain standing many years, but will quickly fail when subjected to lateral forces, such as those experienced in an earthquake. Overall, industry contacts felt that most often, unexpected tie failures were due to incorrect usage

(e.g., using 28-gauge ties instead of code compliant 22-gauge) and errors in installation, such as too large of tie spacing or not enough engaged in the mortar beds.

1.3 Previous Research On Seismic Performance Of Masonry Veneer

Previous studies have been conducted to investigate the behavior of brick veneer walls under seismic activity. Klingner et al. (2013) specifically studied the performance of low-rise wood-framed structures in high-seismic regions with clay masonry veneer. The full-scale building specimens were evaluated using the shake table present at the University of California San Diego, shown in Figure 1.10. The specimens tested were constructed according to the seismic requirements of ASCE 7-05[2], for seismic design category (SDC) D and E, which includes provisions from the Masonry Standards Joint Committee (MSJC)[5]. In order to meet 2008 MSJC SDC D requirements, anchors were place at 16 in. each way, and for SDC E the anchors were accompanied by joint reinforcement. Another SDC E alternative that was tested was to place rigid, non-corrugated anchors at 16 in. horizontally and 24 in. vertically.

Figure 1.10. Setup of shake table wood-framed specimen from previous Klingner et al. study at UCSD. (Klingner et al., 2013)

The specimens were subjected to ground motion histories from the 1994 Northridge Earthquake. The two time histories were scaled to different levels based on a design response

spectrum that correlated with SDC D and E, for both a MCE and DBE event. Results from the testing indicated that the wood-framed specimen did not collapse under the maximum considered earthquake shaking level, and the veneer was not impacted by the additional bed-joint reinforcement, required for SDC E. In addition, the study led to MSJC code changes for SDC D or above that required anchor fasteners with higher capacities and more resistance to wood moisture content variations (MSJC, 2008). Klingner et al. (2013) studied behavior of seismically-detailed brick veneers for both in-plane and out-of-plane shaking via experimental and analytical studies, including development of computational models in OpenSEES. However, the current study focused solely on out-of-plane motion partially because out-of-plane damage and failure were most common for wood-backed Klingner et al. (2013) specimens, and was typically the first damage to be observed with increasing shaking intensity.

Historically, however, Texas, Oklahoma, and other central U.S. states, experienced significantly less seismic activity than the California region for which the Klingner et al. (2013) specimens were designed, which impacts the design and detailing requirements per ASCE 7-05 and 2008 MSJC. Thus, it is highly unlikely that existing wood-framed, brick veneer buildings in the Texas and Oklahoma region were built with the level of seismic detailing included in the Klingner et al. (2013) specimens.

An additional study conducted by Reneckis and LaFave (2009) specifically investigated the seismic performance of wood-backed walls with brick veneer designed and constructed in regions of low- to moderate-seismic activity, like the Central and Eastern U.S. In this study, the brick, stud, and tie materials and construction were based on 2008 MSJC requirements for brick veneer construction in SDC C or lower, which is applicable for the region of focus in this study. This study included quasi-static cyclic tests of subassemblies of wood backing, fastener, tie,

mortar, and bricks to characterize the cyclic behavior and failure modes of the anchorage, as well as out-of-plane shake table testing of planar walls to characterize brick veneer damage states experience during seismic shaking. Reneckis and LaFave (2009) also constructed full size specimens using 28-gauge corrugated ties, because it better represented actual typical construction practices, rather than code complaint 22-gauge. However, subassembly tests of the individual veneer anchors were conducted for both 22ga and 28ga. Further details of the Reneckis and LaFave (2009) experimental testing will be discussed in Section 2.1.

Nonlinear cyclic models were created based on the tie subassembly behavior and were then utilized in the full wall panel models created in ABAQUS (Abaqus Inc., 2006), which were then validated by the shake table results. The computational models were used to develop fragility curves based on damage states for repairable damage and wall instability, based on tie deformation limits from subassembly tests. More details of the models developed by Reneckis and LaFave (2009) will be provided in Chapter 2, as they were the basis for the OpenSEES (McKenna, 2004) models created for the current study.

Reneckis and LaFave found that the overall veneer wall performance directly correlated to the anchor tensile properties, indicating the importance of focusing on the installation and characteristics of the ties when trying to ensure the overall performance of the veneer wall. It was also found that models with the worst case layout of code compliant 22ga ties with ½ in. eccentricity spaced at 24 in. vertically, performed acceptably for walls in the New Madrid region with 2% in 50 year PGAs up to 0.26g. However, for higher seismic hazard areas, Reneckis and LaFave (2009) recommend improved methods to connect the veneer and wood backup.

1.4 Purpose Of Current Research Study

Although past research studies, such as those presented in Section 1.2, have investigated the seismic performance of seismically-detailed and non-seismically-detailed brick veneers, the uniqueness of the seismic activity and building stock in the Texas and Oklahoma region motivated the need for further research. This research, funded by the Center for Integrated Seismic Research (CISR) and the TexNet Seismic Monitoring Program, aims to better understand the potential seismic vulnerability of brick veneer facades, which are prevalent in Texas residential construction, under ground motions that are representative of those experienced in Texas and nearby states.

The purpose of the study is to build upon existing knowledge of brick veneer construction and behavior to investigate the response and potential for damage under seismic activity specific to the region of interest. To this end, this study utilized computational models, based on those from previous research, and a suite of recent ground motion records from Texas, Oklahoma, and Kansas, to then develop fragility curves for wood-backed brick veneer walls specifically located in that region. In addition, researchers investigated how common construction errors associated with brick veneers impact the resultant fragility curves. The resulting fragility curves allow for better predictions of the likelihood and level of damage that could be expected for residential construction in this region based on a given level of shaking intensity (e.g., peak ground acceleration, PGA). Analyzing the effects of various common installation errors on veneer fragility provides a more realistic view of the brick veneer wall performance in the existing building stock, as well as increases understanding of what aspects of installation are most critical to wall performance. In this study, experimentally-validated computational models are used to

evaluate the seismic performance of masonry veneers under a wide range of ground motions, and construction details, to develop the fragility functions.

Chapter 2: Computational Model Creation and Validation

Chapter 2 details the process of creating the OpenSEES veneer wall model used in the current study. The OpenSEES models developed in this project were based on the modeling approaches recommended by Reneckis and LaFave (2009) and were validated using the experimental data from the same study. This chapter first presents the experimental tests and the finite element (FE) modeling approaches developed by Reneckis and LaFave (2009) in Section 2.1. The experiments included both cyclic tests on veneer tie subassembly specimens and dynamic shake table testing of full-scale wall panel specimens. For modeling the behavior of the brick veneers, the brick ties, which are the primary source of nonlinearity in the brick veneer system and typical govern veneer performance, are modeled using nonlinear uniaxial truss elements. The other elements of the veneer-wall system (e.g., the bricks, the 2x4 studs, and the OSB panels) are modeled using a combination of shell and beam-column elements. Sections 2.2 and 2.3 outline how the Reneckis and LaFave (2009) veneer tie and wall panel models, respectively, were adapted in OpenSEES and validation of the proposed model with the available experimental data. The experimentally validated computational models are then used to evaluate brick veneer damage states as proposed by Reneckis and LaFave (2009) and described in Section 2.4.

2.1 Original Reneckis Experimental Tests And Model

Two wall specimens were experimentally tested in the previous Reneckis and LaFave (2009) study under out-of-plane dynamic loading on a shake table. The two specimens were each tested with different types of veneer ties—28-gauge with minimum code allowable installation eccentricity and 22-gauge with maximum code allowable installation eccentricity, referred to as 28ga(min) and 22ga(ecc), respectively. Wall 1 was built entirely of 28ga(min) veneer ties. Wall-

2 was constructed from Wall-1 (28ga(min) ties), after it failed at the top two rows of ties, by rebuilding the top of the wall and adding two rows of 22ga(ecc) ties. A summary schematic of the wall specimens is shown below in Figure 2.1, which is from the Reneckis and LaFave (2009) study, to demonstrate the wall specimen setup and tie layout. It was assumed that the remaining veneer ties in Wall-1 had remained elastic and were considered undamaged when constructing Wall-2. The collapsed portion of Wall-1 was removed, new 22ga(ecc) ties installed in the top two rows, and identical brick and mortar put back in place. Both Wall-1 and Wall-2 were subjected to the same Wen and Wu (2001) synthetic ground motions representing a 10% in 50-year hazard level in the New Madrid region, as well as 2% in 50-years. However, the focus of the results from the previous study were from testing with the 10% in 50-year event time history; therefore, it was used as the basis of validation for the current study, which will be shown in Sections 2.2 and 2.3.

As shown in Figure 2.1, the wall specimens were constructed on a shake table and supported by a system of steel beams and tension rods to keep it upright, which was attached to the stud wall. Figure 2.1 also shows the underlying tie layout, which was utilized for both Wall-1 and Wall-2 experiments, because it is the code required tie spacing, as discussed in Section 1.2.

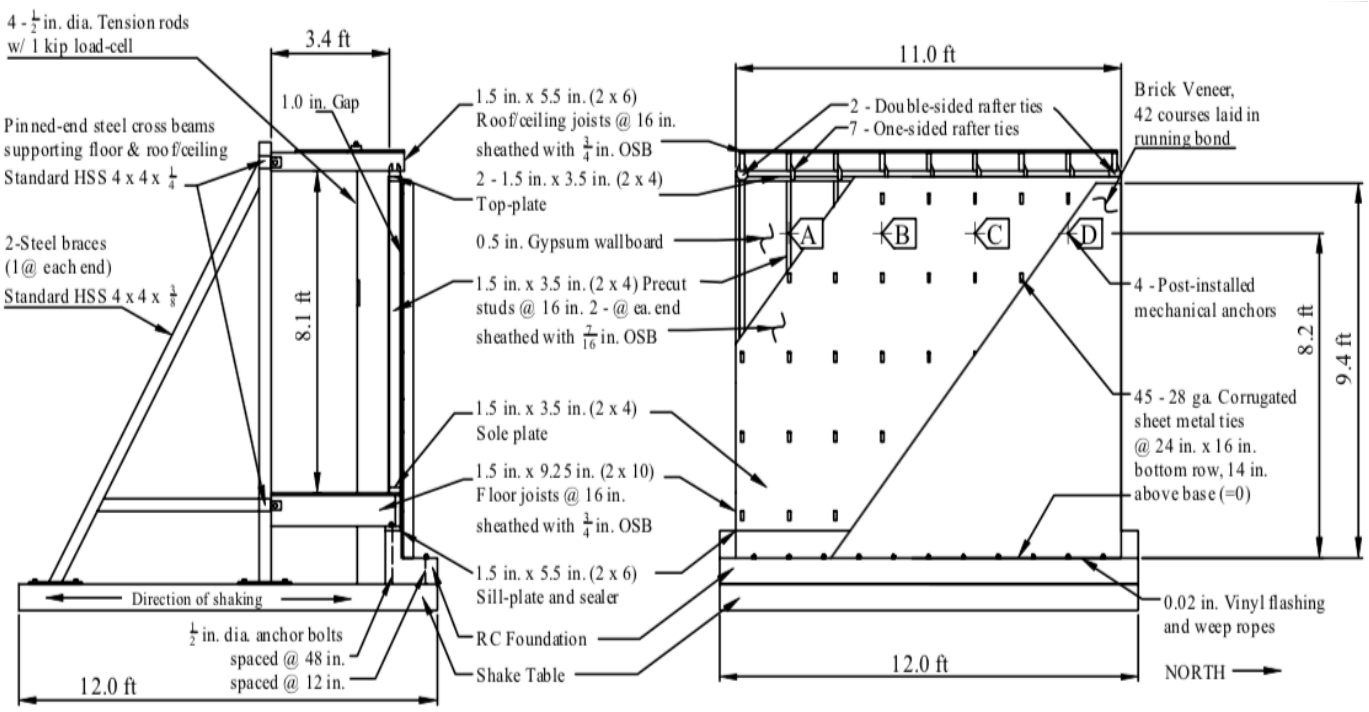

Figure 2.1. Experimental wall specimen setup (schematic from Reneckis and LaFave, 2009)

Figure 2.2(a) and (b) shows a schematic of the brick veneer wall panel that was tested by Reneckis and LaFave (2009). Figure 2.2(c) displays the rendering of the 3D full wall finite element (FE) model that Reneckis and LaFave (2009) developed to simulate wall behavior, mentioned in Section 1.2. As in the previous Reneckis and LaFave (2009) study, the full wall was scaled down to a wall strip model, shown in Figure 2.2(d), to increase computational efficiency when executing hundreds of nonlinear response history analyses.

The Reneckis and LaFave (2009) study utilized ABAQUS to build the veneer model; however, OpenSEES was chosen for the current model because of the open-sourced software's capabilities in regards to specifying individual material properties or behaviors and its computational efficiencies in nonlinear response history analyses. Both models were similarly made up of shell, beam, and spring elements. A key difference between the models was the material properties assigned to simulate the brick tie hysteretic behavior, where alterations were

made to the OpenSEES model to match experimental results from previous brick tie subassembly and full wall panel tests.

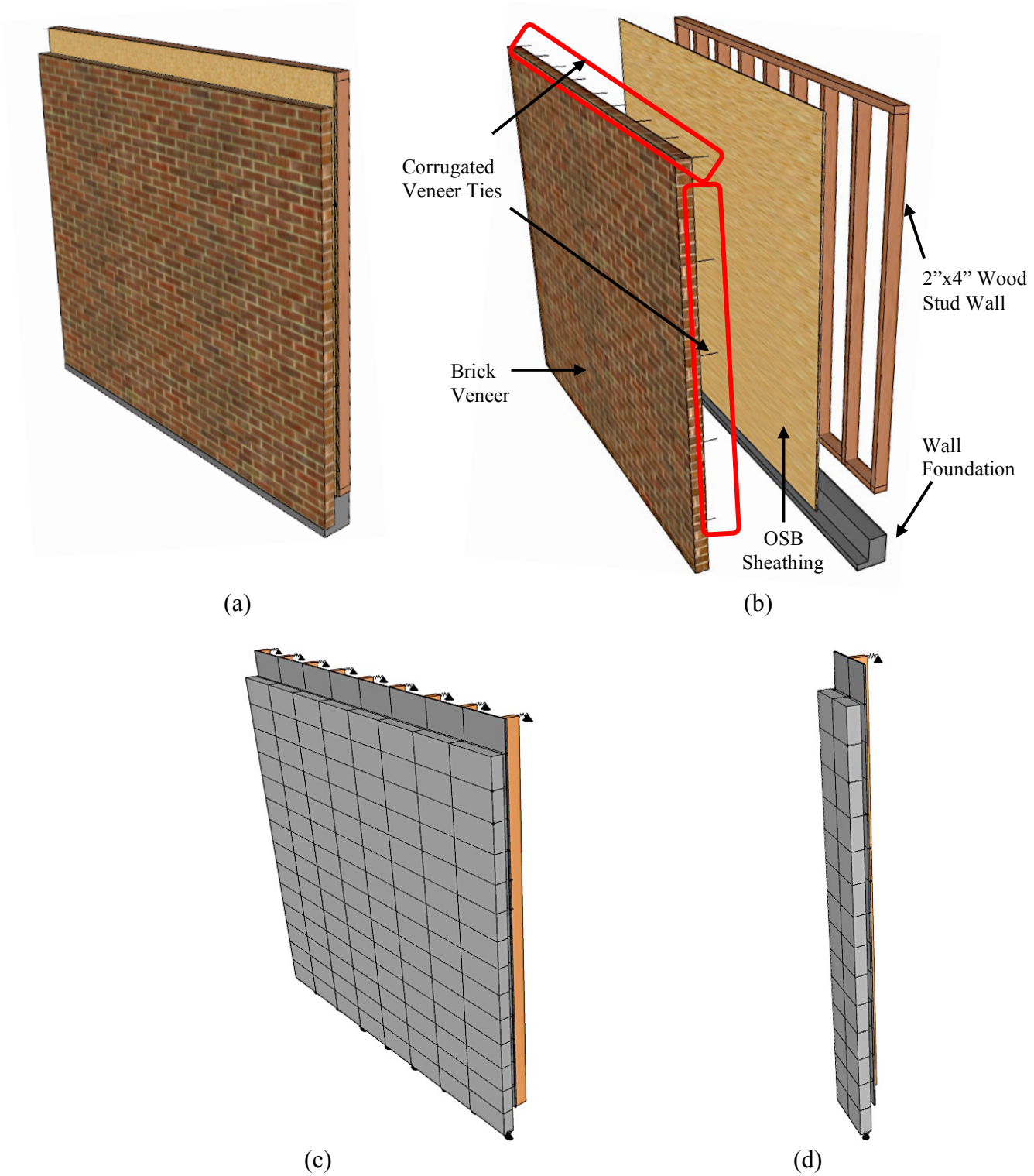

Figure 2.2 Renderings of brick veneer wall: (a) Actual wall as constructed, (b) Actual wall with individual elements labeled, (c) FE veneer full wall model, and (d) FE strip wall model.

In order to experimentally determine the cyclic behavior of a certain type of brick veneer tie, Choi and Reneckis (2004) created experimental subassemblies, shown in Figure 2.3, out of the exact same materials used to build the full-scale wall specimens. Approximately 210 subassemblies were tested by monotonic and cyclic out-of-plane loading. The goal was to evaluate the stiffness, strength, and failure mode of the mortar-tie-fastener system itself, rather than just a single tie without any attachment. Reneckis and LaFave (2009) proposed uniaxial hysteretic models to simulate tie behavior, based on these tests. These hysteretic models served as the basis of the current study, with some modifications, as will be discussed in the following sections.

Figure 2.3. Tie subassembly test setup. (Reneckis, 2009)

2.2 OPENSEES TIE MODEL DEVELOPMENT AND VALIDATION

The nonlinear behavior of the corrugated veneer tie subassembly is simulated as an axial element in the computational models in the previous Reneckis and LaFave (2009) study as well as the current study. The nonlinear tie behavior was initially based on results from the brick tie subassembly tests and were later validated and modified, as need, using data from the full wall panel tests. Truss elements were utilized in OpenSEES to represent the corrugated veneer ties that connect the brick veneer wall back to the OSB sheathing and stud wall. Uniaxial hysteretic materials were defined for each individual type of tie that was studied.

Only 28-gauge and 22-gauge ties were studied because the full-scale walls, from the previous study, were initially built with 28-gauge ties, and 22-gauge are the minimum code compliant veneer ties. In addition, one of the goals of the current study was to most accurately represent the quality of construction of real brick veneer walls, so no thicker than 22-gauge ties were considered. The hysteretic backbones of both tie gauges, at both the minimum and maximum eccentricities, 5/32 in. and ½ in., respectively, are shown in Figure 2.4. When referring to a certain type of veneer tie, both the gauge and installation eccentricity are used. For example, 28ga(min) refers to a 28-gauge tie installed with the minimum code allowable eccentricity, which is 5/32 inches, as mentioned previously. A 28ga(ecc) tie is also a 28-gauge tie, but installed with the maximum allowable eccentricity of ½ inches. Figure 2.4 shows the backbones from both the current study and those utilized in the previous FE model from Reneckis and LaFave (2009). The experimental data included in the plots is the average from all the cyclic tests conducted for each tie type. The goal was to best replicate both the overall behavior and the maximum strength values of the cyclic average subassembly curves. The specific force-displacement values for each backbone can be found in Appendix B.

The resultant OpenSEES backbones in Figure 2.4 closely match the initial stiffness, as well as the maximum tie strength and displacement at which that occurred during cyclic out-of-plane loading. As shown in Figure 2.4, the OpenSEES models used in the current study deviate slightly from the previous Reneckis and LaFave (2009) FE model backbones in order to more closely match the cyclic subassembly behavior.

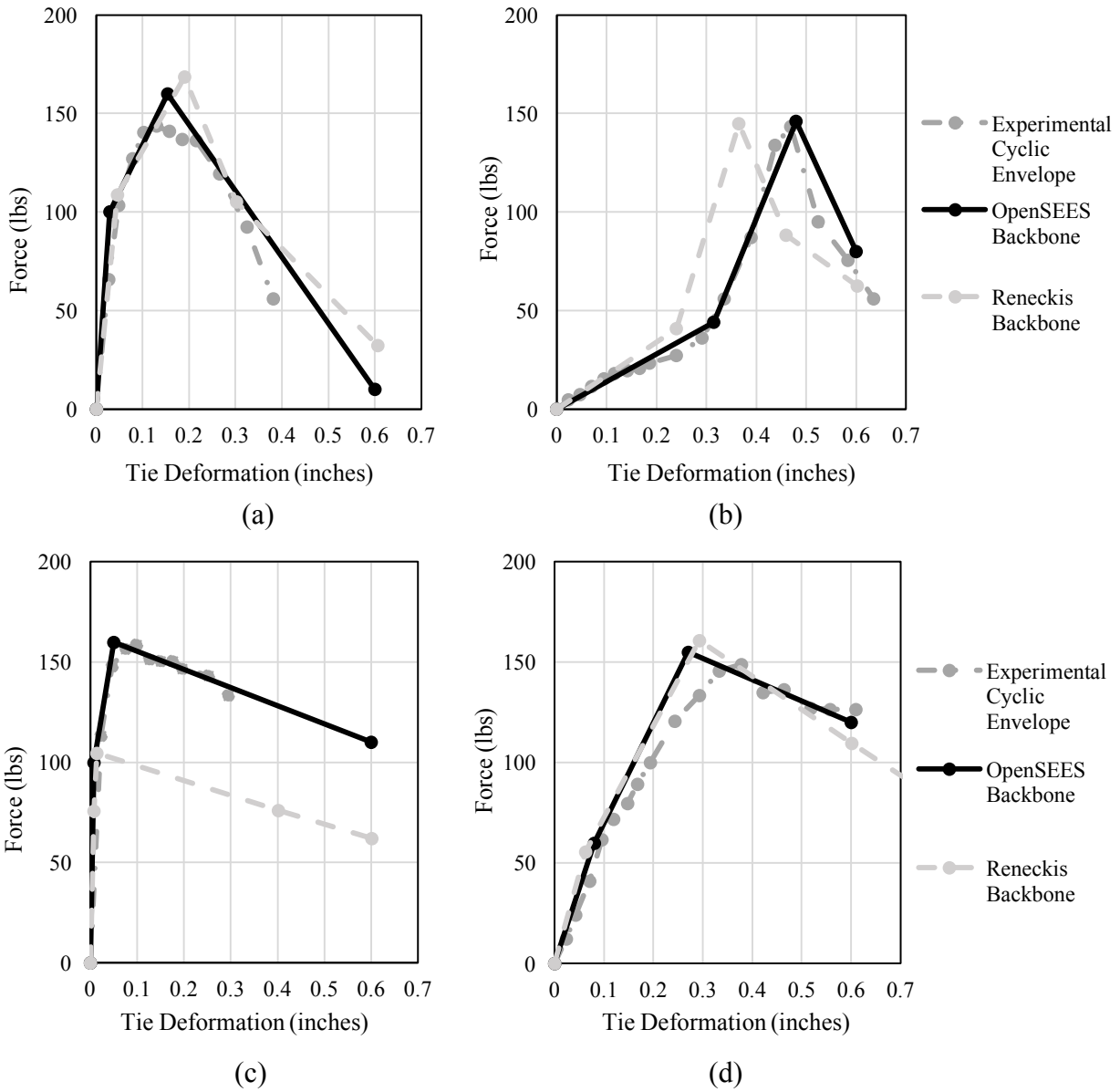

Figure 2.4. Veneer Tie Hysteretic Backbones in OpenSEES for different tie types: (a) 28ga(min), (b) 28ga(ecc), (c) 22ga(min), and (d) 22ga(ecc).

The actual cyclic behavior of the ties is demonstrated in Figure 2.5, for both 28ga(ecc) and 22ga(ecc) tie types, because the experimental subassembly cyclic loading and unloading data were available. The backbones presented above were combined with hysteretic unloading and reloading rules using the pinching variables in the Hysteretic material available in OpenSEES. In the x-direction, pinching parameters were defined as 1.0 and 0.85 for 28-gauge and 22-gauge

ties, respectively. The y-direction pinching for both tie gauges was defined as 0.3. The pinching values were determined by comparing the loading and unloading behavior of the cyclic plots to those produced in the experimental subassembly tests. The replication of the subassembly cyclic behavior is shown for 28ga(ecc) by comparing Figure 2.5(a) and (b), as well as in (c) and (d), for 22ga(ecc) ties.

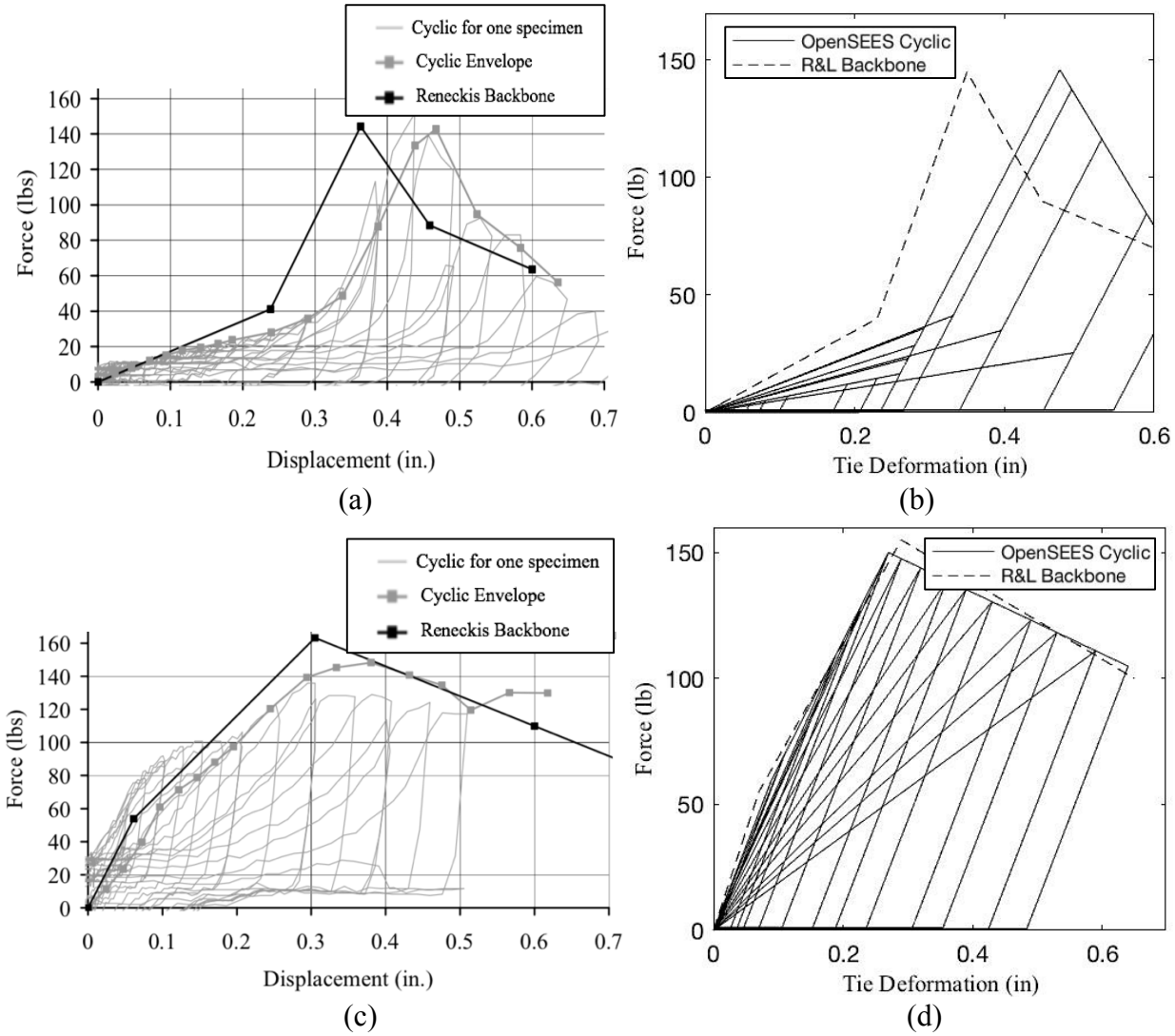

Figure 2.5. Cyclic behavior of tie subassemblies and OpenSEES hysteretic material for veneer ties: (a) experimental 28ga(ecc) subassembly, (b) 28ga(ecc), (c) experimental 22ga(ecc) subassembly, and (d) 22ga(ecc).

The subassembly testing focused on loading the ties cyclically in tension. Compression response of the ties was ignored, as it was assumed that mortar droppings behind the wall would

provide a direct compressive load path from the brick veneer to the backing structure. Thus, the tensile tie behaviors described above were combined in parallel with an elastic-no-tension material with a very stiff response in compression.

To simulate complete tie failure, as was observed in the wall panel tests, a failure criterion was defined to remove the tie from the model, making it ineffective. In the previous Reneckis and LaFave (2009) study, the tie elements in the FE model were manually removed from the model after they were observed to reach their peak capacity. In OpenSEES, the built-in MinMax function was used to automatically "remove" an element from the model after it reaches a specified displacement limit. Based on the manual tie element removal approach used in Reneckis and LaFave (2009), the displacement limits were set to the displacement at which the peak strength occurred for each type of tie as given in Table 2.1. These tie displacement limits were validated based on the full wall panel models, particularly noting the excitation levels that induced a very large increase in brick displacement, indicating collapse

Table 2.1: Tie displacement limit values.

Veneer Tie Classification	Displacement Limit (inches)
28ga(min)	0.17
28ga(ecc)	0.48
22ga(min)	0.08
22ga(ecc)	0.27

The validation of the tie limits in Table 2.1 was done by applying the tie model into a strip model to simulate the response of a full wall panel. More details on the strip model can be found in Section 2.3. For purposes of the tie displacement limit validation, the peak brick veneer and backup displacements of the OpenSEES strip model were compared to the correlating values from Wall-1 and Wall-2 experimental tests, shown in Figure 2.6, to observe when the ground motion intensity that caused the experimental specimens and computational models to collapse.

The OpenSEES models for 28ga(min) and 22ga(ecc) tie types were validated by comparing plots of the maximum veneer and wood backup displacements vs. scaled PGA input. The ground motion time history, which was scaled to incremental PGA values, was the same as that utilized for the experimental tests and Reneckis FE model validations. The models were subjected to scaled time histories that produced varying levels of wall damage based on the intensity of the input record. In order to best simulate response to individual seismic events, the computational model was subjected to scaled input records that were increased by 0.1g each run. The plots for models with both tie types is shown in Figure 2.6. The plots include the displacement behavior for the wall models if no MinMax command was used in OpenSEES to designate the tie displacement limits, from Table 2.1, and the ties were allowed to follow the entire backbone for each from Figure 2.4. As observed in Figure 2.6, the models with the displacement limits were able to replicate the sharp increase in displacement shown in the two experimental wall specimens.

The 28ga(min) tie type was able to be compared directly to Wall-1 because the specimens had been constructed with that type of tie. However, no wall panel was originally constructed entirely with 22ga(ecc) ties. Therefore, the validation of the 22ga(ecc) backbone was done by replicating the Wall-2 specimen construction process in OpenSEES, in which the top two rows of ties in the wall panel were built with 22ga(ecc) ties, and the rest of the ties below remained as the original 28ga(min) ties. The displacement vs. scaled PGA behavior was compared to both the Wall-2 experimental test results and the Reneckis FE model that was tested utilizing 22ga(ecc) ties. The results indicate that the OpenSEES model with the MinMax tie displacement limits are able to better match the experimental results compared to the Reneckis and LaFave (2009) model and the OpenSEES model without the MinMax tie displacement limit.

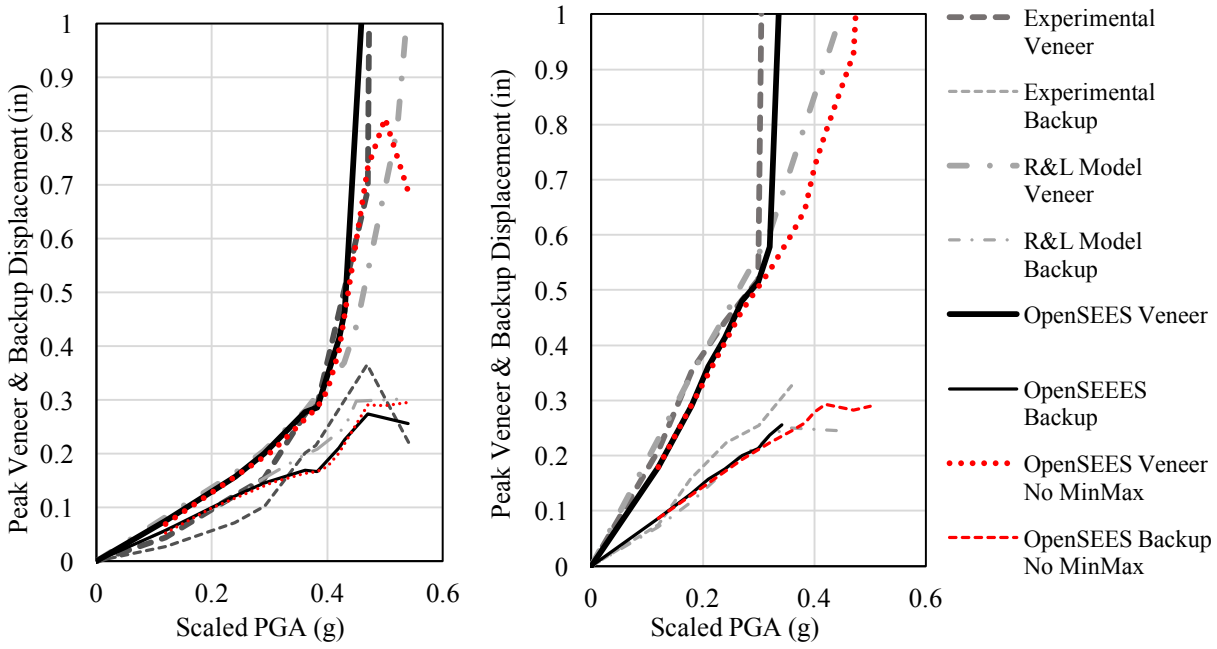

Figure 2.6. Validation of use of displacement limits for tie backbones based on comparing OpenSEES and experimental peak displacement data for specimens: (a) Wall-1 and (b) Wall-2.

It should be noted that for displacement plots in the current study, such as Figure 2.6, the scaled PGA values used to plot the results are the nominally scaled PGA values used as inputs for the previous experimental testing. In the previous study, the measured PGA values were found to vary slightly from those of the input ground motions, due to random spikes in acceleration outputs from the shake table. Therefore, the scaled PGA values, which are used here, better represent the actual intensity of shaking experienced by the experimental specimens.

2.3 OPENSEES STRIP MODEL DEVELOPMENT AND VALIDATION

Figure 2.7 shows each wall component labeled with the OpenSEES elements used in the computational model. The small rotational and lateral spring supports are enlarged in the rendering for better detail, but are zero-length elements in the model. The OpenSEES strip model was validated by subjecting the model to the same ground motion time history that Reneckis and

LaFave (2009) used for the full-scale experimental tests, and then comparing the resultant behavior.

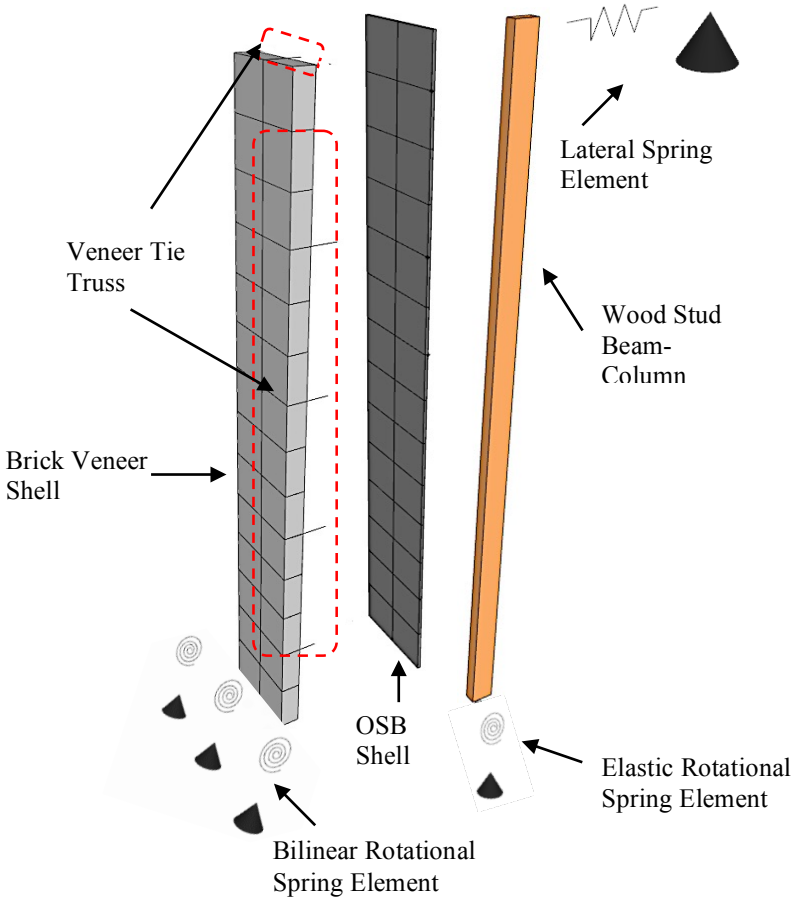

Figure 2.7. Exploded view of strip model with individual OpenSEES elements labeled.

2.3.1 Elements In OpenSees Model

2.3.1.1 Shell Elements

Shell elements were utilized to create both the brick veneer and the OSB sheathing. Shell elements in OpenSEES are able to have a small, designated depth, and have degrees of freedom in in-plane and out-of-plane directions. The material properties for both the brick veneer and OSB were taken from those utilized in the previous Reneckis and LaFave (2009) study. The property values are shown in Table 2.2 and are based on typical standard values for standard

"Colonial Red" bricks, Type N mortar, and typical OSB sheathing. The shell elements in OpenSEES were assumed to remain elastic with the constant values provided in Table 2.2, and all out-of-plane nonlinearity in the wall is assumed to be concentrated in the brick ties and rotational spring at the base of the wall, as described below.

Table 2.2: Shell element material properties.

Shell Element	Elastic Modulus, *E* (ksi)	Poisson's Ratio, *v*	Density, ρ (pcf)	Thickness (in)
Brick Veneer	2000	0.2	115	3.5
OSB Sheathing	930	0.4	72.4	7/16

The elastic modulus and Poisson's ratio for brick veneer in Table 2.2 was determined by Reneckis and LaFave using brick prism and mortar cube samples, which were cured for 28 days and tested following standardized ASTM procedures to determine compressive strength, modulus of elasticity, and modulus of rupture. For each full wall specimen built, five prism tests were conducted and the material values averaged. Elastic modulus, which is the property required for OpenSEES shell elements, was determined per ASTM E111 (2002). The mortar cube compression and flexural strength tests followed ASTM C780 and ASTM E518, respectively (2002). The material property results were compared to the MSJC specifications and were found to meet 2008 code requirements with Type N mortar. The elastic modulus and density for the OSB sheathing were chosen as those specified by NDS (2001).

It should be noted that because the brick veneer was modeled as linear elastic shell elements, no inelastic behavior, such as out-of-plane failure in the mortar joints, was accounted for in the actual brick veneer model. Reneckis and LaFave (2009) investigated the use of elastic-plastic nonlinear hinges between veneer element nodes to simulate the effects of cracking in the mortar. While they found that this modeling approach was capable of capturing performance of the brick veneer at cracking, they ultimately decided not to include these nonlinear brick

cracking springs in their proposed model, because, as they state, "the most important features of the brick veneer wall performance were effectively represented through utilizing detailed nonlinear FE models for the tie connections" (Reneckis and LaFave, 2009). Based on this recommendation, the inelastic rotational springs to simulate cracking within the veneer, were not included in this model as they were not necessary for the purposes of this study.

2.3.1.2 BEAM-COLUMN ELEMENTS

The wood 2x4 studs were modeled in OpenSEES using elastic beam-column elements. The material properties were also taken from the values used in the previous study, which were determined from code specifications and experimentally measured weights. The elastic modulus and density were chosen as those specified by NDS (2001). The material properties designated for the wood studs are shown in Table 2.3, and are also what was utilized in the current study for the OpenSEES beam-column elements.

Table 2.3: Wood stud material properties.

Element	Elastic Modulus, E (ksi)	Poisson's Ratio, v	Density, ρ (pcf)
Wood Stud	1200	0.4	26.2

In addition to the property values in Table 2.3, beam-column elements in OpenSEES also require the designation of weak- and strong-axis moments of inertia (I_{yy} and I_{zz}, respectively), shear modulus (G) of 667 ksi, and polar moment of inertia (J) of 6.343 in^4. The additional element inputs were determined from the area and cross section of a 2x4 wood stud. As previously mentioned in Section 1.2, only out-of-plane shaking was studied, therefore, the axis of bending for the studs was horizontal, parallel to the width of the veneer wall. In addition, as shown in the rendering of the real veneer wall in Figure 2.2(b), horizontal 2x4 top and sole plates

are placed at the top and bottom, respectively, of the vertically oriented studs, in order to complete the stud wall subassembly and provide stability. Therefore, the OpenSEES model also included a horizontal wood stud beam-column element at the top and bottom of the row of vertical studs. The horizontal studs had the same material properties as those of the vertical, except for the orientation specified within the model. As shown in Figure 2.7, the stud boundary conditions included a pinned rotational spring at the bottom of each stud to simulation rocking behavior at the base of the wall and a pinned out-of-plane lateral spring at the top of the stud assembly to simulate the lateral resistance provided by the entire structure. The specifics of the spring elements are discussed in Section 2.3.1.3 and 2.3.1.4.

2.3.1.3 LATERAL SPRING ELEMENTS

The lateral restraint spring is shown in Figure 2.7(b). The purpose of the spring is to represent the connection of a real stud wall back to the rest of a structure with a defined lateral stiffness, which is assumed to behave elastically during a seismic event. As shown in Figure 2.7(b), the lateral spring was oriented out-of-plane to the wall. The OpenSEES element was designated as uniaxial linear elastic, with a stiffness of 1.7 k/in, which remained constant throughout the current study. Lateral spring supports were chosen to represent the boundary condition at the wall top because in the full-scale experimental tests, Reneckis and LaFave (2009) restrained the wall with a steel support frame and rafters, in the out-of-plane direction, which did not provide significant rotational resistance. In the previous study, the spring stiffness values were determined first for a full-scale wall model, based on comparing computed static load test displacements to those observed in the experimental tests. The lateral resistance springs at the top corners of the wood backing of the full wall panel were determined to have a higher stiffness than the remaining springs due to the presence of the support frame behind the wall

panel, visible in Figure 2.1. However, as shown in Figure 2.7, the strip model only included a single lateral resistant spring. In order to determine the required singular spring stiffness, Reneckis and LaFave (2009) took a weighted average of the springs from their original full wall FE model, shown in Figure 2.2(c). The single spring stiffness in the previous study was determined to be 1.4 k/in and was used as an initial basis for the lateral resistant spring in the OpenSEES model. However, the final lateral resistance spring stiffness value for the current study was determined to be 1.7 k/in. The increase in stiffness occurred during the model calibration phase when it was observed that the OpenSEES model with the higher spring stiffness actually better replicated the displacement behavior of the backup stud wall than with the smaller stiffness.

2.3.1.4 ROTATIONAL SPRING ELEMENTS

Two different types of rotational springs were utilized as base supports for the computational model. Rotational springs present at the stud bases were only considered to have elastic behavior, with a stiffness of 1000k-in/rad, based on experimental wall behavior. The stiffness value was determined in the Reneckis and LaFave study by comparing the displacements from static tests on the computational model to those measured from the experimental tests. The elastic rotational stud support springs were used to simulate the rotational restraint provided by the OSB fastened to the sole plate. Rotational springs were included at the base of the stud wall because experimental testing found that the OSB sheathing added rotational resistance to the stud wall backing.

In addition, rotational springs were also included in the model at the base of the brick veneer because in experimental testing, the brick wall was found to pivot around its base and exhibited some rigid body rocking response. In order to represent the rigid body rocking

behavior, the brick veneer rotational springs were given bilinear force-displacement behavior, as was done in the previous study. The bilinear behavior was defined in studies by Doherty et al. (2002) and Simsir (2004), based on the veneer wall weight and geometry. Translational degrees of freedom at the base of the brick veneer and stud wall were restrained. An example of the type of bilinear elastic behavior assigned to the base rotational springs is shown in Figure 2.8.

The M_{max} and θ_{max} designated for the specific brick veneer wall in the strip model were defined in OpenSEES as 1,330 lb-in and 0.045 radians, respectively. Unlike the brick veneer wall, which was given the behavior in Figure 2.8, the rigid body rocking behavior was observed to not be significant for the wood stud wall due to the tie downs provided to the foundation.

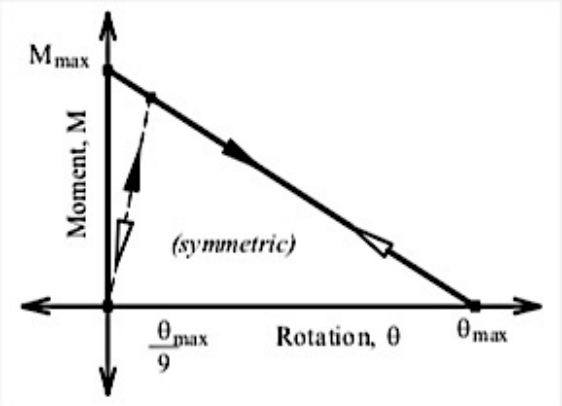

Figure 2.8. Bilinear rotational spring behavior model. (Reneckis, 2009)

2.3.2 SEISMIC MASS

Seismic masses are included for each element in OpenSEES by designating the material density for each individual component in the model. The shell element mass is distributed based on the specified shell dimensions and shell material density. The nonlinear beam-column elements, used for wood studs, also utilized the material density and to distribute mass along the height of the stud within OpenSEES. An additional lumped mass was added to the top of the

veneer where the last tie was located. The lumped mass accounted for the additional bricks in the top few rows of the veneer wall that were above the top tie. A total of 0.14 lb-s^2/in was added to the model node where the last tie was located to account for the topmost bricks of the veneer wall. No additional gravity loads were applied to the model, as geometric nonlinearity was not considered in the analysis.

As determined in the previous study, a 4% damping ratio was designated for Rayleigh damping, for the first and second modes, for the dynamic response history analyses. In OpenSEES, a Uniform Excitation load was defined to subject the model to the acceleration time history input file, with a time step of 0.01 seconds. The earthquake excitation is applied to all support nodes in the direction designated in OpenSEES, which was out-of-plane for this study. Figure 2.9 shows the OpenSEES model with the defined dimensions and tie locations utilized for analysis.

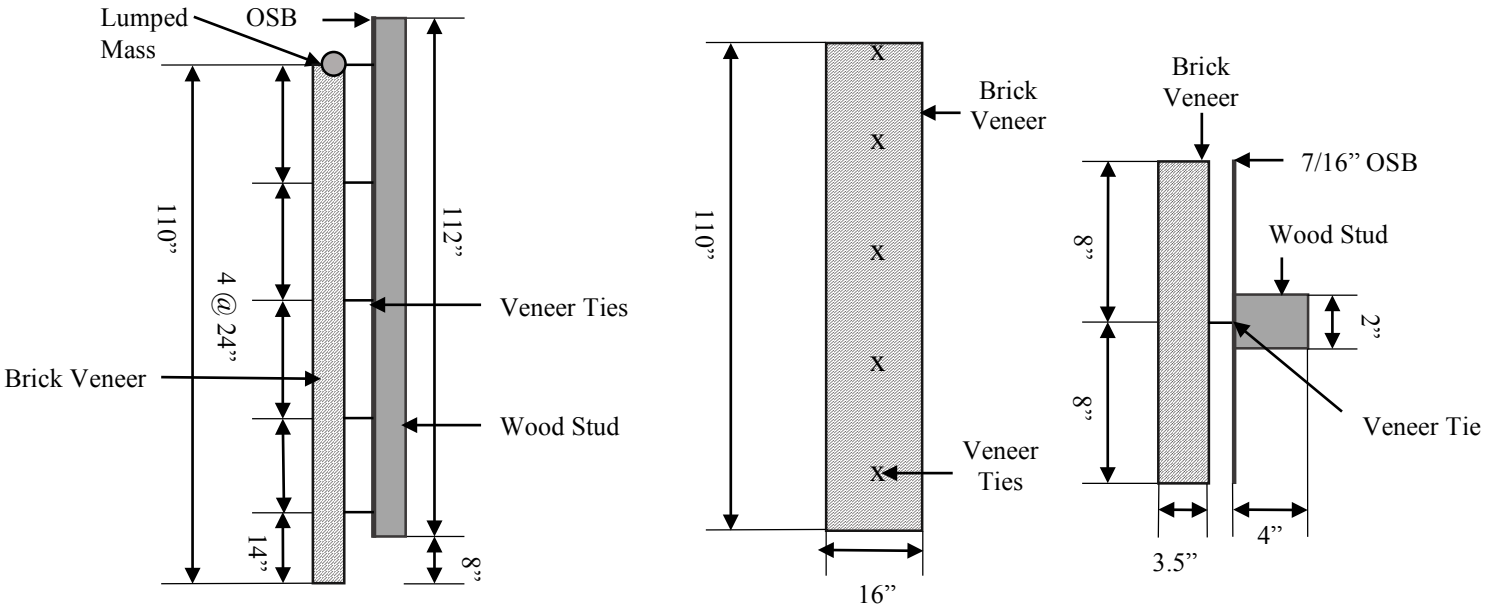

Figure 2.9. Dimensions of OpenSEES Model as Loaded for Analysis: (a) side, (b) front, and (c) top.

2.3.3 OpenSEES Strip Model Validation

The key response parameter of interest in both the previous and current study was the veneer tie deformation because damage and wall stability are determined by how long the veneer stays connected to the supporting wood stud wall. The tie backbones and cyclic behavior from Figures 2.4 and 2.5 were first validated by comparing each to the corresponding subassembly behavior data as described in Section 2.2. The backbones were then used within the actual strip wall model, for each type of tie, and were validated by conducting static and dynamic tests on each wall model, which were compared to wall displacement results from experimental static and dynamic tests of the full wall panel.

The ground motion utilized to conduct the dynamic OpenSEES model tests was a synthetic 10% in 50-year event for Memphis, Tennessee, with a PGA of 0.059g, from the Wen and Wu (2001) ground motion set, because this was the same time history used by Reneckis and LaFave (2009) for experimental and computational model testing. The time history was chosen from a suite of 20 synthetic, 10% in 50-year events representative of New Madrid seismic hazards, and then utilized for both experimental and FE model testing. The OpenSEES strip models were initially subjected to shaking levels that would not result in tie damage, and the displacements vertically up the wall were compared to those of Wall-1 and Wall-2 for full-scale wall dynamic tests, shown in Figure 2.10.

Both the experimental and OpenSEES models of the veneer wall, included in Figure 2.10, show similar behavior up the height of the wall. The displacement results are solely from one synthetic ground motion time history, but was included to show the overall wall behavior before any tie failures occurred. Results from testing Wall-1 in Figure 2.10(a) were obtained by scaling the acceleration time history, with an original PGA of 0.059g, up to 0.38g, which had

experimentally been determined to be the end of the elastic range, where the first tie would fail. The displacement profiles in Figure 2.10 are at the time where the top of the OpenSEES veneer wall model reached its peak displacement. The behavior up the height of the Wall-2 specimen also closely follows that of the OpenSEES computational model. The Wall-2 displacement results in Figure 2.10(b) are compared to an experimental test that was only scaled to 0.18g. The intention was to document displacements at the end of the wall elastic behavior range, before the first tie failed, and Wall-2 became unstable at lower PGAs than for Wall-1, thus the displacement profiles are shown for a lower PGA level. The minor variations between the two computational models and the actual wall specimens, in Figure 2.10, can be attributed to slight differences in real tie stiffness values, as well as alterations made to the OpenSEES tie backbones when following the subassembly experimental results, as discussed in Section 2.2.

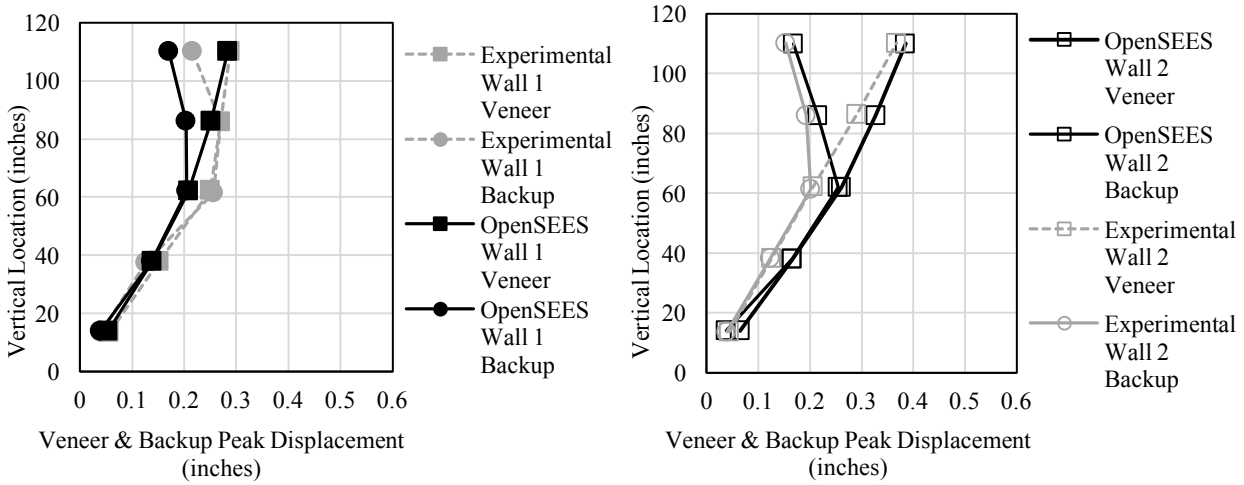

Figure 2.10. Veneer and wood backup peak displacements along length of wall for experimental walls and OpenSEES model subjected to 10% in 50yr motion with PGA=0.059g scaled to corresponding experimental values: (a) Wall-1 scaled to a PGA of 0.38g and (b) Wall-2 scaled to a PGA of 0.18g.

Figure 2.11 shows the displacements at the top of the brick veneer and of the wood backup for different levels of shaking intensity for both Wall-1 and Wall-2 specimens. The figure compares the results from the two experimental specimens, the previous Reneckis model,

and the current OpenSEES model. The close correlation, in Figure 2.11(a) and (b), between the OpenSEES models and the experimental wall behaviors and displacement values, validated the veneer wall model as a whole, as well as the individual tie backbones used within the model. No full experimental wall was constructed using solely 22ga(ecc) ties, therefore, Wall-2 was the most accurate experimental data available to validate the hysteretic 22ga(ecc) behavior.

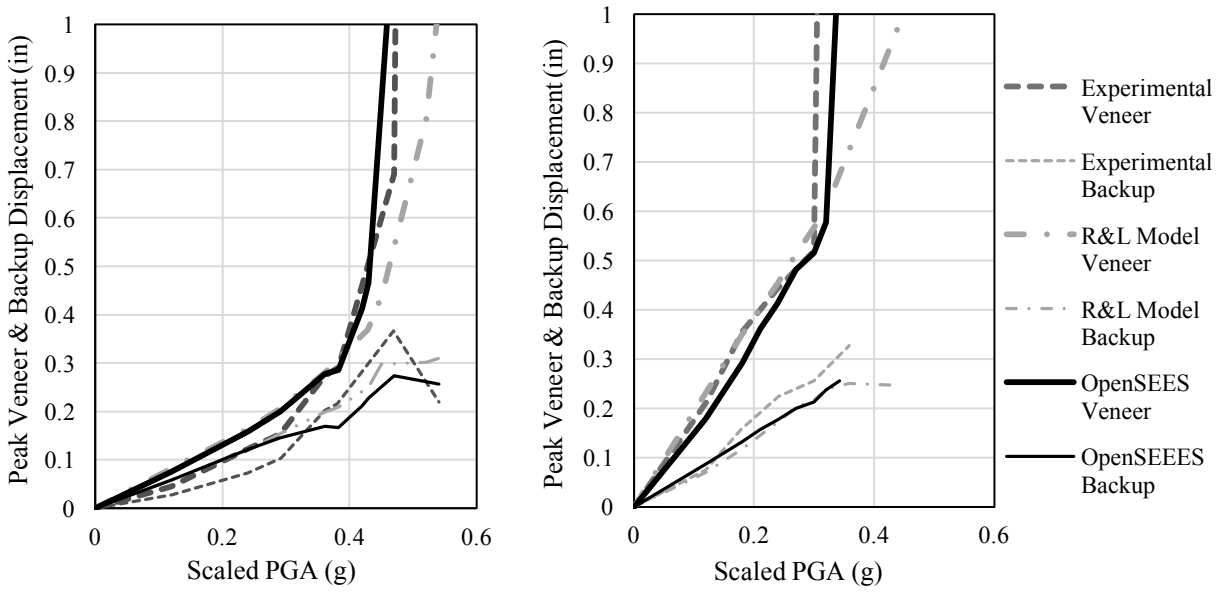

Figure 2.11. Comparison of OpenSEES model peak displacements to experimental and previous FE model results for both solid panel walls from previous experimental tests: (a) Wall-1 and (b) Wall-2.

2.4 DAMAGE STATES

To use the computational models to assess brick veneer fragility, the models must be capable of predicting the occurrence of damage. Two damage states were chosen for the current study to classify the brick veneer damage, specifically repairable damage and wall instability or collapse. Brick veneer damage is directly correlated to the veneer tie deformation, because tie failure directly leads to veneer instability and separation from the backup system. Based on the previous experimental tests, repairable damage (DS 1) correlated with failure of the top row of ties, while wall instability, or collapse (DS 2), occurred after failure of the top two rows of ties

on a wall panel, where tie failure corresponds to the tie exceeding the deformation limits given in Table 2.1. This same method for classifying damage states was utilized in the OpenSEES model and the creation of fragility curves, discussed in detail in Chapter 3.

Figure 2.12 shows the points at which both damage states were reached for the OpenSEES models of experimental Wall-1 and Wall-2. Figure 2.13(a) and (b) both show that after the walls reached Damage State 1, when the top tie fails, there was only a PGA increase of approximately 0.14-0.15g before the wall collapsed. In addition, the changes in slope in the plots also provide an indication of where the changes in damage states occurred. Before Damage State 1 was reached, the wall was considered to have essentially no observable damage because no ties had yet failed. The tie deformation limits for determining the damage states were developed in order to create fragility curves for veneer walls of varying tie types. The process and results from the fragility curves will be presented in Chapter 3.

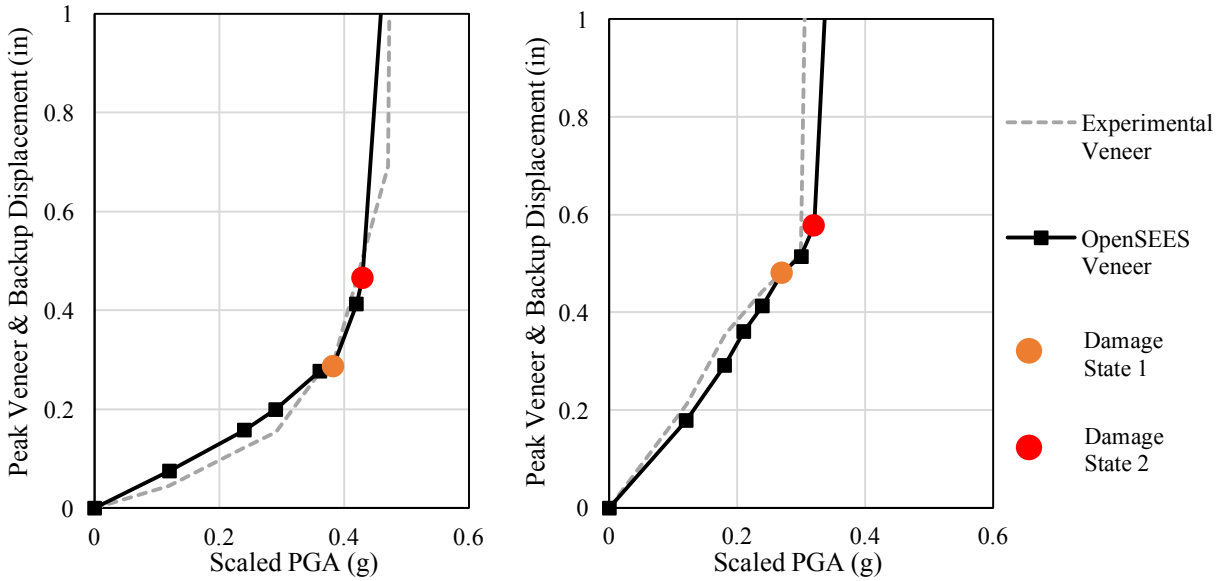

Figure 2.12. Points where Damage State 1 and 2 were reached for OpenSEES and experimental results for (a) Wall-1 and (b) Wall-2.

2.5 CALCULATION OF FUNDAMENTAL PERIODS

The natural periods for the computational models of the Wall-1 and Wall-2 specimens were all computed in OpenSEES. Table 2.4 shows the natural periods for each of the wall models compared to those computed for experimental Wall-1 and Wall-2. The experimental natural period from each wall specimen was determined from free vibration tests. A 300lb load was applied 40 in. from the top of the veneer for Wall-1 and 400lbs at 16 in. from the veneer top for Wall-2. The static loads were released and the natural period determined by the time it took for one full cycle. The natural periods of the computational models were determined from an eigenanalysis. The natural periods in the current study OpenSEES models differed slightly from those computed for the Reneckis and LaFave (2009) FE model natural periods because of the alterations that had been made to the initial stiffness of the tie elements, discussed in Section 2.2.

Table 2.4: Experimental and model wall initial natural periods.

	Experimental Wall Specimen (seconds)	OpenSEES Computational Model (seconds)	Reneckis FE Model (seconds)
Wall-1	0.1	0.125	0.126
Wall-2	0.17	0.131	0.139

The natural periods were recalculated for the OpenSEES model walls after each passed Damage State 1 because the loss of the top tie would alter the stiffness of the veneer model. The second natural period was determined by removing the top tie and then recalculating using the same eigenanalysis as the initial period. As in the previous study, the remaining undamaged ties were assumed to have remained elastic, so there was no reduction in stiffness for those ties when recalculating the natural period. Table 2.5 shows the natural periods for the computational model walls both before and after the first tie failed. As expected, the natural periods of all wall models increased as the wall was damaged and the stiffness of the system decreased.

Table 2.5: Natural period of original models and models after first tie failure.

Veneer Wall Model	Original T_n (seconds)	T_n After DS1 Reached (seconds)
Wall 1	0.126	0.265
Wall 2	0.131	0.269

2.6 CONCLUSION

The computational models in OpenSEES, which were utilized in the current study, were initially based on the modeling done in the previous Reneckis and LaFave (2009) study, with slight modifications to calibrate the model to the experimental wall and tie displacement results. Both the tie hysteretic behavior was validated using available cyclic tie subassembly experimental data, and the brick veneer wall panel model, was validated using shake table testing results subjected to a single ground motion at multiple scale factors. Based on correlations between computational model response and observations of damage during the test, tie deformation was determined to be the key response parameter used to predict damage in the brick veneer. Damage states were established to constitute the limit of repairable damage and wall instability or collapse. The plots presented in this section show that both the behavior of the computational models closely follow those of the experimental walls. These experimentally validated computational models were then utilized, along with the damage state limits, to produce the fragility curves found in Section 3.4.

Chapter 3: Development and Analysis of Fragility Curves

3.1 Definition of Fragility Curves

Fragility curves are used to represent the probability of exceeding a predetermined damage state based on an engineering demand parameter, related to the ground motion to which the element was subjected. An example of a possible engineering demand parameter is deformation of a specific component, such as a veneer tie, which is the parameter used in the current study to determine the damage state of the brick veneer model.

To create a single fragility curve, a sample of twenty ground motion files was chosen to account for uncertainty associated with seismic excitations. The next step in the fragility curve creation process was to scale the ground motions to a range of intensities and subject veneer models to each of the twenty scaled ground motions at each intensity level. For this study, the ground motions were scaled to PGA levels ranging from 0.1g to 2.2g, with increments of 0.1g. At each 0.1g step, the tie deformations of the top two ties were compared to the previously mentioned limit values, in order to determine if at that point the wall correlated to Damage State 1 or 2. Based on how many of the twenty runs at each 0.1g increment resulted in either damage state, that determined the probability then plotted on the fragility curve at that particular PGA value. These discrete points at each PGA level were plotted, and then a lognormal curve fit was used to create the actual curves to be analyzed and utilized in the future. An example of discrete points at 0.1g PGA increments and the corresponding curve fit is displayed below in Figure 3.1.

Lognormal distributions are often assumed for the probabilistic fragility model, which can be defined by two variables, median (μ), and beta (β), which is defined below in Equation 1.

$$\beta = \sqrt{\beta_{MTL}^2 + \beta_{GM}^2} \qquad \text{(Eq. 1)}$$

β_{MTL} = Uncertainty associated with model and tie strength properties*

β_{GM} = Uncertainty associated with ground motions

(*Previous study found range of values to be 0.09-0.37 depending on tie type used, as values express coefficient of variation for subassembly tie strength. (Reneckis, 2009))

The sources of uncertainty in developing the fragility curves for the current study were those associated with the actual ground motions, not the OpenSEES structural modeling parameters. Therefore, for the current study, beta (β) is the same as β_{GM}. Additional uncertainty due to variability of material and structural response could be added in to the fragility curves developed in this study. An updated uncertainty parameter accounting for material and structural uncertainty could be calculated per Eqn. (1) as the square root sum of squares of the beta from the fragility curves presented in this study accounting for ground motion uncertainty, as well as the beta associated with material uncertainty.

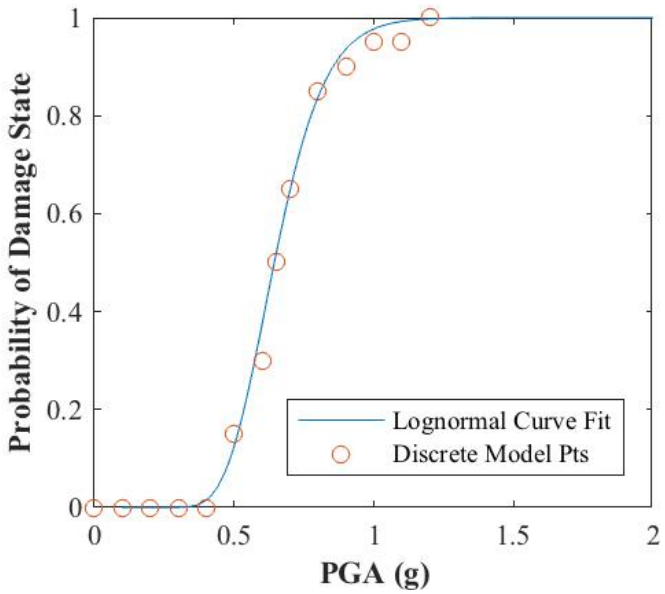

Figure 3.1. Example probability of reaching a given damage state, for discrete 0.1g increments and full curve fit.

3.2 WALL PARAMETERS EVALUATED WITH FRAGILITY CURVES

The primary purposes of this fragility study are to investigate how brick veneer fragility is affected by (i) different ground motion and seismic hazard characteristics, (ii) different brick tie types and layouts, and (iii) different retrofit options to mitigate wall damage. The fragility curves developed in this study are meant to be applicable to residential homes and construction methods found in the Texas and Oklahoma region of interest. The section below describes particular wall parameters that were considered in this study.

The wall strip model discussed in Chapter 2 was used to create the fragility curves in this study. The computational models used in this fragility study are meant to be representative of residential homes, such as those shown in Figure 3.2. The prototypical wood-framed homes that are the basis of this study can take on a wide variety of layouts and dimensions, resulting in a wide range of possible natural periods. Tests by Kharazzi and Ventura (2006) determined a natural period range of 0.19 to 0.55 seconds for a non-engineered two-story wood-frame house,, and experimental tests by Filiatrault et al. (2002) on two-story wood-framed homes had natural periods ranging from 0.15 to 0.25 seconds.

To determine the structural properties to represent the residential home in the fragility study, Reneckis and LaFave (2009) conducted a sensitivity study to determine the impact of the backup structure period on the response of the brick veneer wall. In this sensitivity study, they used an elastic spring and lumped mass attached to the top of the wall model (in series with the lateral spring presented in Section 2.3.1.3) to represent the structural response of the structure. The lumped mass of 14,500kg was used to represent the prototype building, and the stiffness of the structural spring was varied to generate structures with natural periods that were 0.0, 1.0, 1.5, and 2.0 times the natural period of the veneer wall, as determined by the models of the test

panels presented in Section 2.5. Here, a natural period of 0.0 represents a completely rigid structure. From this sensitivity study, they found that structures with natural periods around 1.0 to 1.5 times the veneer natural period exhibited resonance, in which case the amplification of lateral displacements resulted in higher likelihoods of damage and represented a lower bound fragility (i.e., damage occurring at lower shaking intensity levels). The model with the rigid structure (i.e., no additional spring to represent structural flexibility, representing a structural natural period of 0.0) resulted in higher shaking intensities required to cause damage. For this reason, Reneckis and LaFave (2009) determined that their wall panel strip models based on their test setup, which did not represent the flexibility of the house structure, was an effective model for representing the upper bound limit of veneer fragility. For the purposes of the current study in which the models are being used to investigate how different ground motion characteristics or brick tie properties affect seismic vulnerability, the models from the experimental test setup presented in Chapter 2 are used in the following fragility. Based on the recommendations by Reneckis and LaFave (2009), these models are assumed to represent brick veneers attached to an essentially rigid structure and thus result in fragility curves that represent an upper bound limit on the shaking intensities required to produce damage.

To investigate the effects of brick tie type on wall fragility, the two types of corrugated ties tested in the Reneckis and LaFave (2009) dynamic wall panel tests were considered in this study, namely 28 gauge with minimum installation eccentricity and 22 gauge with the maximum installation eccentricity, referred to as 28ga(min) and 22ga(ecc), respectively. These two tie types were studied in depth to better understand the fragility of what is considered the typical gauge and fastener combinations. Table 3.1 shows the different wall models that were utilized to

create fragility curves in order to study the impact of different wall construction parameters and retrofits.

In addition, the choice of focusing on combinations of 28ga(min) and 22ga(ecc) provided the largest amount of available experimental data with which to compare results and validate findings. To investigate the effects of different tie types, Wall #1 and Wall #2 consisted of 28ga(min) and 22ga(ecc) ties, respectively, with code compliant vertical tie spacing of 24 inches. These models were used to evaluate the effects of the two tie gauges, and the type of ground motions to which the models were subjected, as will be discussed in Section 3.4.

In addition to evaluating the effect of tie gauge, through the two code compliant tie spacing models, the impact of tie spacing on the fragility of the wall models was evaluated with Wall#3 and Wall #4. The original 28ga(min) wall model was modified to have larger than code compliant spacing of 48 inches. However, two different layouts, Walls #3 and #4, were evaluated that had 48 inch spaced ties at different locations along the vertical height of the wall. The impact of the larger tie spacing will be discussed in Section 3.4.2.

The impact of simple retrofits was also evaluated by modifying Walls #3 and Wall #4 with tie spacing larger than those specified by the code, mentioned previously. Wall #5 was based on Wall #3, which was “retrofitted” with the addition of a code complaint 22ga(ecc) tie at the top of the veneer wall. Wall #6 was based on Wall #4, but only had the top tie replaced for a code compliant tie since there was already a tie present at the top in the base wall. The effects of the two retrofitted models with be discussed in Section 3.4.3.

Figure 3.2 Representative elevations of model prototype houses for: (a) one story and (b) two stories. (Isoda et al. 2001) (Schematic from Reneckis and LaFave, 2009)

Table 3.1: Wall models used to create fragility curves and evaluate impact of wall parameters.

	#1	#2	#3	#4	#5	#6
Tie Type	28ga(min)	22ga(ecc)	28ga(min)	28ga(min)	28ga(min)	28ga(min)
Vertical Tie Spacing	24”	24”	48”	48”	48”	48”
Additional Comments	-	-	Located at 32” & 80”	Located at 8”, 56”, & 104”	Retrofitted with 22ga(ecc) at wall top	Retrofitted with 22ga(ecc) at wall top

3.3 Ground Motion Suites Used in Fragility Analysis

Two different ground motion suites were used in this study to compare the effects of different seismic hazards on brick veneer fragility. One was a suite of twenty synthetic motions developed by Wen and Wu (2001) to represent ground motions in the New Madrid region. The synthetic motions were developed to specifically represent the seismic hazard in Memphis, TN for probabilities of exceedance of 10% and 2% in 50 years. The records developed for the suite were also developed to represent the seismic characteristics of events within the region and

resulted in synthetic motions of magnitudes of 5 to 8. Of the twenty files in the suite, ten represented a 10% probability of exceedance and ten represented a 2% probability of exceedance in 50 years, all of which had soil conditions that matched the region of interest.

The second suite was provided by researchers in the Center for Transportation Research at the University of Texas at Austin, from 68 recording stations spread over Texas, Oklahoma, and Kansas (Khosravikia et al., 2018). This suite was created by initialing choosing 556 events that occurred after January 2005 and had magnitudes of greater than 3.0. In the previous study, which developed this suite, there was no distinguishing between natural and induced events (Khosravikia et al., 2018). Figure 3.3 shows both the locations of the events and the stations that were included in the suite of ground motions.

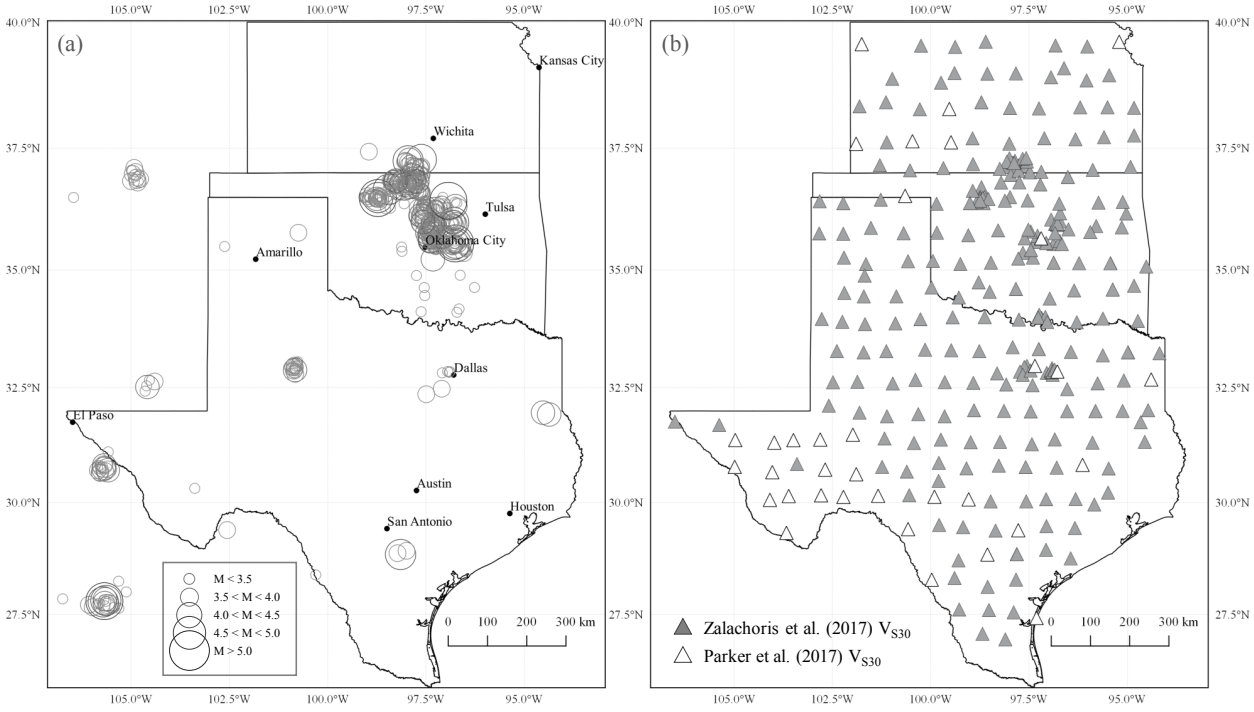

Figure 3.3: (a) Locations and Magnitudes of selected earthquake events, (b) Locations of seismic recording stations in Texas, Oklahoma, and Kansas; distinction of stations with V_{S30} estimates based on Zalachoris et al. (2017) and Parker et al. (2017) (Khosravikia et al., 2018)

The goal in the creation of the ground motion suite was to accurately represent the seismic hazard in Texas. Therefore, out of all of the original 556 events selected, 200 were

chosen that captured high intensity motions with larger PGA (Khosravikia et al., 2018). Figure 3.4 shows the locations of the events and stations of those included in the 200 selected for the suite out of the larger original group of seismic events.

The 200 three-component recordings represented 36 earthquake events and 68 seismic stations. In order to ensure that the resultant suite of ground motions was representative of the Texas seismic hazard, the response spectra of the selected recordings were compared to target response spectra based on USGS 1-year hazard maps (Khosravikia et al., 2018). The selected motions are shown in red in Figure 3.5, out of the larger collection of 556 possible motions. Those selected had magnitudes of 4.0-5.8, hypocentral distances of 5-420 km, and PGA values of 0.0025-0.595g. These characteristics were found to be representative of the seismic hazard for Texas and, therefore, were utilized in the development of the fragility curves in the current study.

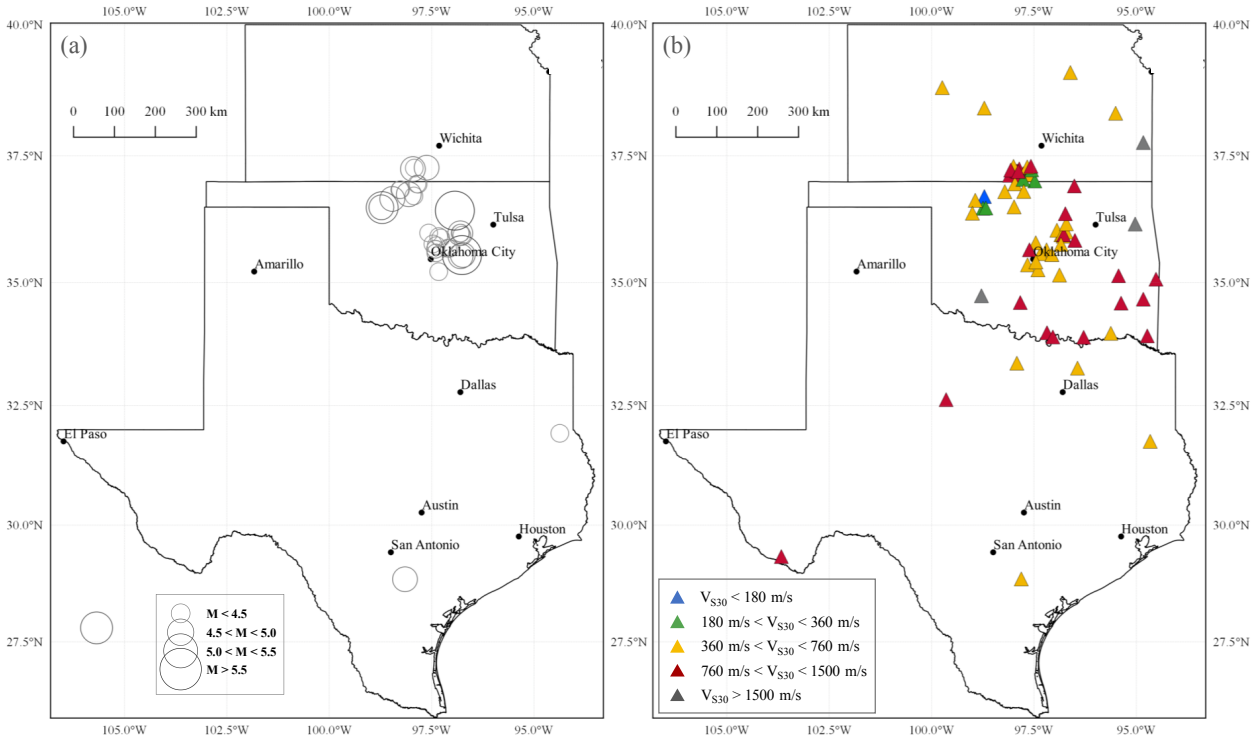

Figure 3.4: (a) Locations and Magnitudes of earthquake events selected for previous study, (b) Locations of seismic recording selected for previous study. (Khosravikia et al., 2018)

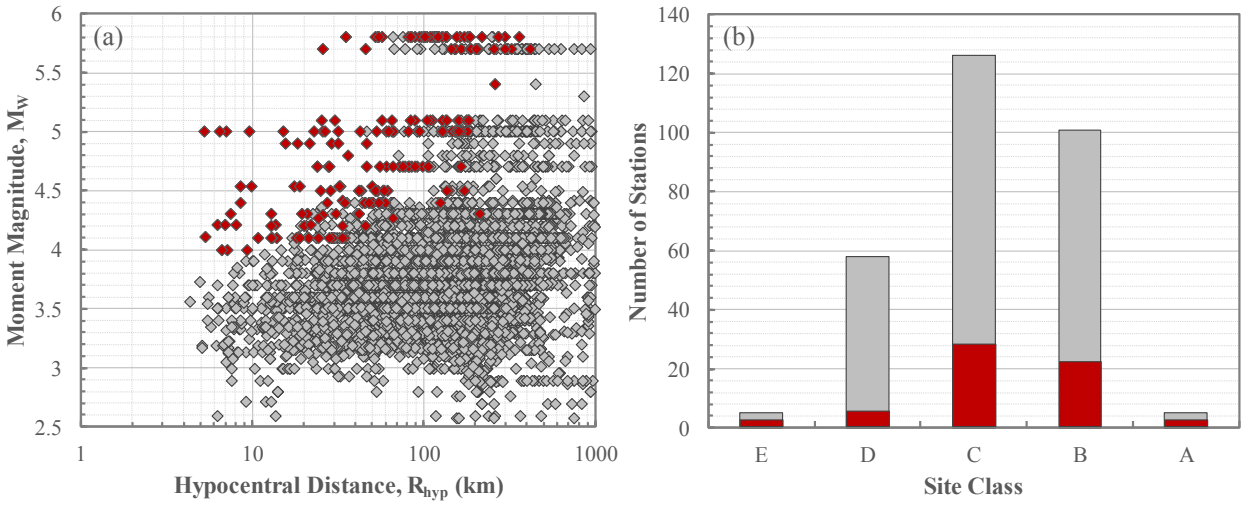

Figure 3.5: Ground motion database utilized in this study: a) Moment Magnitude (M_W) – Hypocentral Distance (R_{hyp}) distribution, and b) number of stations per NEHRP site classification; The selected ground motions for use in this project are shown in red. (Khosravikia et al., 2018)

In the creation of fragility curves, only the two horizontal components were considering for selection from the 200 recordings in the suite. For ground motion sets that were sampled based on specific ground motion characteristics, the horizontal direction with the maximum PGA value was selected to be used to develop the fragility curves for the current study. However, for ground motion sets that were randomly sampled from the suite of 200, the horizontal direction was randomly selected.

By first utilizing New Madrid ground motions, the resultant fragility curves could be compared to those developed in the previous Reneckis and LaFave (2009) study. However, because the ultimate objective of this study was to understand the behavior of the veneers under the types of ground motions found in Texas, Oklahoma, and Kansas, it was necessary to create fragility curves based solely on motions located in that region. To better determine the impact of ground motion characteristics on the fragility of the veneer wall, samples of twenty were chosen

from the Texas, Oklahoma, and Kansas recordings, herein referred to as the Texas suite. Different sets of ground motions were selected from the Texas suite based on the characteristics listed in Table 3.2. For example, four different sets of 20 ground motions each, were randomly selected from the suite to evaluate how the veneer fragility was affected by different random samplings. Ground motion sets were also selected from those motions from the largest magnitude events, those with the larges recorded PGA, and those recordings closest to the earthquake hypocenter. A list of the ground motions used in each set are given in Appendix A, which displays the characteristics of the ground motion files for each of the sample sets.

Table 3.2: Ground motion characteristics for comparative sampling.

Ground Motion Suite	Ground Motion Selection Characteristic
New Madrid	All
Texas	Random 1
	Random 2
	Random 3
	Random 4
	Max. Magnitude
	Max. PGA
	Min. Hypocentral Distance

3.3.1 GROUND MOTION CHARACTERISTICS

To better understand the characteristics within each of the samples used to create the fragility curves, which will be presented in Figure 3.16, box and whisker plots were developed for key ground motion parameters, in Figure 3.6, including event magnitude, hypocentral depth, recorded PGA, average shear wave velocity of the top 30 meters of soil (V_{s30}) (Zalachoris et al., 2017b), and hypocentral distance. The characteristics and distribution of parameters from the

recordings in each set were used to then evaluate potential correlation between certain ground motion characteristics and the resulting fragility curves.

The range of PGAs for the max PGA sample set is 0.5947g to 0.0604g, shown in Table A.6 of Appendix 1. This range is so large because of the nature of the Texas ground motion suite. There were only 8 files that had PGAs of at least 0.1g included in the suite. Therefore, in order to sample 20 ground motions, smaller values had to be included in the set. This range of PGA values was found to be consistent with the seismic hazard of the region, based on assessments by USGS (2016a). (Khosravikia et al., 2018) There were 13 unique seismic events that were included in this particular sample set from the Texas suite.

In addition, a sample set of 20 ground motion files contained those recordings with the smallest hypocentral distances, out of all the files within the suite. The range of distances in the sample were 5.2km to 13.9km, as shown in Table A.7 in Appendix A, and included motions from 9 unique seismic events. Comparing Table A.6 and A.7 also indicates that over half of the ground motions with the smallest hypocentral distance were also included in the maximum PGA sample set. The distribution of these characteristics is provided for the Texas sets in Figure 3.6, but were unable to be determined for the New Madrid suite due to the synthetic ground motions being developed to fit target spectra for 10% and 2% exceedance of a 50-year events.

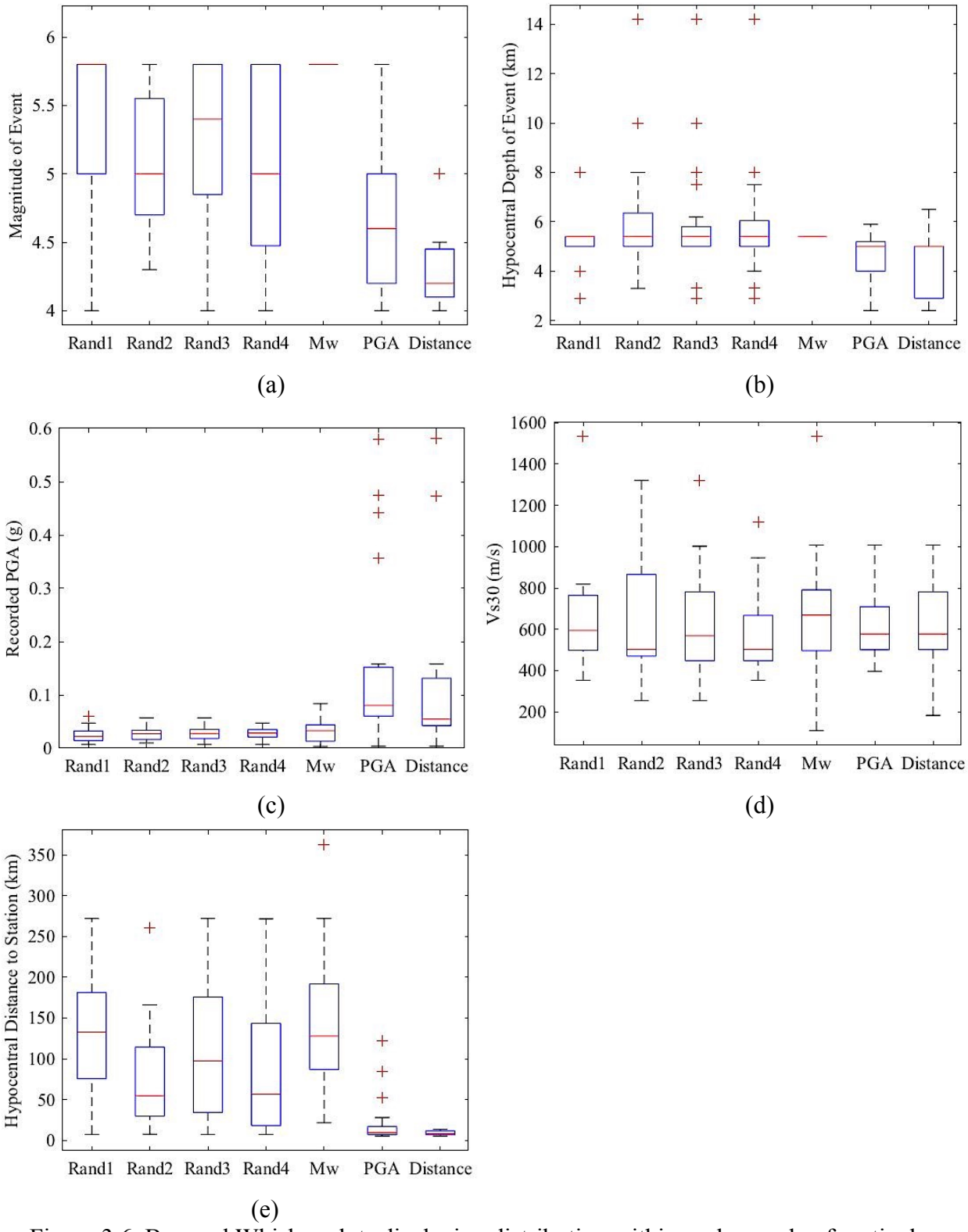

Figure 3.6. Box and Whisker plots displaying distribution within each sample of particular ground motion characteristics: (a) Magnitude of Event, (b) Hypocentral Depth, (c) Recorded PGA, (d) Vs_{30}[29], and (e) Hypocentral Distance to Station.

The mean depths of each set, shown in Figure 3.6(b), were all in the range of 5 to 6km. The relatively similar hypocentral depths across all samples indicated that this was characteristic of these types of induced seismic events and did not strongly influence the relative fragility of the veneer model. In addition, the distribution of mean recorded Vs_{30} is in the range of 500-700 m/s for all sample sets, as shown in Figure 3.6(d). As with recorded depth, this was determined to be a characteristic of the region over which ground motions were recorded and did not show an impact on the fragility of the curves created from each set of ground motions.

The PGA distribution in Figure 3.6(c) shows that in order to subject the veneer models to PGAs ranging from 0.1g to 2.2g, to develop fragility curves, a portion of the original ground motion files had to be scaled by large scale factors. No other adjustments were made to other ground motion characteristics when the files were scaled. Additional research should be done to assess the appropriateness of the methodology of scaling the original motions when larger PGA values are necessary. The process of scaling the original motions may lead to other aspects of the time histories to be inaccurately represented, such as the duration of strong shaking, leading to larger apparent levels of damage.

3.3.2 Ground Motion Spectral Responses

3.3.2.1 Texas Suite Spectral Response

Spectral acceleration plots were developed for each sample set tested, in order to determine a possible impact on the fragility of the curves developed using that specific set of ground motion recordings. Figure 3.7 shows all of the spectral acceleration responses, normalized with respect to PGA, for each of the seven ground motion sample sets. In order to better compare the spectral acceleration characteristics of each of the seven sets, the average

spectral acceleration response from each set of twenty motions found in Figure 3.7 is also shown in Figure 3.8.

The plots in Figure 3.7(a-d) display the responses of the four random samples. Comparing all four plot averages shows that the peak spectral acceleration occurs in the range of 0.1-0.15 seconds. In addition, the maximum spectral accelerations across these four plots are, on average, 2.7 to 3 times the PGA of each recording. The average maximum magnitude spectrum, in Figure 3.7(e), has a peak response of almost 3 times that of PGAs, occurring at a period of 0.14 seconds, within the range of the random sample peaks. The average spectrum for the maximum PGA set, in Figure 3.7(f), does not have a peak value at a discrete point, but occurs over a period range of 0.07-0.14 seconds, with a maximum of only approximately 2.5 times the PGA values. The minimum hypocentral distance set, Figure 3.7(g), also has a peak of approximately 2.5 times PGAs, but only occurs at a lower period of 0.07 seconds.

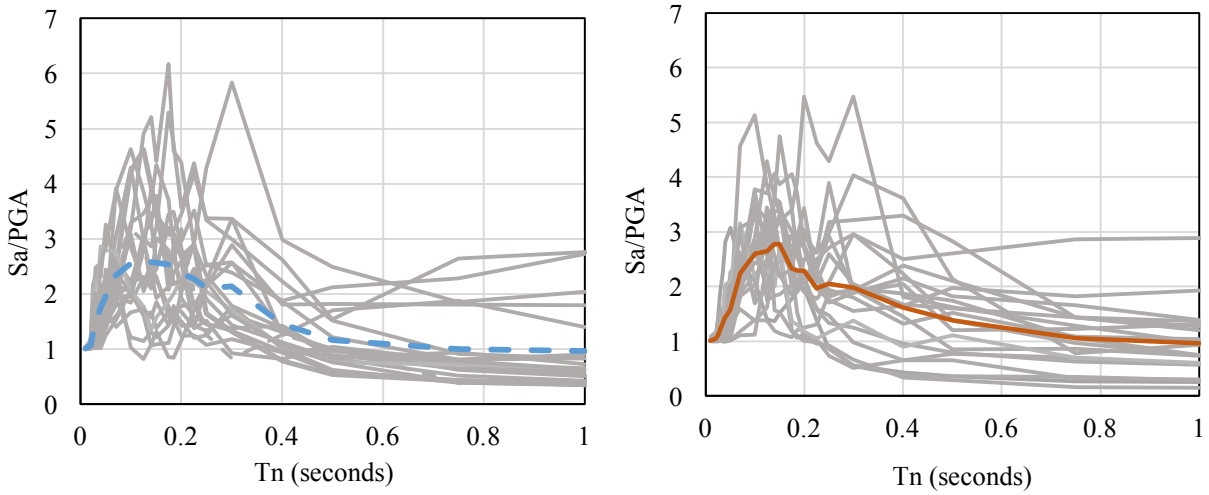

(a) (b)

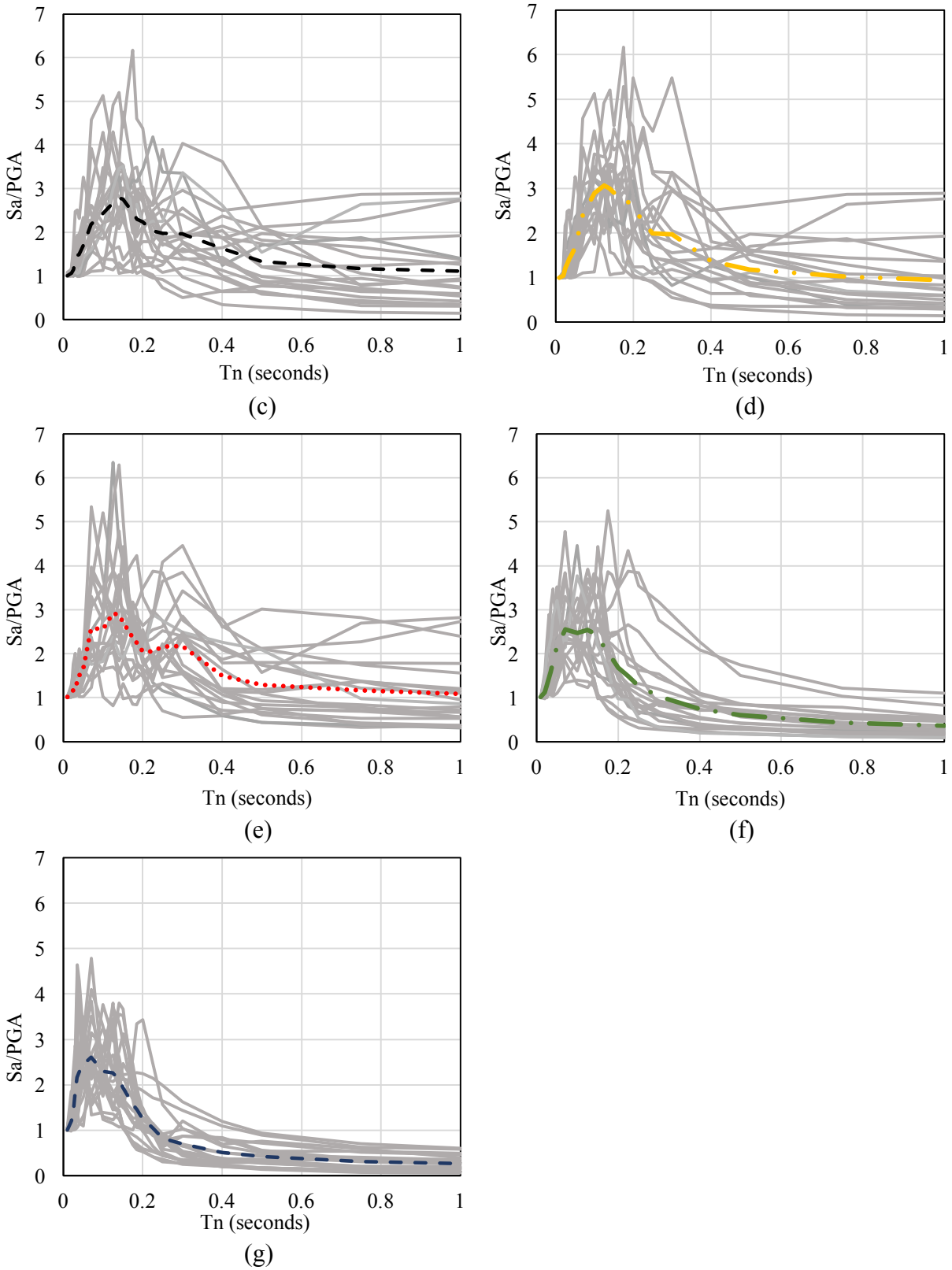

Figure 3.7: Spectral Acceleration plots for ground motion sample groups: (a) Random 1, (b) Random 2, (c) Random 3, (d) Random 4, (e) Maximum Magnitude, (f) Maximum PGA, and (g) Minimum Hypocentral Distance.

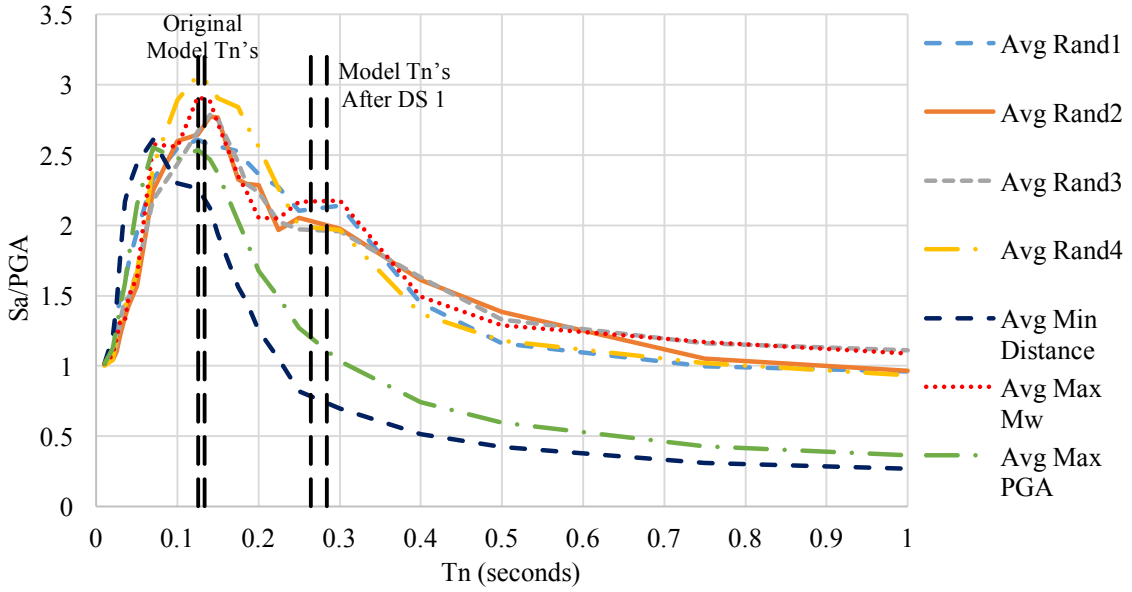

Figure 3.8. Average Spectral Acceleration for each sample set of ground motion files.

As shown in Figure 3.8, the four random samples and maximum magnitude sample all have a similar spectral shape. The maximum average acceleration values are within the range of 2.5-3.1 times the PGA, for periods of approximately 0.1-0.18 seconds. In addition, all five of these sample sets have a second portion of the spectrum that display a relatively constant acceleration within the 0.225-0.3 second period range. The maximum accelerations in this region are also clustered together at 2.0-2.2 times the PGAs of the recordings.

The maximum PGA average spectrum has a peak acceleration at lower period values of 0.07-0.125 seconds, and a lower peak spectral acceleration of 2.5 times recorded PGAs. In the lower period range, around 0.07 seconds, the average maximum PGA spectral response is actually greater than all other samples, but decreases rapidly above the 0.1 second period range. This observation indicates that the maximum PGA and minimum hypocentral distance sets display the largest spectral acceleration amplification at lower natural periods, compared to the random samples or the maximum magnitude sample. The period range of peak acceleration is a result of the characteristics of the ground motions that were utilized in a particular sample set.

For example, the random and maximum magnitude spectra have significantly more amplification at larger periods because those samples included larger magnitude events, shown in Figures A.1-A.5, compared to other sets. Larger magnitude events are typically known to have longer period content because larger magnitude indicates more energy released, which is required to produce the longer period seismic waves. In contrast, smaller magnitude events, such as those included in the max PGA and minimum distance samples, typically have a higher content of higher frequency shaking, leading to larger acceleration amplifications in smaller period ranges.

The maximum PGA and minimum distance samples also show a quick decline in spectral acceleration compared to the rest of the Texas sample sets, and beyond periods of 0.2 seconds, spectral acceleration is approximately only half the other five sets. The random samples and maximum magnitude samples showed larger overall spectral acceleration amplification values.

The OpenSEES wall model natural period values in Table 2.5, from Section 2.4, were plotted with the average spectral acceleration plots for each sample in Figure 3.8. Analysis of Figure 3.8 shows that both of the original natural periods fall within the maximum spectral response regions for all samples. However, the periods are at the peaks of the random and maximum magnitude samples. In contrast, the natural periods after the first tie failed, reaching DS1, are located in a region where the average spectra response for both max PGA and minimum distance have already significantly decreased. In addition, the maximum PGA and minimum hypocentral distance sample spectra show a rapid downward slope as the period increases beyond that of DS1. The difference in the downward slope as the walls were damaged and periods elongated affects the resulting level of damage in DS2 when comparing the seven sample sets, as will be discussed later in Section 3.4.1.1 with the development of the Texas fragility curves.

3.3.2.2 NEW MADRID SPECTRAL RESPONSE

The spectral acceleration plot for the New Madrid suite of 20 motions is displayed in Figure 3.9, including the average of the suite. The range of constant acceleration is within periods of 0.1-0.15 seconds, with a maximum acceleration ratio of 3, which is within the range of maximum accelerations of the Texas ground motion sets from Figure 3.8.

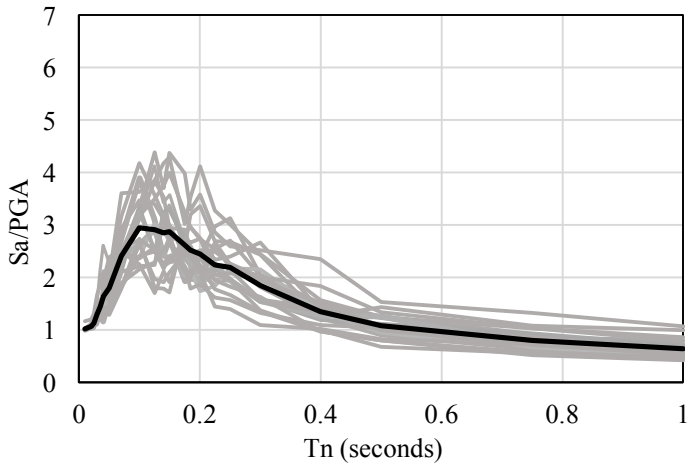

Figure 3.9. Spectral Acceleration plot of New Madrid ground motion suite, including average spectrum.

Comparing the spectrum Figure 3.9 to those in Figure 3.7, indicates the likely cause for less variability that will be shown in the New Madrid fragility curves, because the New Madrid response spectra are much more tightly clustered and uniform compared to those of the Texas samples. Increased spread of ground motion spectral response leads to more uncertainty when predicting the veneer wall response, which will be evident in the fragility curves. The average spectrum of the New Madrid suite is included with the averages of the seven sample sets from the Texas ground motion suite in Figure 3.10.

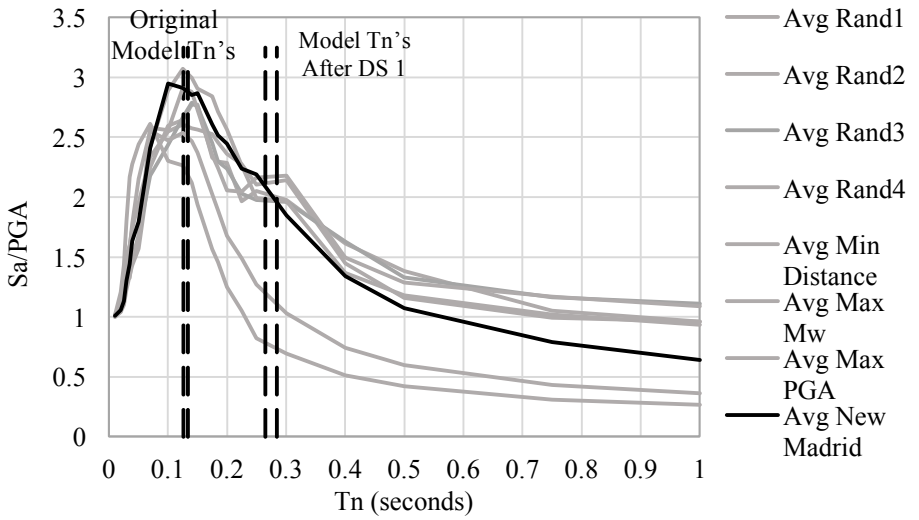

Figure 3.10. Average Spectral Acceleration plots for Texas and New Madrid sample sets.

The shape of the New Madrid spectrum, in Figure 3.10, closely follows that of the random and maximum magnitude sample set, including the period range of maximum acceleration. However, the New Madrid spectral acceleration plot does not have a second, lower region of constant acceleration around periods of 0.225-0.3 seconds, which was present in the majority of the Texas sample sets. The rate of decline of spectral acceleration at increasing periods of the New Madrid response is similar to that of the random and maximum magnitude sets as well.

3.4 Fragility Curve Comparisons

3.4.1 Effects of Ground Motion Characteristics and Tie Types

The fragility curves created from the New Madrid suite are shown in Figure 3.11. Fragility curves were created for two different tie and installation combinations, 28 gauge ties with minimum installation eccentricity, referred to herein as 28ga(min) (Wall #1 in Table 3.3), and 22 gauge ties with the maximum code allowable installation eccentricity, referred to herein as 22ga(ecc) (Wall #2 in Table 3.3). For purposes of comparison, the fragility curves generated

by the OpenSEES models used in this study were compared to the fragility curves developed by Reneckis and LaFave (2009) using the same New Madrid ground motions suite. Figure 3.11(a) shows that for Wall #1, both Damage State 1 and 2 (DS1 and DS2, respectively) are more vulnerable with the OpenSEES model compared to the FE model created in the previous study by Reneckis and LaFave (2009). However, for a wall with 22ga(ecc) ties, in Figure 3.11(b), the new OpenSEES model is less fragile than the previous model for Damage State 1. The OpenSEES model for Damage State 2 for PGA less than 0.7g, is more fragile than that of the previous study, but for larger PGAs over 0.7g the current OpenSEES model becomes less fragile.

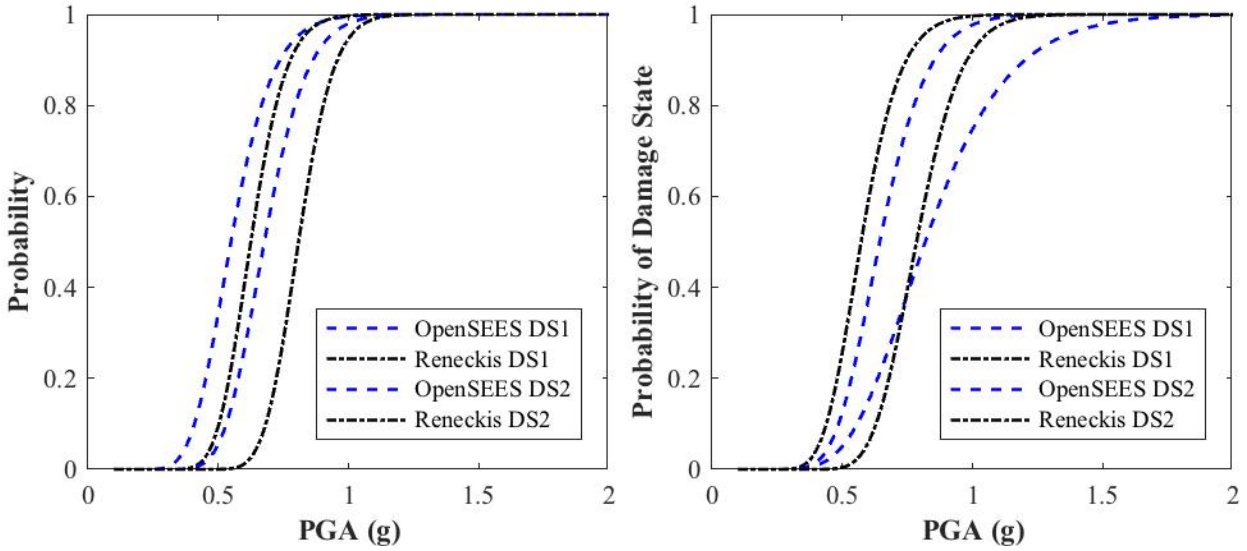

Figure 3.11. Comparison of OpenSEES model and previous study fragility curves subjected to New Madrid suite ground motions, for both tie types and damage states: (a) 28ga(min) (Wall #1) and (b) 22ga(ecc) (Wall #2).

The more significant increase in fragility for the 28ga(min) OpenSEES models is a result of the alterations made to the tie backbone behavior discussed in the previous Section 2.2. In order to more closely represent the tie subassembly behavior, the 28ga(min) tie maximum deformation limit, indicating tie failure, decreased more than that of the 22ga(ecc) tie backbone, compared to the previous failure limits in the Reneckis and LaFave (2009) study. Both damage states are

based on these maximum tie deformation values, therefore, a more significant backbone change results in the increased fragility in Figure 3.11(a). In contrast, there was little difference between the experimental subassembly 22ga(ecc) backbone and the one used to create the Reneckis fragility curves in Figure 3.11(b). Therefore, the development of the 22ga(ecc) backbone for the OpenSEES model, which was based on the subassembly cyclic behavior, did not have as significant an impact on the resultant fragility curves. However, the small decrease in fragility could be attributed to the slight increase in the lateral resistance spring stiffness, previously discussed in Section 2.3.1.3. The median PGA values of the New Madrid fragility curves, developed with OpenSEES, are shown in Table 3.3.

Table 3.3: Median PGA and lognormal standard deviation parameters for fragility curves of models subjected to New Madrid suite. (Wen and Wu, 2001)

Wall Model	Damage State 1		Damage State 2	
	Median PGA (g)	Beta (β)	Median PGA (g)	Beta (β)
Wall 1	0.549	0.23	0.677	0.19
Wall 2	0.644	0.22	0.819	0.3

3.4.1.1 TEXAS SUITE FRAGILITY CURVES

In order to determine the impact of which ground motions were sampled, on the resultant fragility curves, first a total of four random samples were taken to create four different fragility curves. Figure 3.12 shows the resultant fragility curves for the four random samples for both 28ga(min) (Wall #1 in Table 3.4) and 22ga(ecc) (Wall #2 in Table 3.4) ties. An average across the four samples was calculated as well, to be used in comparison to curves created specifically based on ground motion characteristics, which will be shown later in this section. The median PGA and beta values of the four random fragility curves is found in Table 3.4.

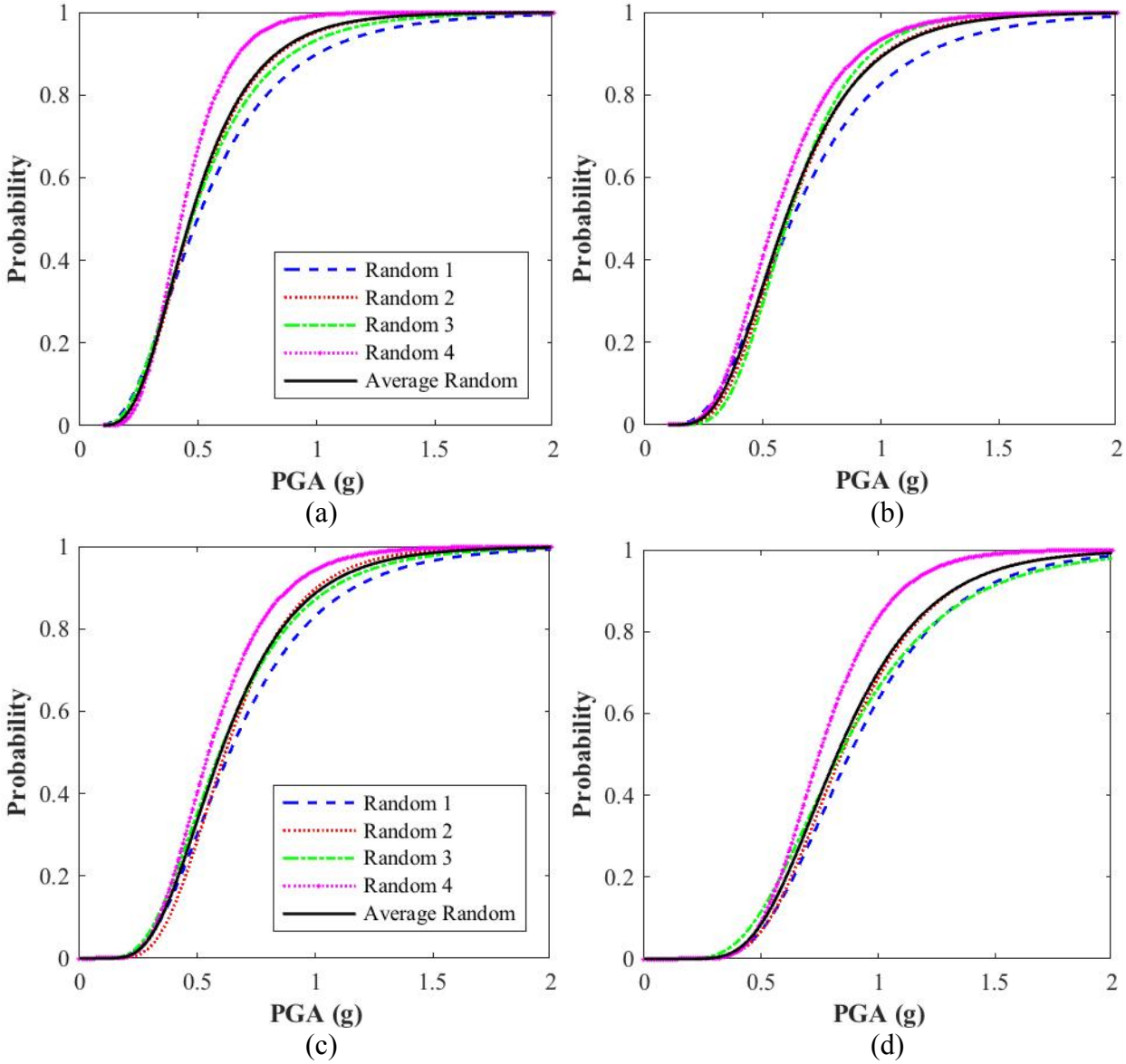

Figure 3.12. Fragility curves from models subjected to four random sets of Texas ground motion files: (a) 28ga(min) Ties (Wall #1) Damage State 1, (b) 28ga(min) Ties (Wall #1) DS 2, (c) 22ga(ecc) (Wall #2) Damage State 1, and (d) 22ga(ecc) (Wall #2) Damage State 2.

Table 3.4: Median PGA and lognormal standard deviations of fragility curves from Texas random samplings.

Wall Model	Sample Number	Damage State 1		Damage State 2	
		Median PGA (g)	Beta (β)	Median PGA (g)	Beta (β)
Wall 1	1	0.497	0.55	0.625	0.5
	2	0.472	0.45	0.607	0.4
	3	0.470	0.5	0.602	0.36
	4	0.427	0.35	0.549	0.4
	Average	0.467	-	0.597	-
Wall 2	1	0.638	0.47	0.878	0.38
	2	0.619	0.38	0.844	0.35
	3	0.595	0.46	0.835	0.43
	4	0.549	0.38	0.748	0.3
	Average	0.600	-	0.826	-

The sampling for the motions with the maximum magnitude all had a magnitude of 5.8 because they were all recorded for the same event in Pawnee, OK. The fragility curves created from this sampling are shown in Figure 3.13. The fragility curves developed from a sample of the ground motion files with the twenty largest maximum PGAs are displayed in Figure 3.14, while those produced using the closest hypocentral distance recordings are shown in Figure 3.15. After the creation of the seven different fragility curves for both 28ga(min) and 22ga(ecc) tie type walls, Wall #1 and Wall #2, respectively, comparison of the Average Random, Maximum Magnitude, Maximum PGA, and Minimum Hypocentral Distance curves indicated the relative fragility of each wall based on the type of ground motion sample chosen. Figure 3.16 displays the plot of these curves together to allow for ease of comparison.

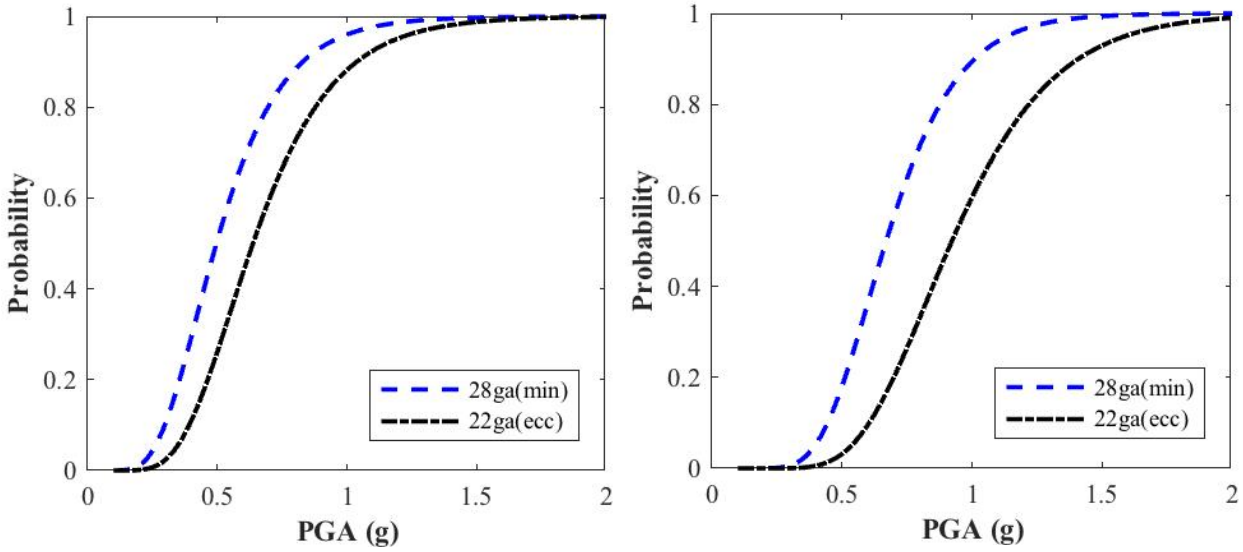

(a) (b)

Figure 3.13. Fragility curves from selection of Texas ground motion files with largest magnitude events: (a) Damage State 1 and (b) Damage State 2.

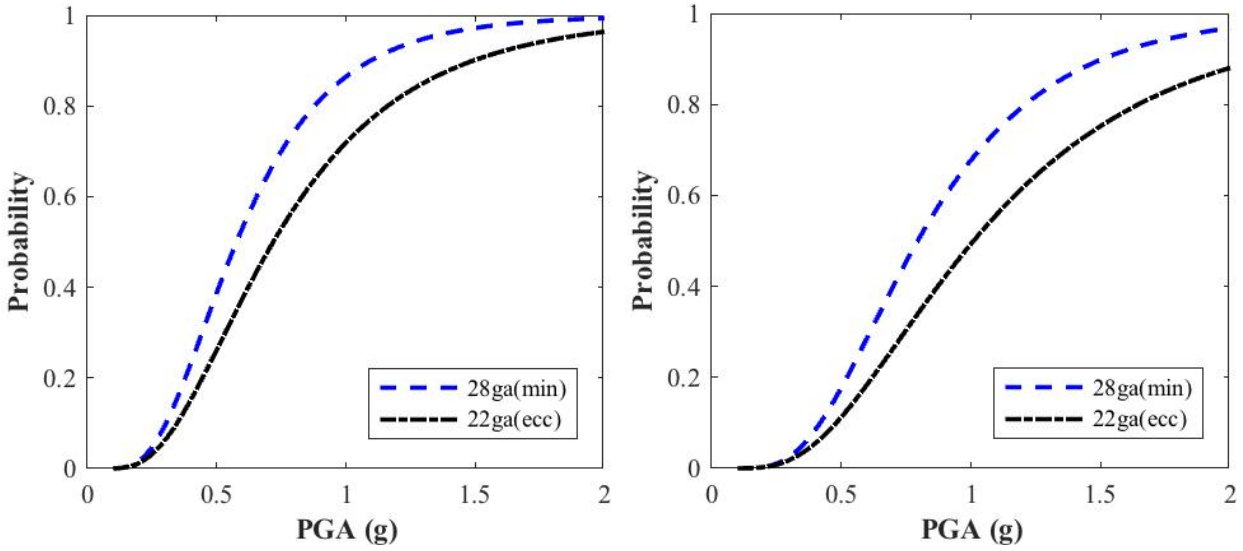

(a) (b)

Figure 3.14. Fragility curves from selection of Texas ground motion files with largest maximum PGA recordings: (a) Damage State 1 and (b) Damage State 2.

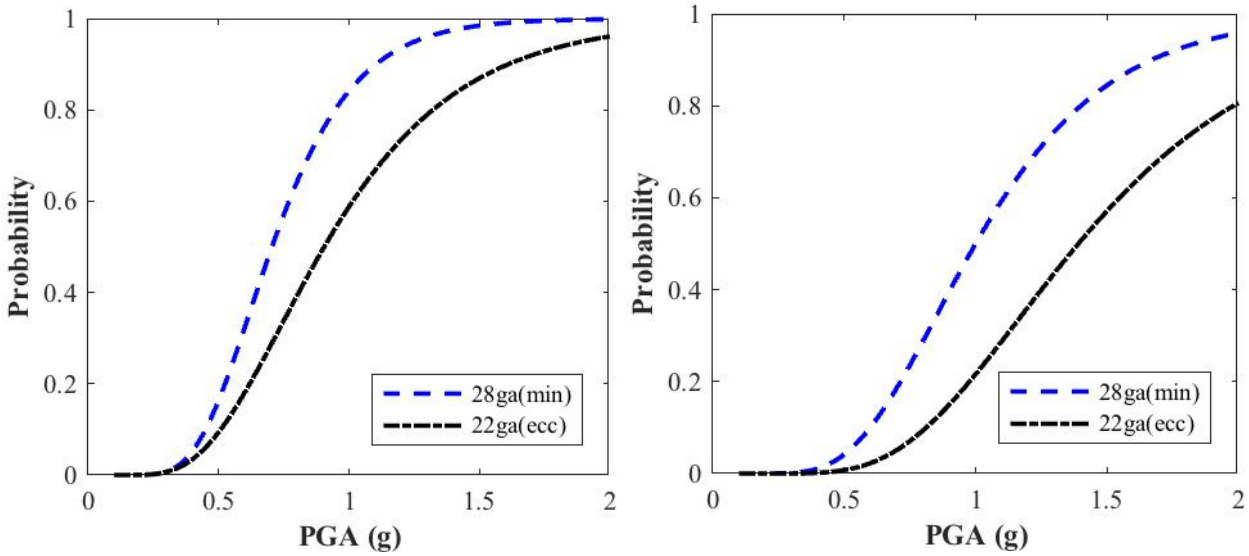

(a) (b)

Figure 3.15. Fragility curves from selection of Texas ground motion files with smallest hypocentral distance recordings: (a) Damage State 1 and (b) Damage State 2.

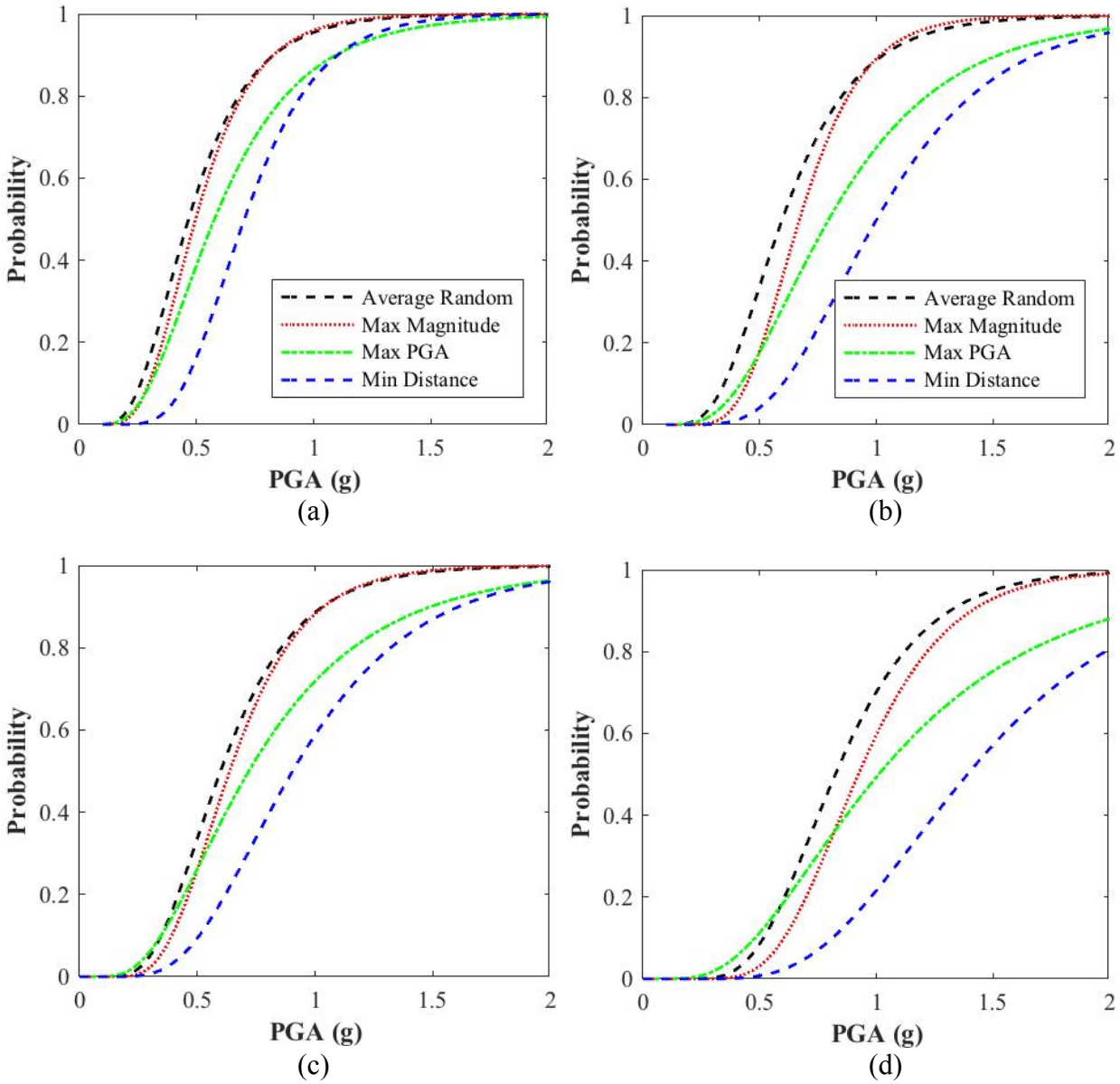

Figure 3.16. Comparison of fragility curves based on selected sample characteristics: (a) 28ga(min) Damage State 1 (Wall 1), (b) 28ga(min) Damage State 2 (Wall 1), (c) 22ga(ecc) Damage State 1 (Wall 2), and (d) 22ga(ecc) Damage State 2 (Wall 2).

As observed in Figure 3.16, on average, the fragility curves developed using a random sample of twenty ground motions from the suite were shown to be the most fragile for walls of both tie types. In contrast, those curves created using ground motions out of the suite with the shortest hypocentral distances were observed as the least fragile. Comparing Figure 3.16(a) and (c) displays the relative fragility of the two tie types tested. The range of median PGAs in Figure

3.16(a) is 0.35-0.75g, while in Figure 3.16(c) the range is shown as 0.55-0.95g. In addition, the Damage State 2 range of medians for 28ga(min) is 0.5-1.0g, in Figure 3.16(b), and that of the 22ga(ecc) ties is 0.75-1.4g. Table 3.5 below shows the values for the median PGAs and lognormal standard deviations for both damage states of the maximum magnitude, maximum PGA, and minimum distance sample sets.

Comparing Figure 3.16 to Figure 3.6(a) indicates that there is a correlation between the magnitude of the events and the relative fragility of the curve developed from those motions. As shown in Figure 3.16, the most fragile of the curves were those created with random and maximum magnitude sample selections. All of these samples have a mean magnitude greater than 5.0 in Figure 3.6(a). In addition, the mean magnitude of the sample for smallest hypocentral distances, the least fragile curve, is shown to be the lowest of all sample sets tested.

Based on the distribution of the mean PGA of each sample set in Figure 3.6(c), there does not appear to be a direct correlation between PGA values within a ground motion set and the relative fragility of the resultant brick veneer fragility curve. Figure 3.6(e) displays the variation in hypocentral distances of the recordings in each sample set. The more fragile curves, the random and maximum magnitude samples, were found to contain events with larger average recorded hypocentral distances. As shown in Figure 3.6(e), all five of those sample sets had average hypocentral distances greater than 50 km, while both the maximum PGA and minimum distance sets were only approximately 10 km. However, it should be noted that it is unlikely for earthquakes of low and moderate magnitude, such as those in Texas, to produce significant shaking intensities sufficient to cause damage at such large hypocentral distances (Zalachoris and Rathje, 2017a).

Observing the variation in accelerations in Figure 3.8, for each sample type at the original, undamaged, natural periods shows that there is a correlation between the most fragile fragility curves and those spectra with the larger accelerations at the designated periods. The random sample sets and the maximum magnitude spectra have not only the largest overall spectral acceleration amplifications, but also reach those maximum values within the critical period range of both the 28 and 22 gauge walls.

As expected, the 28-gauge walls were shown to be more fragile for both Damage State 1 and 2, for all Texas sample sets tested. The comparison indicates that, for both damage states, the use of code compliant anchors, rather than 28 gauge, allows for an increased level of protection against wall instability for all Texas sample sets.

Table 3.5: Median PGA and lognormal standard deviations of characteristic Texas samples.

Tie Type	Sample Type	Damage State 1		Damage State 2	
		Median PGA(g)	Beta (β)	Median PGA(g)	Beta (β)
28ga(min) (Wall #1)	Max M_w	0.497	0.4	0.670	0.32
	Max PGA	0.577	0.5	0.795	0.5
	Min Distance	0.705	0.35	1	0.4
22ga(ecc) (Wall #2)	Max M_w	0.638	0.38	0.923	0.33
	Max PGA	0.719	0.57	1.01	0.58
	Min Distance	0.905	0.45	1.39	0.42

In addition, to understand the difference in veneer behavior when subjected to New Madrid compared to those experienced in Texas, Kansas, and Oklahoma, Figure 3.17 shows the New Madrid fragility curves along with those already presented in Figure 3.16. In all four types of fragility curves in Figure 3.17, the New Madrid curves are observed to have the least uncertainty compared to that of any Texas samples. The New Madrid ground motion suite consisted of 20 synthetic time histories, which were specifically created to match the 10% and

2% in 50 year target response spectra in and around Memphis, TN. However, the Texas suite contained a larger number of real event time histories that were spread over the region of Texas, Oklahoma, and Kansas. Therefore, it should be expected that the Texas fragility curves show a larger amount of variability of when a damage state is reached.

The median PGA for both damage states of the 22ga(ecc) ties (Wall 2) fall within the range of those for the corresponding random sample values under Texas ground motions, found in Table 3.4. There was a small increase in median PGA of the New Madrid fragility curves compared to those of the random Texas samples, in Tables 3.3 and 3.4, respectively. Even though the spectral shape of the New Madrid suite shows similar behavior to that of the random samples from the Texas suite, the differences in other ground motion characteristics, between the two suites, is likely the cause for the difference in fragility.

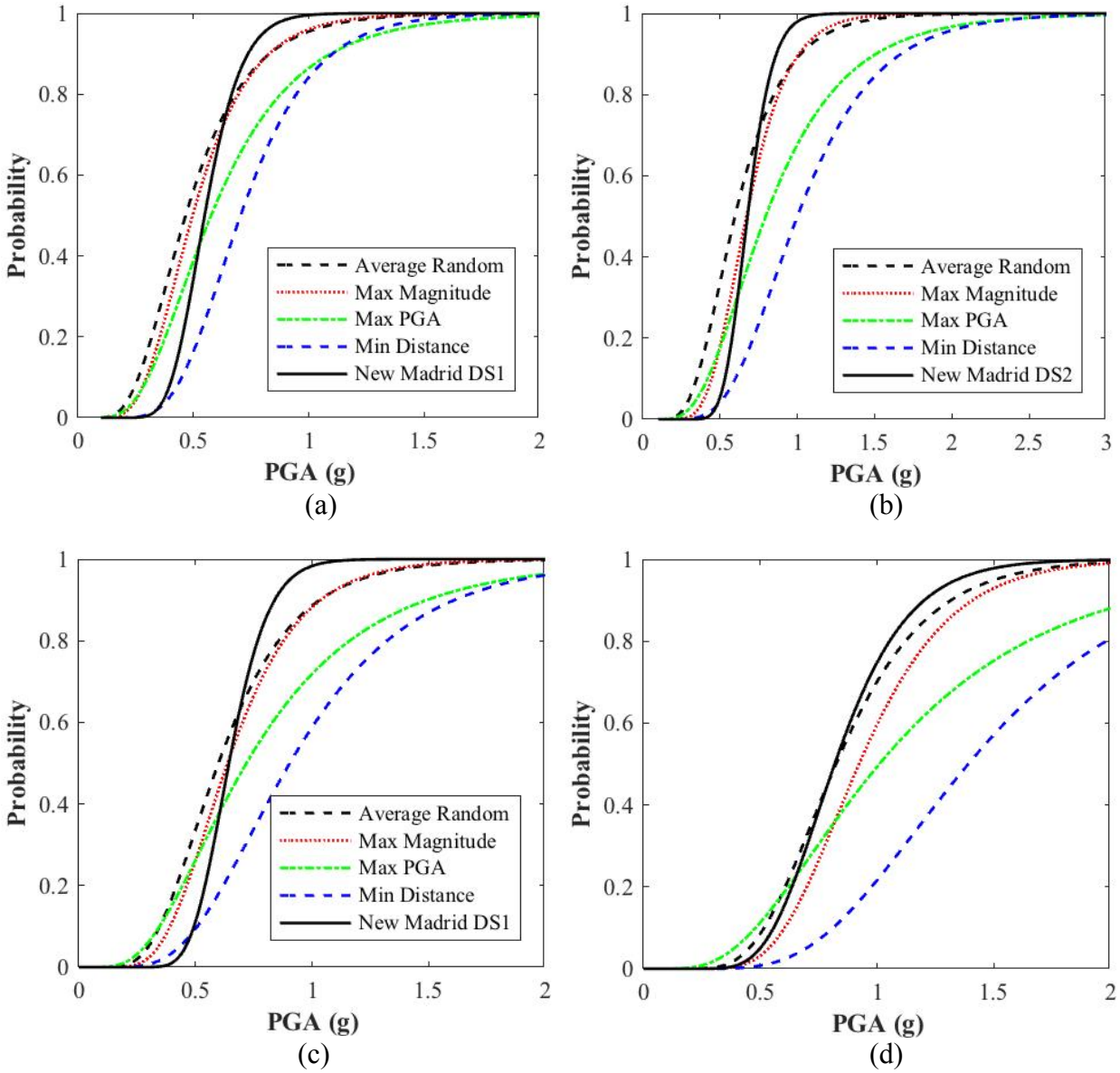

Figure 3.17. Comparison of Texas sample groups with corresponding New Madrid fragility curve for: (a) 28ga(min) Damage State 1 (Wall 1), (b) 28ga(min) Damage State 2 (Wall 1), (c) 22ga(ecc) Damage State 1 (Wall 2), and (d) 22ga(ecc) Damage State 2 (Wall 2).

3.4.2 Effects of Tie Spacing on Fragility Curves

OpenSEES computational models were utilized to better understand the influence of tie installation factors (i.e. tie spacing used) on the relative fragilities of the brick veneer walls. As discussed in Section 1.2.1, code complaint vertical tie spacing can be up to 24 inches, which was

also the original vertical spacing of the OpenSEES computational model. The original 28ga(min) (Wall #1) strip wall model was modified to have two different, larger tie spacing layouts. The intent of these new models was to explore two configurations that had larger than code compliant tie spacing. The vertical locations of the ties in each of these two models, measured from the base of the brick veneer wall, is found in Table 3.6. In addition, schematics of the non code compliant models are found in Figure 3.18.

Table 3.6: Vertical locations of veneer ties in modified non-code compliant walls.

Wall	New 28ga(min) Tie Vertical Locations (inches)
#3	32, 80
#4	8, 56, 104

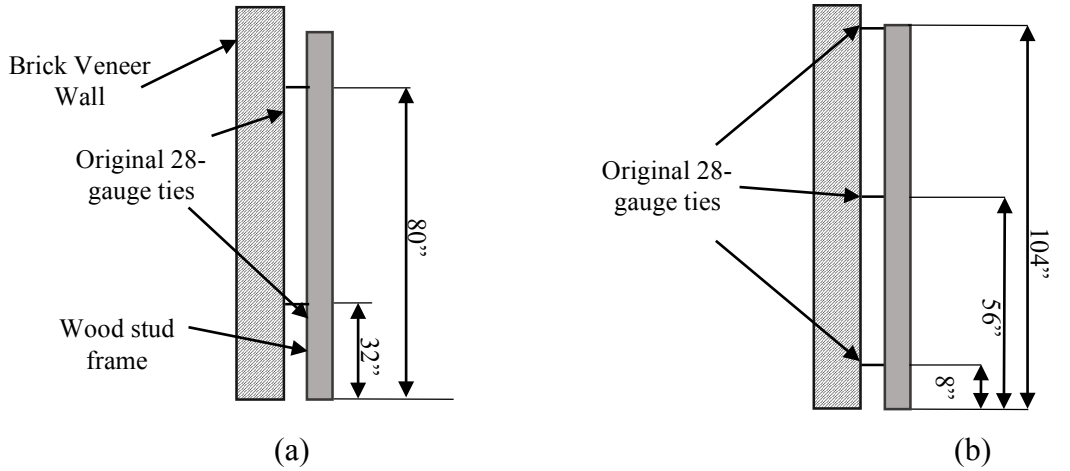

Figure 3.18. Schematics tie layout for larger than code compliant spacing: (a) Wall #3, and (b) Wall #4.

Each of the modified walls was subjected to one set of 20 ground motions from the Texas suite. The set selected was Random 2 because it was determined that a random sample would better capture the overall fragility behavior across the region where the seismic events were recorded. In addition, the individual Random 2 sample set more closely aligned with the overall average of all the random samples that were evaluated, as shown in Figure 3.12. The fragility

curves for both Wall #3 and Wall #4 are found in Figure 3.19. In this sensitivity study, the original fragility curve, using the same random sample set of Texas ground motions, for a veneer with 28ga(min) ties spaced at 24 inches (Wall #1) was compared to both modified walls, Wall #3 and #4, shown in both Figure 3.19 and Table 3.7.

Damage states 1 and 2 are the same as those used in the development of the regular wall model fragility curves. No wall specimens were experimentally tested using the larger tie spacing; therefore, no experimental evidence is available to determine the modes of failure, in the modified walls, that correlate with the first and second tie failures. It is unknown if failure of the top tie produces only cracking since there are only a total of two ties present in the non-retrofitted modified walls. Therefore, the fragility curves developed for the modified walls should be used as representative of PGAs at which ties will fail, as well as the relative fragility achieved with added retrofits, rather than damage states explicitly for repairable damage and collapse.

Figure 3.19(a) shows that Wall #3, with only two ties vertically at 32 and 80 inches, is more fragile than Wall #4, when subjected to ground motion. This should be expected because Wall #3 has not only a fewer number of overall ties, compared to Wall #4, but also does not have a tie at the top of the veneer wall. This is important to note because based on previously observed experimental data, and the definition of the damage states for this study, the top of the veneer should be expected to be where the wall is weakest and damage initiates. This comparison indicates that the spacing of the wall ties, as well as the inclusion of a tie at the top of the veneer wall, are important factors when trying to ensure adequate wall response to seismic activity.

Table 3.7 indicates the percent decrease in median PGA of Walls #3 and #4 compared to that of the original code compliant spaced 28ga(min) wall (Wall #1), in order to evaluate the

change in fragility for models with larger tie spacing. Wall #3, which had no top tie, was shown to be much more fragile than Wall #4, even though the spacing between the ties was 48 inches for both models. In addition, Table 3.7 indicates that the reduction in median PGA for Damage State 2 was less impacted by the larger tie spacing than for Damage State 1.

Wall #4 in Figure 3.19(a) did not vary from the original wall as significantly as Wall #3. This could be attributed to Wall #4 having more ties, including a top tie, which more closely resembles the full wall tie layout of the original wall compared to Wall #3. The fragility curves for Wall #1 and #4, in Figure 3.19, are much more tightly clustered than those for Wall #1 and #3. This indicates that the presence of a top veneer tie greatly influences the wall response. Even when ties within the center region of the wall are missing or not engaged, as simulated with both modified walls, Wall #4 with ties vertically at 32, 80, and 104 inches was able to closely imitate the original full tie wall behavior.

Table 3.7: Median PGAs of modified non-code compliant spacing wall models.

	DS1		DS2	
	Median PGA (g)	Beta (β)	Median PGA (g)	Beta (β)
Wall #3	0.082	0.7	0.135	0.85
Wall #4	0.368	0.45	0.577	0.44
Wall #1	0.472	0.45	0.607	0.4
Percent Decrease Wall #1 to Wall #3	82.6%	-	77.8%	-
Percent Decrease Wall #1 to Wall #4	22%	-	4.9%	-

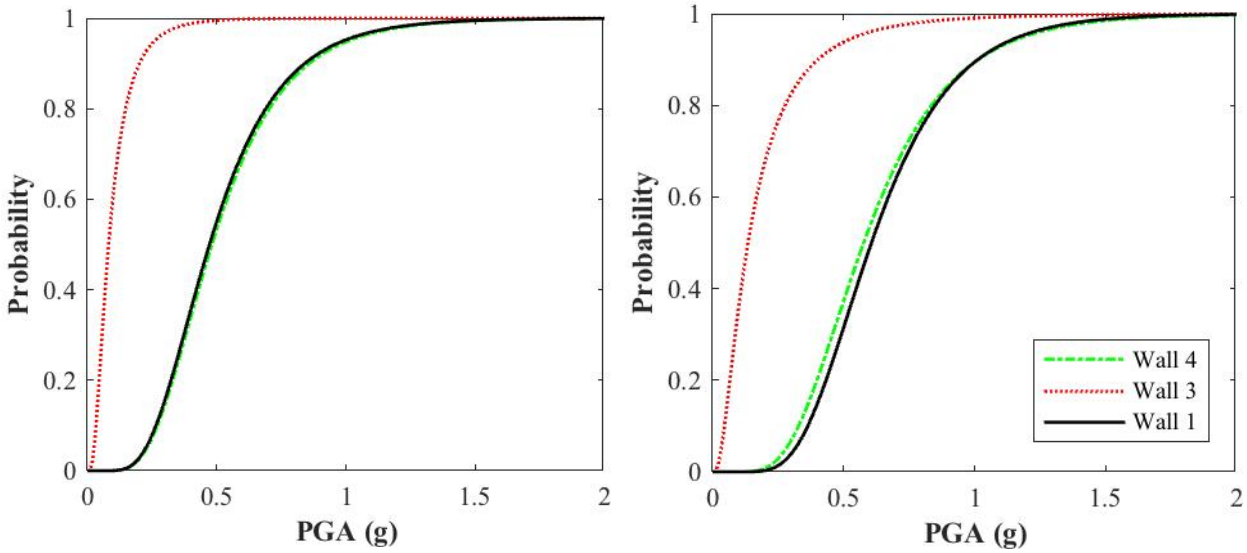

(a) (b)

Figure 3.19. Comparison of original 28ga(min) wall model (Wall #1) to two models with larger than code-compliant tie layout wall models: (a) DS 1 for Wall #3 & #4, and (b) DS 2 for Wall #3 & #4.

3.4.3 Effects of Retrofits on Fragility Curves

Part of the motivation behind the study was to also gain a better understanding of simple techniques to retrofit existing walls. Therefore, the two previously mentioned modified walls (Walls #3 and #4) were also evaluated for behavior when a 22ga(ecc) tie was present at the top of the veneer wall. Table 3.8 shows the location of the original, non-code compliant ties and the added ties acting as retrofits for both walls. Figure 3.20 displays schematics of the tie layout for both modified walls, in the retrofitted versions. Wall #5 was based on Wall #3, but was retrofitted by the addition of a code compliant 22ga(ecc) tie at the top of the brick veneer wall, at 104 inches from the bottom. Wall #6 was based on Wall #4, which already included a 28 gauge at the top of the veneer, so this tie was replaced in OpenSEES for a 22-gauge tie (22ga(ecc)) at the same location, rather than the addition of a tie. This retrofitted model, Wall #6, showed the impact of only exchanging a non-code compliant, but commonly used, 28-gauge tie for a code compliant 22-gauge tie at the top of the wall only.

Table 3.8: Tie locations for retrofitted non-code compliant wall models.

Wall	New 28ga(min) Tie Vertical Locations (inches)	Location of Additional 22ga(ecc) Tie
#5	32, 80	104
#6	8, 56, 104	104

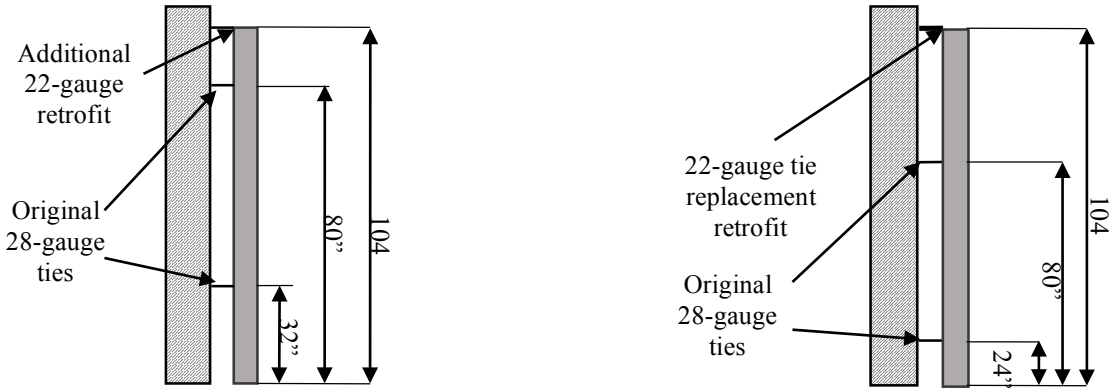

Figure 3.20. Schematic of retrofits of larger than code-compliant wall models: (a) Wall #5, and (b) Wall #6.

The change in median PGA for all four plots in Figure 3.21 can be found in Table 3.9, in order to better evaluate the actual reduction in fragility of the modified walls. The significantly larger percent increase in median PGA, indicating decreased fragility, for Wall #3 shows the effectiveness of having a top tie installed. Wall #4 already had a top tie before it was retrofitted, which is why there was less increase in median PGA compared to Wall #3 that had no top tie. This indicates that including a veneer tie at the top of the wall has a bigger impact on wall behavior than switching to a code compliant tie at the same location.

Table 3.9: Median PGAs of retrofitted larger than code-compliant tie spacing wall models.

	DS1		DS2	
	Median PGA (g)	Beta (β)	Median PGA (g)	Beta (β)
Wall #3	0.082	0.7	0.135	0.85
Wall #5	0.247	0.5	0.602	0.34
Percent Increase from Retrofit (Wall #3 to #5)	201%	-	346%	-
Wall #4	0.368	0.45	0.577	0.44
Wall #6	0.482	0.45	0.589	0.35
Percent Increase from Retrofit (Wall #4 to #6)	31%	-	2.1%	-

Figures 3.21(a) and (b) display the effectiveness of the addition of a code compliant tie to the top of the veneer wall. In both plots, the fragility of the wall is lowered, especially for Damage State 2. Wall #6 in Figure 3.21(a) and (b) shows the impact on fragility when a code compliant anchor is used at the top of the wall, which is predicted to be the point where damage initiates, rather than the original 28-gauge tie. The reduction in fragility is minor compared to that of retrofitting the wall with no top tie at all in Wall #3. This is to be expected because just the presence of a veneer tie, even 28-gauge, will already give the wall better performance since the top of the wall is where damage initiates.

In Figure 3.21(a) both Walls #3 and #4 are more fragile than the original veneer wall model, as was expected. However, the addition of the 22-gauge tie at the top of the wall reduces the fragility beyond that of the original wall, most significantly for Damage State 2, as shown in Table 3.7. When both Walls #3 and #4 were retrofitted, the top tie maximum allowable displacement was increased because it was a 22-gauge tie, based on the subassembly test data from Section 2.2.5. Therefore, for both retrofitted walls, DS1 and DS2 fragility curves were almost identical because the top two ties reached their respective maximum displacement limits

at the same PGA level. This explains why in Figure 3.21(a), the two retrofitted walls appear less fragile than the original veneer model that contained a full set of 28ga(min) ties. In addition, Figure 3.21(b) shows that for DS2, Wall #4 and Wall #6 are virtually the same, which can also be attributed to the change in failure behavior when the top tie is replaced with a 22-gauge tie. Comparing the median PGA values for Wall #5, in Table 3.9, to those of the original random sample number 2, in Table 3.7, also demonstrates that for DS 2, Walls #4, #5, and #6 were all able to achieve median PGA values close to the original full 28ga(min) model (Wall #1).

In addition, both Figure 3.21(a) and (b) show that, when retrofitted, the fragility curves for both walls become very similar. The significant decrease in fragility show in Figure 3.21(a) and (b) does indicate that for current walls that might have ties missing from the center, or even from the top of the veneer, retrofitting by the addition of a code compliant 22-gauge tie at the top of the wall does allow the wall response to move significantly closer back to the original code complaint 24-in spaced tie wall (Wall #1).

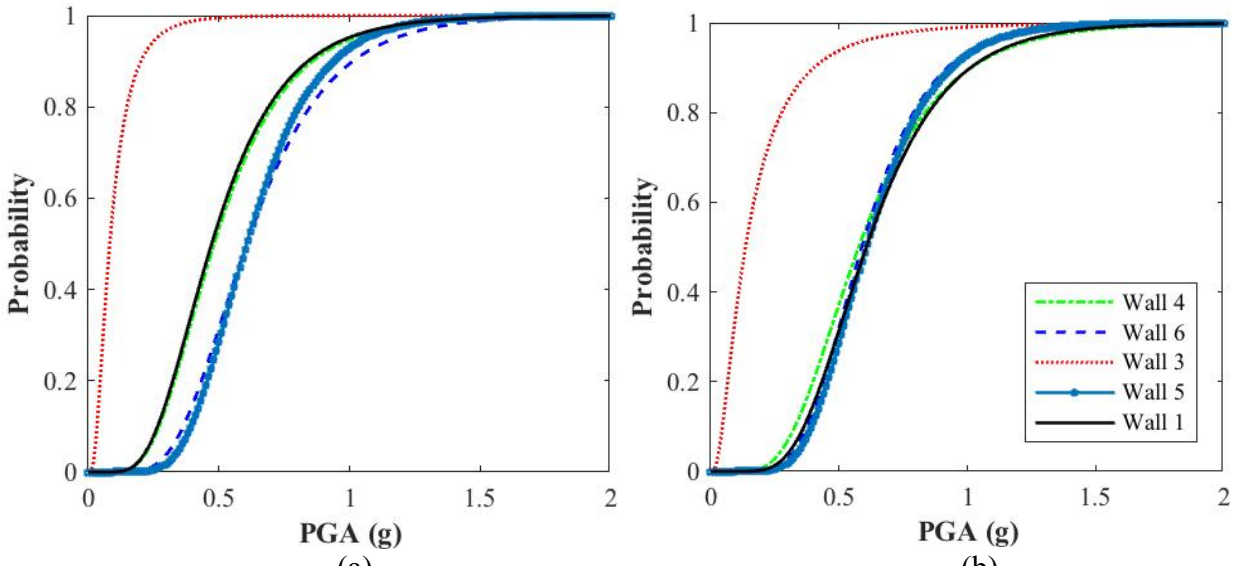

(a) (b)

Figure 3.21. Fragility curves for both larger than code compliant walls (#3 and #4) and retrofitted walls (#5 and #6) under Random Set 2:(a) Damage State 1, (b) Damage State 2.

3.5 CONCLUSION

One of the major findings from the current study was that the type of sample set used in the development of a fragility curve directly impacts the behavior of the resultant curve, in both median PGA and uncertainty. When only ground motions with larger PGA values, which typically were recorded at closer hypocentral distances, were used, the Texas motions appeared to be less fragile than those from the New Madrid suite. This observation can be attributed to the differences in both spectral shape and duration between ground motions representative of the two regions. However, when ground motions with smaller PGAs were scaled to be utilized for fragility curves, the resultant spectral shapes and fragility curves for those sample sets appeared closer to the results with New Madrid inputs. Ultimately, Texas ground motions would be expected to result in lower relative fragilities for damage compared to that of New Madrid, which is based on the results from when larger PGA records from the Texas suite were utilized and are the types of motions actually large enough to cause damage without scaling the input file. The sensitivity study showed that the most critical aspect of installing veneer ties is to include one at the top of the wall, even if ties are missing or not engaged within the center portion of the wall. In addition, when considering economical retrofit options, simply adding a connection at the top of the veneer wall was found to effectively increase the façade's resistance to ground motion.

Chapter 4: Conclusion, Recommendations, and Future Research

4.1 Summary of Research Project

A study was done to better understand the fragility of brick veneer in the Texas and Oklahoma region, due to human-induced seismic activity. Based on available census data, the decision was made to focus on wood-frame construction with clay brick veneer because of its prominence within the region of interest. After reviewing relevant previous research, it was determined that the Reneckis and LaFave (2009) study provided the most applicable experimental and FE model results upon which to base the computational model for the current study. The OpenSEES model in this study was initially created using material properties from the previous FE model, but alterations were made to calibrate the model to the experimental results. The model was validated by comparing the veneer and backup displacements to those measured in Wall-1 and Wall-2 tests from the previous Reneckis and LaFave (2009) study. The ground motion used in the validations was the same New Madrid time history utilized for testing in the previous study, which came from a suite of 20 synthetic time histories from Wen and Wu (2001).

An additional suite of Texas, Oklahoma, and Kansas ground motion files was created from those provided by researchers at the University of Texas at Austin. Fragility curves were developed for both the New Madrid and Texas suites, using samples of 20 input files to determine the probabilities utilized for each fragility curve. Sample sets were chosen based on varying ground motion characteristics to determine the impact on the relative fragility of the curves. The spectral acceleration responses of each sample set were plotted, in order to show the impact on the relative fragility of the curves as well, and compare to the natural periods calculated for the OpenSEES models. In addition, a random sample set was used to create

fragility curves for a parametric study that examined the importance of tie location and gauge on the veneer wall performance. The parametric study was intended to better understand the impact of possible installation errors and subsequent retrofit options.

4.2 CONCLUSIONS

Analyzing the results from the Texas suite and parametric study fragility curves, led to the following conclusions about the seismic vulnerability of masonry façades in the region of interest.

- The most fragile sampling, likely to result in the most damage, could be predicted using the highest magnitude events recorded in the region.
- The range of fragilities of the Texas curves demonstrates that PGA, or any one particular intensity measure, does not necessarily directly predict the level of damage, or fragility, because there is a large range of behavior based upon the parameter chosen. Therefore, reliance on measured PGAs from seismic events in the Texas and Oklahoma regions may not accurately predict the veneer damage from those events. Other intensity measures, such as peak ground velocity (PGA) or spectral acceleration at a specific period (e.g., S_a(0.2sec)), may provide more consistent estimates of damage and should be investigated in future studies.
- The shape of the spectral acceleration response can greatly vary within ground motion sample sets for the same region. This variation impacts the resultant fragility curves based on where the natural period of the model falls along the acceleration response spectrum.

- Even if there are ties that are missing, or not engaged, within the center of the wall, having ties located at the top portion of the wall allows the veneer to perform moderately well under seismic activity.
- The parametric study showed that having a tie at the top of the veneer wall was more important in reducing fragility than the gauge of the tie. The wall that had a top tie, even though it was thinner than code compliant, still performed significantly better than the wall with the same 48 inch spacing, but no top tie.

4.3 Recommendations and Future Research

Based on the conclusions made in Section 4.2, the following recommendations would allow for improved damage predictions and veneer wall performance under the region's seismic activity.

- When trying to predict the fragility of masonry façade, it is important to utilize ground motions from the region of interest to represent the specific seismic hazards experienced in that region, rather than from events representative of other seismic hazards elsewhere in the U.S. or the world.
- Even though the relative fragility was low compared to other Texas sample sets, to most accurately predict the damage to brick veneer in the region, with a single sample set, ground motions with the largest PGA or smallest hypocentral distance should be considered. Fragilities created using ground motions with Larger PGA or smaller hypocentral distances are more representative of ground motions that are likely to actually cause damage, rather than records of lower shaking intensity that have been scaled to a level that will cause damage to the veneer.

- Although using a code compliant gauge for veneer ties is ideal, the most critical part of installation is including ties in the upper portion of a wall panel.
- If it is desired to strengthen an existing brick veneer wall, without having to reconstruct the entire wall, the addition of ties, or alternative anchors, at the top of the wall will still provide increased seismic resistance. This retrofit approach may be a good course of action if it is suspected that there are ties that are missing, have corroded, or were not installed properly.

In order to continue to better understand the performance of brick façades, under seismic loads, the following areas for future research are recommended.

- It would be beneficial to study the comparison between the different Texas fragility curves and the actual observed levels of damage from events. Photos and personal accounts of brick veneer damage would need to be compiled in order to do so. The comparison would determine which sample set is the most accurate prediction of actual veneer damage
- Fragility curves using the same sample sets should be recreated for different intensity measures, such as spectral acceleration and PGV. PGA was utilized in the current study to allow comparison to previous results, but it would be beneficial to analyze the impact of using alternative intensity measures.
- The parametric study could be expanded to explore more combinations of tie layout, gauge, and fastener type. Testing additional variables would provide more knowledge of the sensitivity of the wall performance to each one individually. Expanding the retrofit study could also include defining the behavior of helical

anchors in OpenSEES and then developing fragility curves with those present at the top of the veneer wall, rather than just additional ties.

- It would be beneficial to subject real wall panels, similar to the ones tested in the previous study, to ground motions from the Texas suite, and then compare the damage results to the fragility curves created in this study.

Appendix A

Table A.1: Random 1 Sample Set Ground Motion Recordings

Date	PGA (g)	Magnitude	Depth (km)	V_{s30} (m/s)	Hypocentral Distance (km)
4/16/13	0.005	4.4	5	578	56.6
9/3/16	0.005	5.8	5.4	666	271.7
6/18/14	0.005	4.1	5	796	21.3
2/13/16	0.007	5.1	8	503	182.6
9/3/16	0.007	5.8	5.4	764	272
11/7/16	0.007	5	5	1534	160.6
11/7/16	0.0073	5	5	1118	166
2/13/16	0.0074	5.1	8	183	104.3
11/7/16	0.01	5	5	353	129.7
9/3/16	0.011	5.8	5.4	818	219.2
4/16/13	0.0114	4.2	5	796	45.6
9/3/16	0.03	5.8	5.4	765	112.8
9/25/15	0.0344	4	2.9	448	7.2
9/3/16	0.035	5.8	5.4	493	94.6
9/3/16	0.042	5.8	5.4	525	97.4
9/3/16	0.042	5.8	5.4	1534	173.3
9/3/16	0.044	5.8	5.4	503	35.4
9/3/16	0.045	5.8	5.4	664	136.1
9/3/16	0.045	5.8	5.4	612	180.2
11/12/14	0.094	4.9	4	396	15.6

Table A.2: Random 2 Sample Set Ground Motion Recordings

Date	PGA (g)	Magnitude	Depth (km)	V_{s30} (m/s)	Hypocentral Distance (km)
11/19/15	0.0066	4.7	5.9	503	166
11/5/11	0.007	5	6.2	1321	127.3
9/21/13	0.007	5.4	10	1002	260.3
11/7/16	0.007	5	5	1118	166
1/7/16	0.008	4.7	4.1	493	66.5
10/20/11	0.01	4.8	14.2	430	36.1
11/7/16	0.013	5	5	906	31.6
11/6/11	0.0132	5.7	7.5	521	46.1
11/7/16	0.016	5	5	796	81.8
2/13/16	0.018	5.1	8	500	56.8
5/17/12	0.032	4.4	5	401	33.5
9/3/16	0.038	5.8	5.4	672	52.6
9/3/16	0.041	5.8	5.4	353	81.3
10/2/14	0.0433	4.5	5	946	19
9/3/16	0.044	5.8	5.4	502	101.3
12/29/15	0.0457	4.3	6.5	502	12.9
9/3/16	0.047	5.8	5.4	254	162.1
11/12/14	0.098	4.9	4	825	18.4
11/19/15	0.118	4.7	5.9	500	28
10/10/15	0.1329	4.3	3.3	448	7.5

Table A.3: Random 3 Sample Set Ground Motion Recordings

Date	PGA (g)	Magnitude	Depth (km)	V_{s30} (m/s)	Hypocentral Distance (km)
9/3/16	0.005	5.8	5.4	666	271.7
11/5/11	0.007	5	6.2	1321	127.3
9/21/13	0.007	5.4	10	1002	260.3
2/13/16	0.007	5.1	8	503	182.6
9/3/16	0.007	5.8	5.4	764	272
2/3/16	0.0084	5.1	8	183	104.3
10/20/11	0.01	4.8	14.2	430	36.1
11/7/16	0.013	5	5	906	31.6
11/6/11	0.0132	5.7	7.5	521	46.1
11/7/16	0.016	5	5	796	81.8
9/3/16	0.03	5.8	5.4	765	112.8
5/17/12	0.032	4.4	5	401	33.5
9/25/15	0.0344	4	2.9	448	7.2
9/3/16	0.035	5.8	5.4	493	94.6
9/3/16	0.042	5.8	5.4	525	97.4
10/2/14	0.0433	4.5	5	946	19
9/3/16	0.045	5.8	5.4	664	136.1
9/3/16	0.045	5.8	5.4	612	180.2
9/3/16	0.047	5.8	5.4	254	162.1
10/10/15	0.1329	4.3	3.3	448	7.5

Table A.4: Random 4 Sample Set Ground Motion Recordings

Date	PGA (g)	Magnitude	Depth (km)	V_{s30} (m/s)	Hypocentral Distance (km)
4/16/13	0.005	4.4	5	578	56.6
9/3/16	0.005	5.8	5.4	666	271.7
11/19/15	0.0066	4.7	5.9	503	166
2/13/16	0.007	5.1	8	503	182.6
11/7/16	0.007	5	5	1118	166
2/13/16	0.0074	5.1	8	183	104.3
6/18/14	0.0075	4.1	5	796	21.3
4/16/13	0.0075	4.2	5	796	45.6
10/20/11	0.01	4.8	14.2	430	36.1
11/6/11	0.0132	5.7	7.5	521	46.1
9/3/16	0.03	5.8	5.4	765	112.8
9/25/15	0.0344	4	2.9	448	7.2
9/3/16	0.038	5.8	5.4	672	52.6
9/3/16	0.041	5.8	5.4	353	81.3
10/2/14	0.0433	4.5	5	946	19
9/3/16	0.044	5.8	5.4	502	101.3
9/3/16	0.045	5.8	5.4	664	136.1
12/29/15	0.0457	4.3	6.5	502	12.9
11/12/14	0.094	4.9	4	396	15.6
10/10/15	0.1329	4.3	3.3	448	7.5

Table A.5: Maximum Magnitude Sample Set Ground Motion Recordings

Date	PGA (g)	Magnitude	Depth (km)	V_{s30} (m/s)	Hypocentral Distance (km)
9/3/16	0.033	5.8	5.4	825	109.2
	0.036	5.8	5.4	1008	122.9
	0.0472	5.8	5.4	701	109.2
	0.0326	5.8	5.4	971	134.3
	0.0555	5.8	5.4	591	89.4
	0.0568	5.8	5.4	448	57.6
	0.0598	5.8	5.4	500	121.6
	0.0309	5.8	5.4	330	156
	0.0051	5.8	5.4	666	271.7
	0.0595	5.8	5.4	672	52.6
	0.0366	5.8	5.4	860	55.1
	0.0596	5.8	5.4	524	84.2
	0.0325	5.8	5.4	493	94.6
	0.0052	5.8	5.4	764	272
	0.0352	5.8	5.4	612	180.2
	0.0419	5.8	5.4	1534	173.3
	0.0145	5.8	5.4	700	185.4
	0.0132	5.8	5.4	818	219.4
	0.003	5.8	5.4	439	362.4
	0.0053	5.8	5.4	697	298.4

Table A.6: Maximum PGA Sample Set Ground Motion Recordings

Date	PGA (g)	Magnitude	Depth (km)	V_{s30} (m/s)	Hypocentral Distance (km)
11/7/16	0.5947	5	5	672	5.2
11/7/16	0.3278	5	5	860	6.4
11/7/16	0.2731	5	5	718	9.6
11/7/16	0.2085	5	5	509	7.1
6/5/15	0.17	4.2	2.4	995	7
8/19/14	0.1413	4.1	4.5	630	5.4
10/10/15	0.1329	4.3	33	448	7.5
11/23/15	0.1157	4.4	5	500	8.6
11/12/14	0.0974	4.9	4	825	18.4
11/12/14	0.094	4.9	4	396	15.6
11/19/15	0.0927	4.7	5.9	500	28
10/2/14	0.0743	4.5	5	1008	9.9
10/2/14	0.073	4.5	5	524	8.6
9/25/15	0.0695	4	2.9	509	6.7
11/7/15	0.0676	4.1	5	701	10.8
1/1/16	0.0604	4.2	5.8	502	12.9
9/3/16	0.0598	5.8	5.4	500	121.6
9/3/16	0.0596	5.8	5.4	524	84.2
9/3/16	0.0595	5.8	5.4	672	52.6
6/20/15	0.059	4	3	630	9.4

Table A.7: Minimum Hypocentral Distance Sample Set Ground Motion Recordings

Date	PGA (g)	Magnitude	Depth (km)	V_{s30} (m/s)	Hypocentral Distance (km)
8/19/14	0.1413	4.1	4.5	630	5.4
10/2/14	0.0743	4.5	5	1008	9.9
10/2/14	0.073	4.5	5	524	8.6
6/5/15	0.0381	4.2	2.4	1008	6.3
6/5/15	0.17	4.2	2.4	995	7
6/5/15	0.0445	4.2	2.4	524	8.1
6/5/15	0.0465	4.2	2.4	971	13.6
6/20/15	0.059	4	3	630	9.4
9/25/15	0.0344	4	2.9	448	7.2
9/25/15	0.0695	4	2.9	509	6.7
10/10/15	0.1329	4.3	3.3	448	7.5
11/7/15	0.0676	4.1	5	701	10.8
11/20/15	0.0316	4.1	5	701	13.1
11/20/15	0.0411	4.1	5	183	13
11/23/15	0.1157	4.4	5	500	8.6
12/29/15	0.0457	4.3	6.5	502	12.9
1/1/16	0.0604	4.2	5.8	502	12.9

Appendix B

28ga(min) Tie Backbone	
Displacement (in)	Force (lb)
0.05	100
0.154	160
0.6	10

28ga(ecc) Tie Backbone	
Displacement (in)	Force (lb)
0.32	44
0.48	146
0.6	80

22ga(min) Tie Backbone	
Displacement (in)	Force (lb)
0.01	90
0.05	155
0.6	110

22ga(ecc) Tie Backbone	
Displacement (in)	Force (lb)
0.08	60
0.27	155
0.6	120

References

Abaqus, Inc. (2006). *ABAQUS 6.6-2,* Providence, R.I.

American Society of Civil Engineers (ASCE). (2005). "Minimum Design Loads for Buildings and Structures." *ASCE 7-05,* New York, N.Y.

ASCE. (2006). "Seismic Rehabilitation of Existing Buildings." *ASCE 41-06*, New York, N.Y.

ASTM. (2002a). "Standard Test Method for Compressive Strength of Masonry Prisms." *ASTM C 1314-02*, West Conshohocken, Pa.

ASTM. (2002b). "Standard Test Method for Young's Modulus, Tangent Modulus, and Chord Modulus." *ASTM E 111-97*, West Conshohocken, Pa.

ASTM. (2002c). "Standard Test Method for Preconstruction and Construction Evaluation of Mortars for Plain and Reinforced Unit Masonry." *ASTM C 780-00*, West Conshohocken, Pa.

ASTM. (2002d). "Standard Test Methods for Flexural Bond Strength of Masonry." *ASTM E 518-00a*, West Conshohocken, Pa.

Bradtmueller, J., and Foley, S. (2014). "Historical Trends of Exterior Wall Materials used in US Residential Construction." *50th ASC Annual International Conference.*

Curtis, P. (2015). The Dos and Don'ts of Masonry Anchors: Anchors, Connectors, and Fasteners. *Masonry Magazine.*

Doherty, K., Griffith, C., Lam, N., and Wilson, J. (2002). "Displacement-Based Seismic Analysis for Out-of-Plane Bending of Unreinforced Masonry Walls." *Earthquake Engineering and Structural Dynamics,* 31, 833-850.

Earthquake Engineering Research (EERI). (2016). Oklahoma, USA Earthquake Clearinghouse. *EERI. <http://www.eqclearinghouse.org/2016-09-03-oklahoma/>*

Ellsworth, M.L. (2012). Injection-Induced Earthquakes. *Science Magazine, 341(6142).*

Filiatrault, A., Fischer, D., Folz, B., and Uang, C.M. (2002). "Seismic Testing of Two- Story Woodframe House: Influence of Wall Finish Materials." *Journal of Structural Engineering,* 128(10), 1337-1345.

Heckmann Building Products, Inc. (2018). *Heckmann Building Products – Products Catalog.* < http://www.heckmannbuildingprods.com/cat200.html>

International Masonry Institute (IMI), The Brick Institute of America (BIA), The Masonry Society (TMS), and The Masonry Institute of America (MIA). (1990). *The Loma Prieta, California, Earthquake of October 17, 1989; Observations Regarding the Performance of Masonry Buildings,* Washington, D.C.

Isoda, H., Folz, B., and Filiatrault, A. (2001). Seismic Modeling of Index Woodframe Buildings, *Report No. SSRP-2001/12*, Division of Structural Engineering, University of California, San Diego.

Jones, C. and Killman, C. Earthquake insurance: 3 in 20 claims approved in Oklahoma since 2010. *Tulsa World News.* (2017). <http://www.tulsaworld.com/earthquakes/earthquake-insurance-in-claims-approved-in-oklahoma-since/article_de588725-1475-592c-9025-bdcfbf9b8bcd.html>.

Masonry Standards Joint Committee (MSJC). (2008). *Building Code Requirements for Masonry Structures. ACI 530-08/ASCE 5-08/TMS 402-08,* ACI, Farmington Hills, Mich.; ASCE, Reston, Va.; TMS, Boulder, Colo.

McGarr, A. (2014). "Maximum magnitude earthquakes induced by fluid injection." *Journal of Geophysical Research*, 119(3), 1008-1019.

McKenna, F., Fenves, G.L., and Scott, M.H. (2004). "Open System for Earthquake Engineering Simulation." *Pacific Earthquake Engineering Research Center*, University of California Berkeley.

National Design Specification for Wood Construction (NDS). (2001). American Forest and Paper Association, Washington, D.C.

Kharrazi, M.H.K. and Ventura, C.E. (2006). "Vibration Frequencies of Woodframe Residential Construction." *Earthquake Spectra,* 22(4), 1015-1034.

Khosravikia F, Potter A, Prakhov V, Zalachoris G, Cheng T, Tiwari A, et al. Seismic Vulnerability and Post-Event Actions for Texas Bridge Infrastructure. FHWA/TX-17/0-6916-1, Center for Transportation Research (CTR): 2018.

Klingner, R.E., Mcginley, W.M., Shing, P., McLean, D.I., Seonwoo, J., and Okail, H. (2013). "Seismic Performance of Low-Rise Wood-Framed and Reinforced Masonry Buildings with Clay Masonry Veneer." *Journal of Structural Engineering, 139(8), 1326-1339.*

Petersen, M.D., Moschetti, M. P., Luco, N., Frankel, A. D., Aagaard, B. T., Baltay, A. S., Blanpied, M. L., Boyd, O. S., Brigg, R. W., Gold, R. D., Graves, R. W., Hartzell, S. H., Rezaeian, S., Stephenson, W. J., Wald, D. J., Williams, R. A., and Withers, K. B. (2018). "2018 One-Year Seismic Hazard Forecast for the Central and Eastern United States from Induced and Natural Earthquakes." *Seismological Research Letters,* 89(3), 1049-1061.

Reneckis, D. and LaFave J.M. (2009). Seismic Performance of Anchored Brick Veneer. *NSEL, University of Illinois at Urbana-Champaign, Report No. NSEL-016.*

Simsir, C.C. (2004). *Influence of Diaphragm Flexibility on the Out-of-Plane Dynamic Response of Unreinforced Masonry Walls,* Ph.D. Thesis, University of Illinois at Urbana-Champaign, Urbana, Ill.

U.S. Census Bureau. (2013). 2013 Characteristics of New Housing Survey. *U.S. Department of Commerce.* https://www.census.gov/construction/chars/pdf/c25ann2013.pdf

U.S. Census Bureau. (2016a). Census Regions and Divisions of the United States. *U.S. Department of Commerce, Economics, and Statistics Administration: U.S. Census Bureau.* https://www2.census.gov/geo/pdfs/maps-data/maps/reference/us_regdiv.pdf>

U.S. Census Bureau. (2016b). Primary Type of Exterior Wall Material of New Single-Family Houses Completed. *U.S. Department of Commerce, Economics, and Statistics Administration: U.S. Census Bureau.* https://www.census.gov/construction/chars/completed.html

USGS. (2016a). 2016 Short-Term Model. *USGS Earthquake Hazards Program.* https://earthquake.usgs.gov/hazards/hazmaps/conterminous/index.php#2016

USGS. (2016b). M5.0-3km West of Cushing, Oklahoma – Shake Map. *Earthquake Hazards Program. https://earthquake.usgs.gov/earthquakes/eventpage/us100075y8#executive*

USGS. (2016c). M5.1-31km NW of Fairview, Oklahoma – Shake Map. *Earthquake Hazards Program. https://earthquake.usgs.gov/earthquakes/eventpage/us20004zy8#shakemap*

USGS. (2016d). M5.8-14km NW of Pawnee, Oklahoma – Shake Map. *Earthquake Hazards Program.* https://earthquake.usgs.gov/earthquakes/eventpage/us10006jxs#shakemap

Wen, Y.K. and Wu, C.L. (2001). "Uniform Hazard Ground Motions for Mid-America Cities." *Earthquake Spectra,* 17(2), 359-384.

Zalachoris, G., and Rathje, E. M. (2017a). "Ground Motion Models for Earthquake Events in Texas , Oklahoma , and Kansas." 3rd International Conference on Performance Based Design in Earthquake Geotechnical Engineering, Vancouver, BC, Canada.

Zalachoris, G., Rathje, E. M., and Paine, J. G. (2017b). "V S30 Characterization of Texas , Oklahoma , and Kansas Using the P-Wave Seismogram Method." *Earthquake Spectra*, 33(3), 943–961.